Coal fly ash: How sample properties and methodology influence immersion freezing results

Von der Fakultät für Physik und Geowissenschaften
der Universität Leipzig genehmigte

DISSERTATION

zur Erlangung des Akademischen Grades

Doktor der Meteorologie
Dr. rer. nat.

vorgelegt von

M. Sc. Sarah Grawe

geboren am 20.08.1990 in Leipzig

UNIVERSITÄT
LEIPZIG

TROPOS
Leibniz-Institut für
Troposphärenforschung

Gutachter: Prof. Dr. Andreas Macke
Prof. Dr. Benjamin J. Murray

Tag der Verleihung: 08.07.2019

Diese Arbeit wurde angefertigt zwischen Oktober 2015 and Februar 2019
am Leibniz-Institut für Troposphärenforschung (TROPOS),
Abteilung Experimentelle Aerosol- und Wolkenmikrophysik,
Permoserstr. 15,
04318 Leipzig.

Diese Arbeit wurde betreut von
Prof. Dr. Andreas Macke.

Bibliographische Beschreibung

Kohle-Flugasche: Einfluss von Probeneigenschaften und Methodologie auf Messergebnisse zum Immersionsgefrierverhalten
Grawe, Sarah
Universität Leipzig, Dissertation
146 Seiten, 196 Zitate, 39 Abbildungen, 6 Tabellen, 3 Anlagen.

Zusammenfassung Aufgrund ihrer speziellen Eigenschaften können sogenannte eisnukleierende Partikel die Bildung von Eis in Wolken katalysieren. Laboruntersuchungen zum Gefrierverhalten dieser Partikel haben sich als wertvoll erwiesen, wenn es um das Verständnis zugrunde liegender Prinzipien und Mechanismen geht. Eine Spezies, die in früheren Untersuchungen vernachlässigt wurde, ist Flugasche aus Kohleverbrennung. Kohle-Flugasche (KFA) wird aufgrund ineffizienter Filterung submikroner Partikel über die Schornsteine von Kraftwerken emittiert und kann, in Abhängigkeit der meteorologischen Bedingungen, die Vereisung von Wolken in der Nähe der Quelle und darüber hinaus beeinflussen. In dieser Arbeit wurde das Immersionsgefrierverhalten, d.h. der Einfluss eingeschlossener Partikel auf das Gefrieren unterkühlter Tropfen, für vier verschiedene KFA-Proben aus deutschen Kohlekraftwerken untersucht. Dabei wurden einerseits Tropfen untersucht, die ein einzelnes submikrones Partikel enthielten. Andererseits wurde das Gefrierverhalten von Suspensionstropfen, die eine Vielzahl verschieden großer Partikel beinhalteten, quantifiziert. Zusätzlich wurden die Proben, sowohl in ihrer Gesamtheit als auch in Form einzelner submikroner Partikel, bezüglich ihrer chemischen Zusammensetzung, Morphologie und Kristallographie analysiert. Es wurde festgestellt, dass die Gefriereffizienz der Proben innerhalb von Minuten abnimmt, sobald diese in Berührung mit Wasser kommen. Immersionsgefriermessungen mit purem Anhydrit ($CaSO_4$), das in den Proben nachgewiesen wurde, zeigten einen ähnlichen Trend, d.h. eine abnehmende Effizienz mit zunehmender Suspensionszeit. Diese Beobachtung, und die Übereinstimmung von Messungen mit KFA-Suspensionspartikeln und Gips ($CaSO_4 \cdot 2H_2O$, ein Hydrat des Anhydrits), weisen darauf hin, dass Hydratation die Ursache für die Abnahme der Gefriereffizienz sein könnte. Dieser Einfluss von Probeneigenschaften und Methodologie auf das Immersionsgefrierverhalten von KFA-Partikeln muss bei der Abschätzung der Relevanz der Partikel für die atmosphärische Eisnukleation unbedingt berücksichtigt werden.

Bibliographic description

Coal fly ash: How sample properties and methodology influence immersion freezing results
Grawe, Sarah
Leipzig University, dissertation
146 pages, 196 references, 39 figures, 6 tables, 3 appendices.

Abstract Due to their specific properties, atmospheric ice-nucleating particles are able to catalyze ice formation in clouds. Laboratory studies investigating the freezing behavior of these particles have proven to be of unmatched value when attempting to understand underlying principles and mechanisms. One species that has almost entirely been neglected in previous ice nucleation studies is fly ash from coal combustion (CFA: coal fly ash). Emitted through the stacks of power plants due to inefficient filtering of submicron particles, CFA has the potential to influence cloud glaciation in source regions and beyond, depending on the meteorological conditions. In this thesis, the immersion freezing behavior, i.e., the influence of particles immersed in supercooled cloud droplets on ice nucleation, of four samples from German power plants was determined with the help of several single particle and bulk instruments. In parallel, single particles and bulk CFA were investigated with respect to their chemical composition, morphology, and crystallography. It was found that the immersion freezing efficiency of the CFA particles decreases in contact with water on the time scale of minutes. Hydration products, that were found in both single particles and in the bulk after suspension, could be responsible for this unique behavior. Immersion freezing measurements with pure anhydrite (anhydrous $CaSO_4$), which is known to occur at the surface of CFA particles, showed the same qualitative trend, i.e., a decreasing efficiency with increasing suspension time. This observation, and the agreement between measurements with suspended CFA particles and gypsum ($CaSO_4 \cdot 2H_2O$, a hydrate of anhydrite), support the hypothesis that hydration causes the observed decrease in immersion freezing efficiency. This influence of sample properties and methodology on the immersion freezing behavior of CFA must be taken into consideration when assessing the relevance of these particles for atmospheric ice nucleation.

Contents

1 Introduction **1**

2 Fundamentals **7**
2.1 Ice nucleation theory 7
2.1.1 Homogeneous ice nucleation 9
2.1.2 Heterogeneous ice nucleation 12
2.2 Properties of CFA particles 17
2.2.1 Physicochemical particle properties 17
2.2.2 Ice nucleation properties 19

3 Materials and Methods **25**
3.1 Materials 25
3.2 Methods 26
3.2.1 Sample preparation and particle generation 29
3.2.2 Immersion freezing instrumentation 31
3.2.3 Physicochemical sample characterization 39

4 Results **43**
4.1 Physicochemical sample characterization 43
4.1.1 Single particle methods 43
4.1.2 Bulk methods 53
4.1.3 Size distribution measurements 63
4.2 Immersion freezing behavior of CFA 65
4.2.1 Dry particle generation 65
4.2.2 Suspension methods 68

5 Discussion **73**
5.1 Comparison to literature results 73
5.1.1 Havlíček et al. (1993) 73
5.1.2 Garimella (2016) 75
5.1.3 Umo et al. (2015) 76
5.1.4 Losey et al. (2018) 78

5.2 Physicochemical particle properties and immersion freezing behavior . . . 80
5.2.1 ALABAMA signal intensity and CFA immersion freezing efficiency . . . 80
5.2.2 Comparision between CFA and identified substances . 82
5.2.3 Effect of sample treatment . . . 88
5.3 Atmospheric implications . . . 92

6 Summary and Conclusions **95**

7 Outlook **99**

Appendices **101**

A Instrumentation **103**
A.1 Electrostatic precipitator . . . 103
A.2 ALABAMA . . . 104
A.3 Multi-MINI . . . 106

B Methods **107**
B.1 Multiple charge correction . . . 107
B.2 LINA calibration routine . . . 108

C LACIS Measurements with Wet-generated CFA1 **111**

List of Abbreviations **115**

List of Symbols **117**

List of Figures **123**

List of Tables **125**

References **127**

1 Introduction

Clouds are important factors influencing Earth's weather and climate, but also still major contributors of uncertainty to radiative forcing estimates (IPCC, 5th Assessment Report; Boucher et al., 2013). This is due to cloud related processes which are not yet sufficiently understood and hence not, or inadequately, represented in climate models. These processes include the formation of ice particles, which are known to influence cloud radiative properties and lifetime (Lohmann and Diehl, 2006; Storelvmo et al., 2011; Chakraborty et al., 2016; Vergara-Temprado et al., 2018), chemical reactions (Zondlo et al., 2000; Abbatt, 2003; Weiss et al., 2016), electrification (Takahashi, 1978; Saunders, 1993; Sherwood et al., 2006), and precipitation formation in mid-latitudes (Houghton, 1950; Rogers and Yau, 1989). There are two pathways for ice formation in the atmosphere. Primary ice formation, which is always initiated by a nucleation process, and secondary ice formation, which can cause multiplication once ice particles have formed due to nucleation (Field et al., 2017, and references therein). Ice nucleation occurs both homogeneously and heterogeneously. Homogeneous ice nucleation describes nucleation of a pure water or solution droplet below ~ -38 °C. Heterogeneous ice nucleation may take place at temperatures just below 0 °C and is always initiated by aerosol particles featuring specific properties, so-called ice-nucleating particles (INPs). Different modes of heterogeneous ice nucleation exist (see Sec. 2.1.2), but this thesis focuses on immersion freezing, i.e., heterogeneous nucleation triggered by an INP immersed in a supercooled cloud droplet. This mechanism has been shown to be of importance for ice formation in mixed-phase clouds which exist in a temperature range between 0 and ~ -38 °C (Ansmann et al., 2008; de Boer et al., 2011; Westbrook and Illingworth, 2011).

General objectives of experimental ice nucleation researchers are the improvement of process understanding and the development of suitable parameterizations for implementation in climate models. As there are no unambiguous criteria for defining whether a certain type of aerosol particle is a good INP (Pruppacher and Klett, 1997; Murray et al., 2012), ice nucleation research has been focusing on quantitative experimentation since its early stages (Vonnegut, 1947; aufm Kampe and Weickmann, 1951). Simultaneous to the ice

nucleation experiments, additional physical and chemical particle characterization analyses have frequently been performed in order to find a connection between physicochemical and ice nucleation properties. Conclusive studies explaining how the ice nucleation efficiency of different mineral dust types depends on lattice spacing, chemical bonds, and defects at the INP surface have been published by, e.g., Shen et al. (1977), Sihvonen et al. (2014), and Kiselev et al. (2017). Although there is a growing tendency of capturing atmospheric INP concentrations in field experiments (Boose et al., 2016b; DeMott et al., 2016; Schmidt et al., 2017; DeMott et al., 2017; Welti et al., 2018; Lacher et al., 2018), heterogeneous ice nucleation has continuously been studied in laboratories in recent years (Whale, 2018). In the course of this, recently further insight has been gained into the ice nucleation potential of almost every type of atmospherically relevant aerosol, including mineral dust from both deserts (Kaufmann et al., 2016; Boose et al., 2016a) and agricultural areas (Hill et al., 2016; Steinke et al., 2016), volcanic emission particles (Kulkarni et al., 2015; Mangan et al., 2017; Genareau et al., 2018), biological particles, i.e, bacteria (Polen et al., 2016; Ling et al., 2018), pollen (Dreischmeier et al., 2017; Gute and Abbatt, 2018), fungal spores (Fröhlich-Nowoisky et al., 2015; Pummer et al., 2015), and plant material (Hiranuma et al., 2015b; Felgitsch et al., 2018), particles originating from open water bodies (Wilson et al., 2015; Moffett, 2016; DeMott et al., 2016; Knackstedt et al., 2018), secondary organic aerosol particles (Ignatius et al., 2016; Wagner et al., 2017; Frey et al., 2018), and combustion particles, i.e., soot (Kulkarni et al., 2016; Levin et al., 2016; Schill et al., 2016; Mahrt et al., 2018b) and ash (Umo et al., 2015; Garimella, 2016; Grawe et al., 2016). The heterogeneous ice nucleation potential of the latter is the least studied of the mentioned species and underlying processes are enigmatic. Hence, physicochemical and ice nucleation properties of ash particles are the focal points of this thesis.

During the combustion of organic substances, there is the emission of primary aerosol particles, i.e., carbonaceous particles and ash, and gaseous precursors, which may form secondary aerosol particles. Carbonaceous particles, i.e., soot or tar balls (Pósfai et al., 2004; Sedlacek III et al., 2018), are composed of C and H and form via incomplete combustion or pyrolysis of the fuel. In contrast, ash particles only contain a limited amount of C as they are primarily composed of the mineral inclusions in the fuel, i.e., of heteroatoms like K, Ca, Na, Mg, P, S, and Fe (Flagan and Seinfeld, 1988a). Ash can originate from both solid or liquid fuel combustion. However, it has been shown that the

ash content, which is the amount of material left after complete combustion, of liquid fuel, e.g., fuel oil, is roughly two orders of magnitude below that of solid fuel, e.g., coal. This is due to mineral inclusions being practically absent in liquid fuels (Block and Dams, 1976; Flagan and Seinfeld, 1988a). A distinction is made between the fine ash fraction, i.e., fly ash, that is emitted during combustion together with flue gases, and the coarse ash fraction, i.e., bottom ash. The latter is defined as the fraction that remains in the power plant, fireplace, or on the ground after a wildfire and can also be emitted due to wind erosion. In total, 6709 coal-fired power plants (30 MW and larger; endcoal.org; status: July 2018) are in operation worldwide, producing more than 600 Mt a^{-1} of coal fly ash (CFA) and bottom ash (Ahmaruzzaman, 2010). The vast majority of this mass is not emitted into the atmosphere, because most coal-fired power plants are equipped with different types of particle removal technology to clean the flue gases of CFA. However, filtering systems show varying efficiencies and part of the collected CFA is emitted during transportation and disposal in landfills (Mueller et al., 2013). A rough assessment was given by Smil (2008), estimating that $\sim$30 Mt a^{-1} of CFA are released into the atmosphere globally. Reff et al. (2009) state that coal combustion causes $PM_{2.5}$ emissions of $\sim$0.5 Mt a^{-1} in the USA.

The ice nucleation potential of CFA has first been investigated more than 50 years ago, the starting point being observations of ice fog and snowfall in proximity to coal-fired power plants (Benson, 1965; Agee, 1971). Additionally, the relevance of CFA particles for atmospheric ice nucleation is shown by studies which identified them in ice crystal residues (Parungo et al., 1978b; DeMott et al., 2003; Eriksen Hammer et al., 2018). Despite of these findings, the number of studies investigating the ice nucleation potential of CFA particles is limited, especially when compared to other aerosol species such as mineral dust. Apart from an early investigation (Schnell et al., 1976), which proved to have used an unsuitable method, all other studies indicate that CFA particles are able to trigger heterogeneous ice nucleation (Parungo et al., 1978a; Havlíček et al., 1993; Umo et al., 2015; Garimella, 2016; Grawe et al., 2016). However, the reported efficiencies in the immersion mode vary by several orders of magnitude. On the one hand, differences between studies could of course be due to differences in physicochemical particle properties, as samples from different origins have been investigated in all cases. Most studies provide additional sample characterization with respect to chemical composition and crystallography, but from this it is still unclear which factors determine the immersion freezing behavior of the

investigated CFA particles. On the other hand, methodology could contribute to the observed variability, as my co-authors and I demonstrated in an earlier study (Grawe et al., 2016). There, the investigated CFA sample showed varying immersion freezing efficiencies depending on the particle generation technique, i.e., whether particles were generated from dry CFA powder (dry particle generation) or from a CFA–water suspension and subsequent drying (wet particle generation). See Sec. 2.2.2 for a full literature review.

To summarize, there is a need for further immersion freezing measurements with CFA particles because previous studies are sparse and show a large variability which cannot be explained by accompanying particle characterization analyses. There is indication that the used immersion freezing instrumentation influences the results, but so far there are no data of a single CFA sample investigated with more than two different methods. Hence, it is unclear in what way and how strongly CFA particles influence atmospheric immersion freezing. The present thesis aims at answering the following research questions:

- How does methodology influence CFA immersion freezing results?
- How do CFA samples from German power plants compare to samples from previous publications?
- Which physicochemical particle properties influence the immersion freezing behavior of CFA?
- How relevant is CFA for atmospheric immersion freezing?

Four CFA samples from German power plants were investigated using four different immersion freezing instruments in an attempt to answer these questions. The immersion freezing instruments can be classified into single particle instruments and cold stage instruments. The droplets investigated in the single particle instruments are airborne and contain a single particle each, whereas suspension droplets which each contain numerous particles are investigated on the cold stages. Due to the difference in surface area per droplet, the instruments can operate in different temperature ranges, ideally yielding information about the immersion freezing behavior from 0 to -38 °C. With the single particle instruments, size selected aerosol, and hence potential effects of size-dependent particle properties on immersion freezing, could be explored. Furthermore, the effect of suspension time on the immersion freezing behavior could be investigated by the application of the different methods. Dry-generated particles were suspended for a maximum

of 10 s in the single particle instruments before they initiated freezing. In contrast, wet-generated particles and particles in the suspension droplets on the cold stages, hereafter referred to as suspension methods, were in contact with water between ∼2 min and ∼24 h before experiments were performed. Data from the literature were considered in connection with data from this thesis to obtain a holistic view of all available immersion freezing measurements with CFA particles. Sample characterization with respect to chemical composition, morphology, and crystallography, was performed and used for interpretation of the immersion freezing results. Like this, components potentially influencing the immersion freezing behavior of the CFA samples could be identified. Finally, the contribution of CFA particles to ambient INP concentrations was roughly estimated based on the here presented findings.

Subsequent to this introduction, chapter 2 focuses on fundamentals, i.e., ice nucleation theory and properties of CFA particles which includes both physicochemical particle properties and ice nucleation properties as found in earlier studies. Chapter 3 includes information about the origin of the investigated samples and the applied methods and instrumentation. The results of the primary investigations of the CFA samples will be shown in chapter 4. Chapter 5, i.e., the discussion, begins with a comparison of my immersion freezing results to data from the literature. Furthermore, the connection between immersion freezing properties and physicochemical particle properties will be discussed. Hypotheses resulting from this will be tested by evaluating additional measurements with pure substances contained in the CFA samples and with modified CFA samples. Chapter 5 closes with a discussion about possible atmospheric implications of my findings. Chapter 6 contains a summary of the results and chapter 7 an outlook on future research perspectives.

Please note that hereafter, text passages and figures are taken from the following peer-reviewed publication which was published in the framework of my PhD thesis:

Grawe, S., S. Augustin-Bauditz, H.-C. Clemen, M. Ebert, S. Eriksen Hammer, J. Lubitz, N. Reicher, Y. Rudich, J. Schneider, R. Staacke, F. Stratmann, A. Welti, and H. Wex (2018). “Coal fly ash: linking immersion freezing behavior and physicochemical particle properties”. In: *Atmospheric Chemistry and Physics* 18, pp. 13903–13923.

2 Fundamentals

The following chapter focuses on two fundamental aspects of immersion freezing induced by CFA particles. Firstly, I introduce the theory of homogeneous and heterogeneous ice nucleation. Secondly, I summarize results from the literature concerning physicochemical properties of CFA and give an overview of previous ice nucleation measurements with CFA particles.

2.1 Ice nucleation theory

Nucleation is defined as the formation of a new stable phase at the expense of an original metastable phase in a thermodynamic system (Pruppacher and Klett, 1997). Nucleation does not necessarily occur as soon as the energy of the stable phase is lower than that of the metastable phase. Rather, spatial and temporal fluctuations of density and temperature cause the spontaneous formation of a molecular nuclei of the stable phase within the metastable phase. Ice nucleation, i.e., the formation of ice particles from the vapor or liquid phase, takes place as soon as the molecular nuclei, from now on called cluster, grows to a critical size. In the following, I only focus on the phase transition from the liquid to the solid state. Ice nucleation may occur in the absence of a foreign substrate, i.e., in pure water or solution droplets, which is referred to as homogeneous ice nucleation (see Sec. 2.1.1). Heterogeneous nucleation (see Sec. 2.1.2) will take place if an INP is present which catalyzes the freezing process. In the following, the most important equations for understanding homogeneous and heterogeneous ice nucleation are derived. On occasion, I refer to the different thermodynamic stages during the supercooling and ice nucleation of a droplet as illustrated in Fig. 2.1.

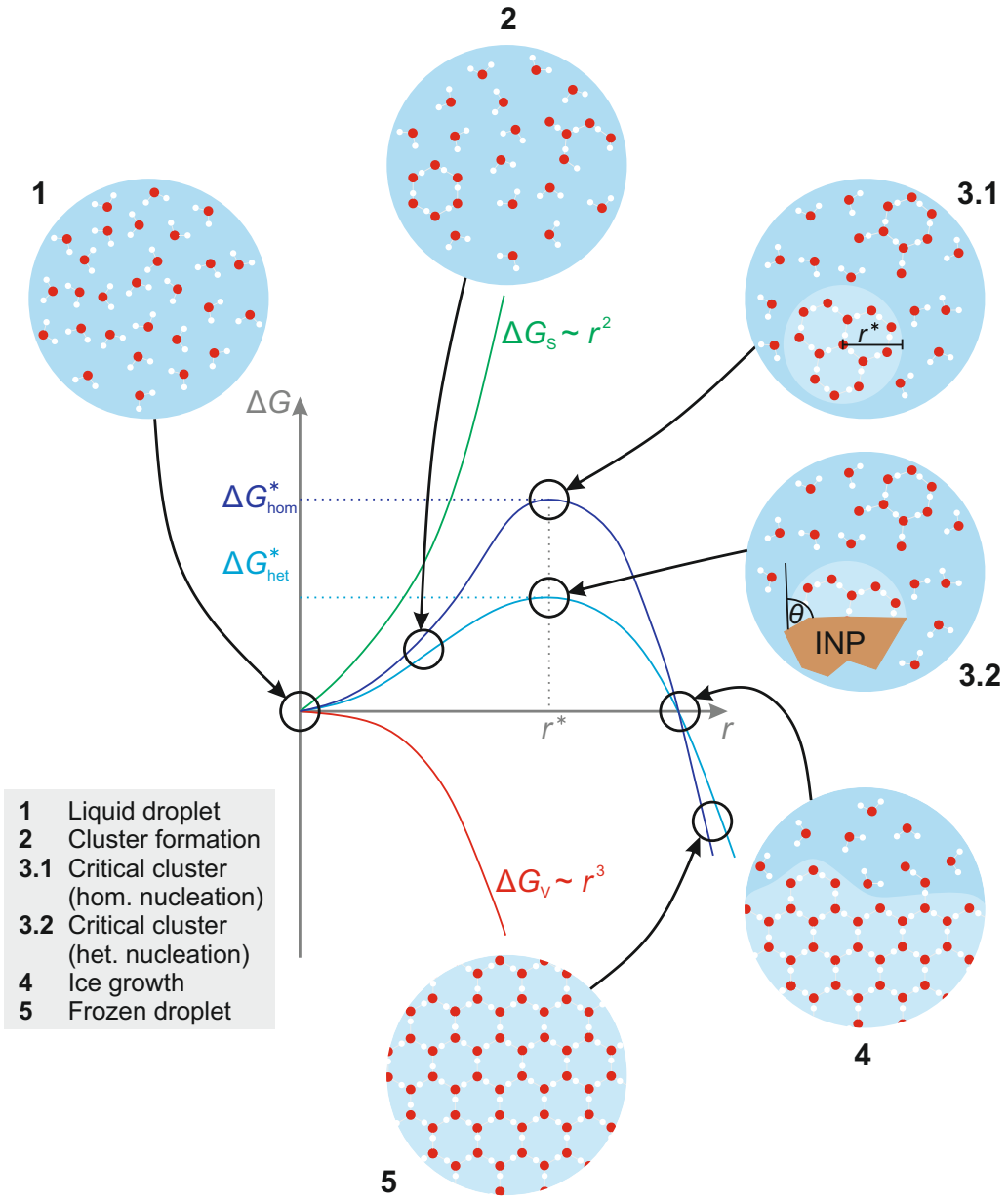

Fig. 2.1.: The center shows the Gibbs free energy change ΔG as a function of cluster radius r. The surface term ΔG_S and the volume term ΔG_V, which add up to ΔG, are included. The surrounding droplets depict different situations during the cooling process. Step 3 represents the formation of a cluster of critical radius r^*. The energy barrier which has to be overcome for nucleation to occur is lower in the case of heterogeneous nucleation (ΔG^*_{het}) compared to homogeneous nucleation (ΔG^*_{hom}). The decrease of the Gibbs free energy barrier can be described with the help of the contact angle θ.

2.1.1 Homogeneous ice nucleation

Considering a single droplet of supercooled water, molecules inside may spontaneously combine to form clusters (see step 2 of Fig. 2.1). The higher the supercooling, the higher the number and the larger the size of the clusters. Ice nucleation spontaneously occurs as soon as one of the clusters exceeds a critical size (see step 3.1 of Fig. 2.1). Classical nucleation theory aims at mathematically describing the rate at which clusters emerge in the liquid phase. In the atmosphere, homogeneous nucleation of pure water or solution droplets takes place below ~ -38 °C (Rosenfeld and Woodley, 2000) which is referred to as the homogeneous nucleation limit. This limit depends on both updraft velocity and cloud droplet size which leads to some variability in the temperature to which supercooled cloud droplets have been observed in the atmosphere (Murray et al., 2012).

The theoretical description of homogeneous ice nucleation starts with calculating the change in free energy of the system caused by the formation of a single cluster. To simplify, the cluster is often considered to be of spherical shape. The change in free energy is referred to as the Gibbs free energy $\Delta G_{\text{hom}}(T)$ and consists of a surface term $\Delta G_{\text{S}}(T)$ and a volume term $\Delta G_{\text{V}}(T)$ (see Eq. (2.1)). $\Delta G_{\text{S}}(T)$ describes the energy required to form an interface between the metastable phase and the stable phase. It depends on the surface area of the cluster $4\pi r^2$ and on the interfacial energy between the liquid (index l) and solid (index i for ice) phases σ_{il}. The energy associated with the difference in chemical potential of the liquid and solid phases is characterized by $\Delta G_{\text{V}}(T)$. Here, $4/3\pi r^3$ is the volume of the cluster, $\nu(T) = m/\rho$ the molecular volume of the solid phase with m and ρ the molecular mass and density of ice, and $S(T) = p_{\text{l}}(T)/p_{\text{i}}(T)$ the ratio of the saturation vapor pressures over liquid water $p_{\text{l}}(T)$ and ice $p_{\text{i}}(T)$, respectively. k_{B} is the Boltzmann constant.

$$\begin{aligned} \Delta G_{\text{hom}}(T) &= \Delta G_{\text{S}}(T) + \Delta G_{\text{V}}(T) \\ &= 4\pi r^2 \sigma_{\text{il}} - \frac{4\pi r^3}{3\nu(T)} k_{\text{B}} T \ln S(T) \end{aligned} \tag{2.1}$$

The center of Fig. 2.1 shows the dominance of $\Delta G_{\mathrm{S}}(T)$ below the critical radius r^* (see Eq. (2.2), from $\frac{\partial}{\partial r}\Delta G_{\mathrm{hom}} = 0$). Until the critical point is reached, energy is required to achieve further growth. As soon as the cluster has grown to r^*, $\Delta G_{\mathrm{V}}(T)$ dominates and the cluster grows while energy in the form of heat is released. The energy barrier $\Delta G^*_{\mathrm{hom}}(T)$ (see Eq. (2.3), from $\Delta G_{\mathrm{hom}}(r^*)$) which has to be surmounted for nucleation to occur is the maximum value of $\Delta G_{\mathrm{hom}}(T)$. A decrease in temperature inevitably leads to a decrease in $\Delta G^*_{\mathrm{hom}}$ and r^* and hence to a larger probability of homogeneous nucleation being triggered.

$$r^* = \frac{2\sigma_{\mathrm{il}}\nu(T)}{k_{\mathrm{B}}T\ln S(T)} \tag{2.2}$$

$$\Delta G^*_{\mathrm{hom}}(T) = \frac{16\pi\sigma^3_{\mathrm{il}}\nu^2(T)}{3(k_{\mathrm{B}}T\ln S(T))^2} \tag{2.3}$$

The next step involves the calculation of the homogeneous nucleation rate coefficient $j_{\mathrm{hom}}(T)$. It describes the number of clusters that grow to a critical size per time interval and droplet volume. It is the product of $w^{\downarrow}(T)$, the diffusive flux of water molecules across the liquid-solid interface, and $n^*(T)$, the number of critical clusters in the liquid phase assuming thermodynamic equilibrium (see Eq. (2.4)). The latter can be described by the number density of molecules in the liquid phase n_{l} (typically $\sim 3.1 \cdot 10^{22}$ m^{-3}; Zobrist, 2006) while assuming the number of clusters to be Boltzmann distributed (see Eq. (2.5)).

$$j_{\mathrm{hom}}(T) = w^{\downarrow}(T) \cdot n^*(T) \tag{2.4}$$

$$n^*(T) = n_{\mathrm{l}} \exp\left(-\frac{\Delta G^*_{\mathrm{hom}}(T)}{k_{\mathrm{B}}T}\right) \tag{2.5}$$

For the transition from liquid to solid to occur, bonds that hold the molecules together in the liquid phase must be broken at first. Subsequently, the water molecules need to re-orientate according to the ice lattice and finally new

bonds with the solid phase need to be created. Hence, nucleation can only take place once the activation energy for diffusion of molecules across the liquid–solid interface $\Delta F(T)$ is put into the system. With this and $k_\mathrm{B}T/h$, which is the quantum mechanical frequency of a molecule at a temperature T where h is Planck's constant, $w^{\downarrow}(T)$ can be written as in Eq. (2.6). Eventually, inserting Eq. (2.5) and (2.6) into (2.4) yields $j_\mathrm{hom}(T)$, the homogeneous nucleation rate coefficient per unit time and droplet volume (see Eq. (2.7)). Some of the parameters in Eq. (2.7), just as $j_\mathrm{hom}(T)$ itself, cannot be measured directly which is why parameterizations are needed (e.g., Zobrist et al., 2007). Alternatively, $j_\mathrm{hom}(T)$ can be derived from measurements of the frozen fraction $f_\mathrm{ice}(T)$, which is the proportion of frozen droplets in a population after a time t at a constant temperature T.

$$w^{\downarrow}(T) = \frac{k_\mathrm{B}T}{h} \exp\left(-\frac{\Delta F(T)}{k_\mathrm{B}T}\right) \tag{2.6}$$

$$j_\mathrm{hom}(T) = \underbrace{\frac{k_\mathrm{B}T}{h} \exp\left(-\frac{\Delta F(T)}{k_\mathrm{B}T}\right)}_{\text{Diffusive flux of molecules}} \cdot \underbrace{n_\mathrm{l} \exp\left(-\frac{\Delta G^*_\mathrm{hom}(T)}{k_\mathrm{B}T}\right)}_{\text{Equilibrium number of critical clusters}} \tag{2.7}$$

Because of the stochastic behavior of nucleation, it is unlikely that all droplets in a population freeze at the same time as soon as a certain temperature value is reached, even if all of them consist of pure water and have the same volume. Pruppacher and Klett (1997) state that a single nucleation event inside a droplet volume V_d is enough to induce freezing of the whole droplet, regardless of its size. This corresponds to a very fast transition from step 3.1 to step 5 in Fig. 2.1 and is reasonable because the growth velocity of ice is very large at the degree of supercooling where homogeneous ice nucleation takes place (Bauerecker et al., 2008). Nonetheless, V_d is of importance because it is more likely to find a critical cluster in a large droplet compared to a small one. If we consider a population of $N = N_\mathrm{f} + N_\mathrm{u}$ droplets of equal size which are all unfrozen at $t = 0$, the change in the number of unfrozen droplets $\mathrm{d}N_\mathrm{u}$ can be written according to Eq. (2.8). Integration from N at $t = 0$ to N_u at t yields Eq. (2.9), assuming that $T =$ const. and $N_\mathrm{u}/N = 1 - N_\mathrm{f}/N$.

$$\mathrm{d}N_\mathrm{u} = - N_\mathrm{u} j_\mathrm{hom}(T) V_\mathrm{d} \mathrm{d}t \tag{2.8}$$

$$f_\mathrm{ice} = \frac{N_\mathrm{f}}{N} = 1 - \exp\left(-V_\mathrm{d} j_\mathrm{hom}(T) t\right) \tag{2.9}$$

By defining a characteristic time $t_\mathrm{c} = (j_\mathrm{hom} V_\mathrm{d})^{-1}$ (time at which $f_\mathrm{ice} = 1 - 1/e \approx 63$ %), it is possible to illustrate the strong effect of temperature on homogeneous ice nucleation. Assuming a droplet size of 20 µm, which has been detected by Rosenfeld and Woodley (2000) between −35 and −40 °C in deep convective clouds, and j_hom from experimental data by Pruppacher (1995), t_c decreases from 24 to 2.4 to $2.4 \cdot 10^{-2}$ s with a change in temperature from −36 to −37 to −38 °C.

2.1.2 Heterogeneous ice nucleation

In mixed-phase clouds, ice particles can exist in a temperature range from 0 to ∼ −38 °C, i.e., well above the limit for homogeneous ice nucleation. In this case, ice formation occurs in the presence of certain solid particles, i.e., INPs, and is referred to as heterogeneous ice nucleation. INPs act as a substrate for ice crystal formation and lower the Gibbs free energy barrier in comparison to homogenous freezing. Only a small fraction of atmospheric aerosol particles, roughly one in a million at −20 °C, are able to trigger heterogeneous ice nucleation (Petters and Wright, 2015). This shows the selectiveness of the ice nucleation process, the reason being that aerosol particles must possess a number of specific features to act as INPs. Some criteria are summarized by Pruppacher and Klett (1997) and include size (the larger the better), solubility (water-insoluble surface), type and strength of chemical bonds (bonds similar to hydrogen bonds of ice lattice), crystallography (small lattice mismatch between INP surface and ice), and active sites (cracks, cavities, edges, or chemical impurities). However, it must be noted that there are no universal rules for assessing whether a material is able to trigger heterogeneous ice nucleation. Laboratory studies under controlled conditions are needed to quantify the ice nucleation efficiency of certain materials and improve the understanding of what makes some aerosol particles efficient INPs.

In the atmosphere, ice particles can form heterogeneously via different pathways, i.e., deposition nucleation, contact freezing, and immersion freezing. Initially, an INP is surrounded by water vapor and the thermodynamic conditions, i.e., temperature and degree of supersaturation of the surrounding air, determine which mechanism will take place. Deposition nucleation is the direct transition from water vapor to ice in a regime which is supersaturated with respect to ice but subsaturated with respect to liquid water. This pathway is known to be more relevant for the formation of cirrus clouds than for the formation of mixed-phase clouds (DeMott, 2002; Lohmann and Diehl, 2006). Note that a pore condensation and freezing mechanism that questions the concept of deposition nucleation was proposed in recent years (Marcolli, 2014; Wagner et al., 2016). Contact freezing can be caused by an INP hitting a supercooled liquid droplet, or by an immersed INP migrating from the inside towards the droplet surface (Durant and Shaw, 2005). There are studies showing that contact freezing is more efficient than immersion freezing, however, the importance of this mechanism for atmospheric ice nucleation is not well understood for lack of field measurements (Ladino Moreno et al., 2013, and references therein). In contrast, immersion freezing, i.e., freezing induced by supercooling of a droplet with an immersed INP, has been shown to be an important mechanism in mixed-phase clouds (Ansmann et al., 2008; de Boer et al., 2011; Westbrook and Illingworth, 2011). Additionally, a mechanism called condensation freezing is mentioned in the literature (Hoose and Möhler, 2012, and references therein). Condensation freezing is defined as a process in which water condenses on the surface of the INP and forms a thin layer which freezes without further temperature decrease, i.e., the underlying process is very similar to immersion freezing. It is not clear whether there is a phenomenological difference between condensation and immersion freezing and whether the two mechanisms should be treated separately (Wex et al., 2014; Vali et al., 2015). In the framework of this thesis, all experiments were conducted in such a way that immersion freezing was investigated. In the following theoretical description, I hence only focus on heterogeneous ice nucleation caused by an immersed particle.

The presence of a solid surface in a supercooled liquid droplet leads to a lowering of the critical Gibbs free energy in comparison to homogeneous nucleation as can be seen in the center of Fig. 2.1. The reason for this lowering is that in the presence of a solid surface less water molecules need to be added to the cluster to reach a critical size (see comparison of step 3.1 and 3.2 in Fig. 2.1). Note that for simplicity, clusters are assumed to

form spherical caps with irregular gaps in between on the surface of the INP (Fletcher, 1959). Mathematically, the decrease of the critical Gibbs free energy can be described with the help of a contact angle model. Forming the product of $\Delta G^*_{\text{hom}}(T)$ and a reduction factor $f(\cos\theta)$ yields the critical Gibbs energy for heterogeneous ice nucleation $\Delta G^*_{\text{het}}(T)$ (see Eq. (2.10)). Here, θ is the angle between the surface of the INP and the surface of the spherical-cap-cluster (see step 3.2 in Fig. 2.1). The reduction factor $f(\theta)$ (see Eq. (2.11) and (2.12)) depends on the interfacial energies between the surface of the INP (index n for nucleus), the surface of the solid phase (index i for ice) and the surface of the liquid phase (index l). Equation (2.12) is known as Young's equation and describes the static equilibrium at the interface of the three phases (Young, 1805). Depending on the contact angle, which is a characteristic value describing the efficiency of an INP, $f(\theta)$ can adopt values from 0 to 1. $\theta = 0°$ yields $f(\theta) = 0$ and nucleation takes place as soon as the droplet becomes supercooled. If $\theta = 180°$ then $f(\theta) = 1$ and heterogeneous nucleation will not be favored over homogeneous nucleation. To summarize, efficient INPs are characterized by small contact angles whereas INPs with large contact angles do not nucleate ice until a temperature close to the homogeneous nucleation limit is reached.

$$\Delta G^*_{\text{het}}(T) = \Delta G^*_{\text{hom}}(T) \cdot f(\theta) \tag{2.10}$$

$$f(\theta) = \frac{1}{2}(2 + \cos(\theta))(1 - \cos(\theta))^2 \tag{2.11}$$

$$\cos(\theta) = \frac{\sigma_{\text{nl}} - \sigma_{\text{ni}}}{\sigma_{\text{il}}} \tag{2.12}$$

According to homogeneous ice nucleation, the heterogeneous nucleation rate coefficient $j_{\text{het}}(T)$, which describes the number of nucleation events per unit time and INP surface area, can be calculated using Eq. (2.13). n_{il} is the number density of water molecules at the interface of critical cluster and supercooled liquid water, typically $\sim 10^{15}$ to 10^{19} m^{-2} (Marcolli et al., 2007; Niedermeier et al., 2010).

$$j_{\text{het}}(T) = \frac{k_{\text{B}}T}{h} \exp\left(-\frac{\Delta F(T)}{k_{\text{B}}T}\right) \cdot n_{\text{il}} \exp\left(-\frac{\Delta G^{*}_{\text{het}}(T)}{k_{\text{B}}T}\right) \tag{2.13}$$

The connection between $j_{\text{het}}(T)$ and $f_{\text{ice}}(T)$ depends on certain assumptions about the properties of the INPs and the droplet population. Since the beginning of the 1950s, there have been two different theoretical approaches for the description of heterogeneous ice nucleation. These are the stochastic (Bigg, 1953a; Bigg, 1953b; Carte, 1956; Dufour and Defay, 1963) and singular approaches (Levine, 1950; Langham and Mason, 1958). In the following, a population of droplets with equal volumes is considered at a constant temperature. Additionally, each droplet shall include the same number of equally sized INPs with identical surface properties.

In case of the stochastic approach, it is furthermore assumed that the presence of the foreign substance does not disrupt the stochastic nature of the freezing process. Hence, each droplet has the same time-dependent freezing probability. The change in the number of unfrozen droplets $\mathrm{d}N_u$ can be calculated according to Eq. (2.14), with A_{n} the INP surface area. Integration from N at $t = 0$ to N_{u} at t for T = const. yields Eq. (2.15), i.e., the equation for $f_{\text{ice}}(T)$. The time-dependence of the nucleation process is clearly shown as there is an increase of f_{ice} over time for T = const. The continued nucleation of droplets which were kept at a constant temperature for a period of time has repeatedly been shown in laboratory experiments (Murray et al., 2011; Broadley et al., 2012; Pummer et al., 2012).

$$\mathrm{d}N_{\text{u}} = -N_{\text{u}} A_{\text{n}} j_{\text{het}}(T) \mathrm{d}t \tag{2.14}$$

$$f_{\text{ice}}(T) = 1 - \exp\left(-A_{\text{n}} j_{\text{het}}(T) t\right) \tag{2.15}$$

The singular hypothesis assumes that clusters preferably form at certain points on the INP surface. Each of these so-called surface sites triggers freezing at its own characteristic temperature T_{c} (Langham and Mason, 1958). The freezing temperature of a droplet is determined by the highest T_{c} of all contained surface sites. Cooling of a droplet population to T_{c} leads to the freezing of a

number of droplets that contain INPs with sites becoming active at or above this temperature. Without further temperature decrease, no other nucleation events will occur, i.e., the number of unfrozen droplets is constant and the nucleation process is time-independent. Connolly et al. (2009) propose Eq. (2.16) for the calculation of n_s, the number of sites which become active per surface area between $T_0 = 0$ °C and a minimum temperature T_{min}. $k(T)$ is the number of sites that become active per surface area and temperature interval dT.

$$n_s = -\int_{T_0}^{T_{min}} k(T)\mathrm{d}T \tag{2.16}$$

The change in the number of unfrozen droplets dN_u in our droplet population is given by Eq. (2.17). Integration from N at T_0 to N_u at T_{min} and insertion of Eq. (2.16) yield a formulation for f_{ice} (see Eq. (2.18)).

$$\mathrm{d}N_u = -N_u A_n k(T)\mathrm{d}T \tag{2.17}$$

$$f_{ice} = 1 - \exp\left(-A_n n_s(T_{min})\right) \tag{2.18}$$

Heterogeneous ice nucleation has been proven to be a stochastic phenomenon to a certain extent. Nevertheless, the nucleation probability may vary among individual particles, even very similar ones, leading to an apparent singular freezing behavior as shown by Niedermeier et al. (2011). As a result, there are several modified descriptions of classical nucleation theory combining benefits from stochastic and singular approaches (Vali and Stansbury, 1966; Marcolli et al., 2007; Vali, 2008; Lüönd et al., 2010; Murray et al., 2011; Niedermeier et al., 2015). Many studies show a very limited time dependence in constant cooling rate experiments for a variety of different INP types (e.g., Broadley et al., 2012; Wright et al., 2013; Budke and Koop, 2015). Therefore, the singular approach was used for the evaluation of immersion freezing data retrieved in the framework of this thesis.

Summary

Ice particles can be formed from the liquid phase via homogeneous nucleation from pure water or solution droplets below ~ -38 °C or via heterogeneous nucleation at higher temperatures. Nucleation occurs as soon as a molecular cluster of critical size has been formed in a supercooled droplet or, in other words, as soon as the free energy barrier for nucleation has been surmounted. Heterogeneous nucleation always involves INPs whose specific properties lead to a decrease of the free energy barrier, i.e., nucleation at lower supercoolings. In general, heterogeneous nucleation is a stochastic, i.e., time-dependent process. However, the time-independent singular approach, which assumes ice nucleation active sites on the surface of the INPs that trigger freezing at certain characteristic temperatures, is representative for many experimental studies and was also used in this thesis.

2.2 Properties of CFA particles

2.2.1 Physicochemical particle properties

A large part of my thesis deals with the physical and chemical characterization of CFA particles, which is why in the following I give an overview about previous investigations in this field. Generally, it is important to know that CFA is a very heterogeneous, multi-component substance. Firstly, this means that for one sample there is a dependency of morphology, chemical composition, and crystallography on the particle size. Secondly, there is large inter-sample variability with respect to the mentioned properties originating from differences in coal petrography, combustion temperature, boiler type, cooling rate, and type of emission control device in different power plants (Ramsden and Shibaoka, 1982).

CFA began to receive much attention from the aerosol research community in the 1970s primarily because of its potentially health-impairing composition (e.g., Davison et al., 1974; Kaakinen et al., 1975; Gladney et al., 1976). These investigations laid the foundation of the current knowledge of trace metal concentration, morphology, crystallography, and size distribution of CFA particles. Flagan and Friedlander (1978) proposed a model of particle formation in coal combustion plumes resulting in a bi-modal size distribution.

The first mode in the size range of several tenths of microns to several microns originates from residual mineral inclusions which melt and form spherical droplets. Volatile components within these droplets can evaporate leading to the formation of hollow *cenospheres* or structures called *plerospheres* (see Fig. 2.2) which are spherical shells filled with many small spherical particles (Fisher et al., 1976). Secondly, particles are formed via nucleation from the gas phase. These particles grow by condensation and coagulation and usually agglomerate to form chain like structures which look very similar to soot particles. The nucleation/condensation mode agglomerates are much smaller than the residual particles, usually in the size range of 1 to 100 nm.

Even though the majority of CFA particles is larger than 1 μm in diameter (Damle et al., 1982), with a broad maximum of the number size distribution in the range from 3 to 50 μm (Ensor et al., 1979; Ensor et al., 1981), submicron particles are of special interest because they have a higher concentration of toxic trace elements than supermicron particles (Davison et al., 1974; Block and Dams, 1976). This is due to the faster cooling rate of small particles compared to larger ones and the favored condensation of elements such as As, Sb, Se, Zn, Pb, and Cd, which are present in the flue gas, onto the small particles. Kaakinen et al. (1975) showed that these elements are detectable to a much smaller extent in coal bottom ash samples. Since the majority of a CFA sample is made up of minerals from inclusions in the coal, it is not surprising that the major elements present in CFA, i.e., Al, Fe, Ca, Si, K, Fe, Na, and Mg can also be found in mineral dust. Traditionally, a classification based on bulk chemical composition emerged from the use of CFA in cement. CFA samples with different compositions have different effects on cement hardening and durability (Canpolat et al., 2004) and the classification is used to estimate which and how much CFA should be added to the cement mixture. According to the American Society for Testing Materials (ASTM, standard C618, 2017), CFA can be characterized into two classes, i.e., F and C. CFA is defined as class F when the combined contents of SiO_2, Al_2O_3, and Fe_2O_3 exceed 70 wt%. CFA is of class C when the combined contents of SiO_2, Al_2O_3, and Fe_2O_3 are between 50 and 70 wt%. Class C CFA typically has a CaO content $\geq$ 20 % causing cementitious (self-hardening when reacted with water) properties. Class F, with a typical CaO content of 1 to 12 wt%, is of pozzolanic nature (self-hardening when reacted with water and portlandite ($Ca(OH)_2$); Ahmaruzzaman, 2010).

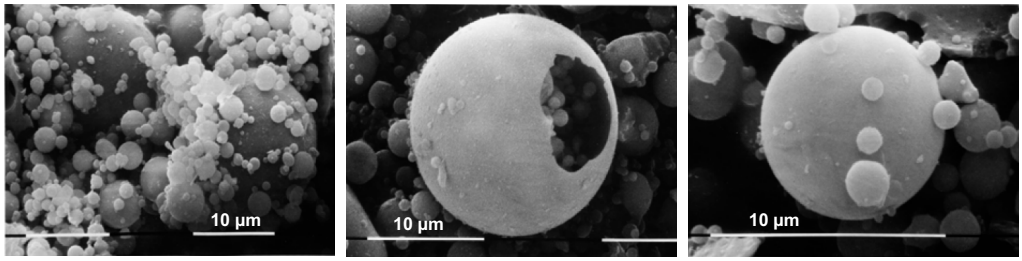

Fig. 2.2.: Scanning electron microscope images of CFA particles from a Bulgarian power plant (Shoumkova et al., 2005).

Concerning crystallography, it must be mentioned that CFA contains between 34 and 80 % of amorphous aluminosilicates, i.e., glass (Vassilev and Vassileva, 2005). The fraction of amorphous material in bulk is dependent on all factors mentioned in the first paragraph of this section, but especially on the coal type. According to Ward and French (2006), CFA from black coal combustion contains a few tens of percent more amorphous material than CFA from brown coal combustion. Additionally, there is indication that the amorphous fraction increases with decreasing particle size, again due to faster cooling rates of the small particles compared to the large ones (Matsunaga et al., 2002). So far over 300 different minerals have been found in the crystalline fraction of CFA samples from all over the world (Vassilev and Vassileva, 2005), among them commonly quartz (SiO_2), mullite ($Al_6Si_2O_{13}$), and hematite (Fe_2O_3; Havlíček et al., 1989). This variability and the overall heterogeneity mentioned above lead to CFA being "one of the most complex anthropogenic materials that can be characterized" (Gianoncelli et al., 2013).

2.2.2 Ice nucleation properties

The following section provides an overview about the state of the art of ice nucleation measurements with CFA. I focus on three recent studies published from 2015 onward (Umo et al., 2015; Garimella, 2016; Grawe et al., 2016) and a study by Havlíček et al. (1993) in which a large number of samples (in comparison to the other studies) was investigated. Earlier investigations (Benson, 1965; Agee, 1971; Schnell et al., 1976; Parungo et al., 1978b; Parungo et al., 1978a) are discussed briefly. Note that very recently, another study (Losey et al., 2018) has been published which is discussed later in comparison to my results (see Sec. 5.1.4). The following paragraphs shall illustrate the scientific situation close to the beginning of my PhD work.

First studies suggesting that aerosol particles from coal-fired power plant plumes could induce heterogeneous ice nucleation date back to the 1960s. Benson (1965) found fog droplets freezing at −35 °C, i.e., above the homogeneous freezing limit, in the heavily polluted air over Fairbanks, AK, USA. The pollution was a result of emissions from coal combustion, car exhausts, and domestic ovens burning various fuels which is why the contribution of CFA particles to heterogeneous ice nucleation could only be speculated on. So-called "industrial snow" events, i.e., snowfall limited to the close proximity of industrial facilities like coal-fired power plants, gave further indication that INPs might be present in the plume aerosol (Agee, 1971). Parungo et al. (1978b) investigated the chemical composition of residual particles from ice crystals formed in a coal-fired power plant plume at −5 °C. They found mainly Si, Al, S, Ca, and Fe which were also major elements in CFA particles from the same power plant and hence came to the conclusion that CFA might trigger heterogeneous ice nucleation in the plume. Ice nucleation measurements with particles sampled directly from coal-fired power plant plumes were initially contradictory as to whether the particles are able to act as INPs (Parungo et al., 1978a) or not (Schnell et al., 1976). Schnell et al. (1976) investigated filter samples from a coal-fired power plant plume in a static diffusion chamber at slight supersaturation with respect to water and compared observed ice nucleation efficiencies with those of filters loaded with background aerosol. They found no difference in the number of ice crystals formed on the two types of filters in a temperature range between −10 and −20 °C. In contrast, Parungo et al. (1978a) described a significantly higher number of ice crystals formed on the filters from the plume by repeating the experiment by Schnell et al. (1976) at a higher supersaturation. Furthermore, they removed volatile, hygroscopic components, which are frequently present in coal-fired power plant plumes, in a vacuum chamber prior to ice nucleation experiments. This procedure led to an increase of registered ice crystals of one order of magnitude compared to the untreated plume filter. Parungo et al. (1978a) concluded that the ice nucleation efficiency of freshly emitted CFA is limited but can be increased by evaporation of the hygroscopic surface layer.

Havlíček et al. (1993) In contrast to the earlier studies, Havlíček et al. (1993) investigated chemical composition and ice nucleation characteristics of CFA not sampled from plume aerosol but from the electrostatic precipitators (ESPs, see Appendix A.1) of nine different power plants in the former Czechoslovakia. They found all samples to trigger heterogeneous ice nucleation. The

chemical composition analysis showed that the water-soluble fraction of the samples varied between 0.43 and 1.34 wt% and mainly consisted of anhydrite (anhydrous $CaSO_4$). Ice nucleation experiments were carried out with two methods. Firstly, polydisperse CFA particles were aerosolized in a thermo-diffusion chamber subsaturated with respect to liquid water at -15 °C, i.e., only deposition nucleation was investigated. Secondly, droplets of CFA–water suspensions were placed onto a cold stage, i.e., immersion freezing was investigated. The water-soluble components were separated from all samples and ice nucleation experiments were carried out with the original samples, the water-insoluble components, and the water-soluble components. Immersion freezing was found to be less efficient than deposition nucleation in all cases. The immersion freezing efficiency of the untreated samples was very variable, i.e., a difference between the least efficient and the most efficient sample of 4 orders of magnitude was observed. The water-insoluble components were up to 3 orders of magnitude less efficient in the deposition mode than the untreated samples. However, when the water-soluble components alone were investigated in the deposition mode, they showed surprisingly low efficiency. This finding illustrates the complex interplay of physicochemical particle properties and freezing behavior, as the water-soluble components increased the ice nucleation efficiency only when associated with the CFA particles but not on their own.

Umo et al. (2015) Four ash samples including CFA, coal bottom ash, wood bottom ash, and bottom ash from a domestic oven were investigated by Umo et al. (2015). The immersion freezing behavior was quantified using the micro-Liter Nucleation by Immersed Particle Instrument (μL-NIPI; Whale et al., 2015) which is a cold stage instrument. In comparison to the bottom ash samples, CFA was more efficient at nucleating ice between -17 and -27 °C, showing a strong increase starting at -16 °C and an apparent plateau below ~ -24 °C. The bottom ash samples behaved similar to each other, with a slight trend of coal bottom ash being less efficient and wood bottom ash being more efficient. Even though analyses with respect to physicochemical particle characterization (bulk crystallography, single particle morphology and chemical composition, particle size distribution) were performed, the question why CFA shows a distinct immersion freezing spectrum could not be answered. Umo et al. (2015) state that the observed differences between bottom ash and CFA must be related to fuel, combustion temperature, chemical composition, and morphology.

Garimella (2016) In the framework of his PhD thesis, Garimella (2016) investigated the freezing behavior of four commercially available CFA samples from the USA using the SPectrometer for Ice Nuclei (SPIN; Droplet Measurement Technologies Inc., Boulder, CO, USA) which is a single particle instrument. The particles were dry-generated and size-selected. Activated fractions (AF, see Sec. 3.2.2) of 1 % were observed at $T < -30$ °C ($1.25 < S_\mathrm{i} < 1.4$) for deposition nucleation and at $T < -20$ °C for immersion freezing. This is contradictory to the measurements by Havlíček et al. (1993) who found deposition nucleation to be more efficient than immersion freezing. Another difference between the results by Havlíček et al. (1993) and Garimella (2016) is the inter-sample variability of the immersion freezing efficiency, which is more than 4 orders of magnitude for the former and very small for the latter. When comparing measurements of CFA by Garimella (2016) and Umo et al. (2015), a discrepancy of more than 1 order of magnitude was found, with the cold stage measurements being below the single particle measurements with SPIN. Garimella (2016) showed that 300 nm particles are more efficient per unit surface area than 700 nm particles, possibly indicating that trace metals, which are enriched in smaller particles, could contribute to the immersion freezing efficiency. This could explain why the results by Umo et al. (2015) were lower, as the size distribution of immersed particles had a mode diameter of ∼10 µm in this study.

Grawe et al. (2016) In the framework of an earlier study resulting from my master's thesis (Grawe et al., 2016), my co-authors and I investigated the immersion freezing behavior of three wood bottom ash samples, one coal bottom ash sample, and one CFA sample. Bulk chemical composition and single particle morphology were also analyzed. The immersion freezing experiments were performed with the Leipzig Aerosol Cloud Interaction Simulator (LACIS; Hartmann et al., 2011), a laminar flow tube in which single, size-selected particles were activated to droplets and subsequently cooled down (see Sec. 3.2.2). It was found that dry-generated CFA particles showed the highest immersion freezing efficiency of the examined samples, being only slightly less efficient below −27 °C than a K-feldspar sample (Augustin-Bauditz et al., 2014). Coal bottom ash was also clearly ice-nucleating, but significantly less efficient than the CFA sample. The wood bottom ash particles showed only limited immersion freezing potential and LACIS results were close to the limit of detection. Interestingly, for the coal ash samples a change in immersion freezing efficiency could be seen in the transition to wet particle generation, i.e., producing CFA–water suspensions

which were sprayed with an atomizer and sent through a dryer. In the case of wet-generated coal bottom ash particles, a decrease towards the limit of detection was observed. The wet-generated CFA particles, however, retained some of their immersion freezing efficiency but virtually no temperature dependence was observed over a range of 10 K. In the course of the work for the here presented PhD thesis, I found that this behavior was caused by a measurement artifact. As a matter of fact, the transition from dry to wet particle generation causes the immersion freezing efficiency of CFA to decrease towards the LACIS limit of detection, just as for coal bottom ash. Please refer to Appendix C for further details which were clarified in the framework of this thesis. As the size of dry- and wet-generated particles in the LACIS experiments was identical, the size-dependent enrichment of trace elements suggested by Garimella (2016) could not be the reason for the observed discrepancy. We rather assumed that physicochemical particle properties were changed in suspension resulting in a lower ice nucleation efficiency. For lack of single particle chemical composition information in Grawe et al. (2016), it was not possible to identify species that could potentially contribute to the ice nucleation activity of dry-generated CFA or cause the decrease of the immersion freezing efficiency in suspension.

Summary

Generally, CFA is a very heterogeneous substance with respect to differences between single particles of one sample and between bulk samples of different origin. This heterogeneity of the physicochemical particle properties leads to a strong variability of the immersion freezing properties. Figure 2.3 shows a comparison of immersion freezing results from Umo et al. (2015), Garimella (2016), and Grawe et al. (2016). A comparison to Havlíček et al. (1993) was omitted here, because in this study no specific surface area is given which would be needed for the calculation of $n_s(T)$. It can be seen that experiments performed with different CFA samples and different instruments show a variability of 3 orders of magnitude (difference between Grawe et al., 2016, and Umo et al., 2015, at -31 °C). So far, it is unclear how large the respective contributions of differences in physicochemical particle properties and differences in methodology are to the variability within the sparse data set. In conclusion, previous investigations did not lead to conclusive findings concerning relevant properties and processes influencing the immersion freezing behavior of CFA particles.

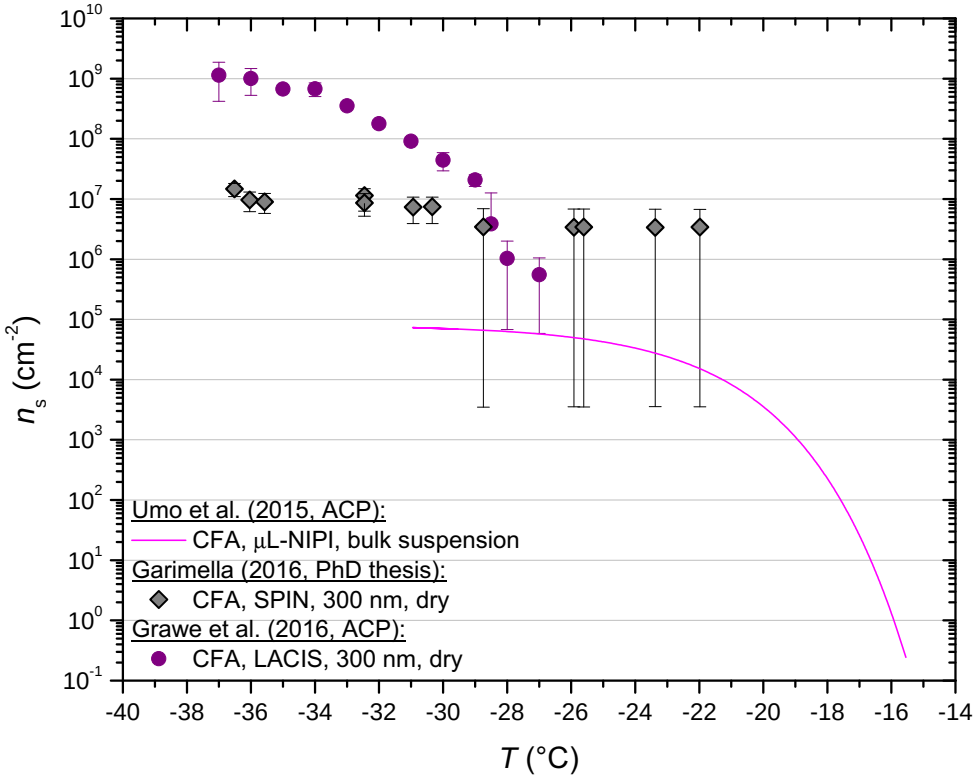

Fig. 2.3.: Overview of $n_s(T)$ from previous immersion freezing measurements with CFA samples of different origin.

3 Materials and Methods

In this chapter, I introduce the investigated CFA samples and additional materials that were used for the immersion freezing experiments. The techniques for physicochemical particle characterization and immersion freezing experiments are described. For some instruments and methods, more detailed explanations can be found in the Appendix.

3.1 Materials

The CFA samples were taken from the electrostatic precipitators (ESPs) of four coal-fired power plants in Germany. Note that depending on the configuration of flue gas desulfurization (FGD; see Srivastava and Jozewicz, 2001, for a review of techniques) and ESP systems in the power plants, CFA samples taken from the ESP might differ substantially from CFA particles that escape into the atmosphere in terms of physicochemical particle properties. In the framework of my thesis, it was not possible to evaluate if particles from the ESP are representative for CFA in the atmosphere because it is not known which FGD technique is applied in the power plants or whether the ESPs are installed up- or downstream of the FGD systems. This technical information could either not be obtained from the power plant operators, or is unknown because the samples were transferred via an intermediary who kept the power plants of origin anonymous.

CFA1 is identical to the CFA sample from Grawe et al. (2016) and originates from the Lippendorf power plant situated 15 km south of Leipzig, Germany. CFA1, CFA2, and CFA4 are from brown (sub-bituminous) coal combustion, CFA3 is from black (bituminous) coal combustion. Differences between the samples, i.e., color, grain size, and the amount of partially combusted material, can already be seen with the naked eye (see Fig. 3.1).

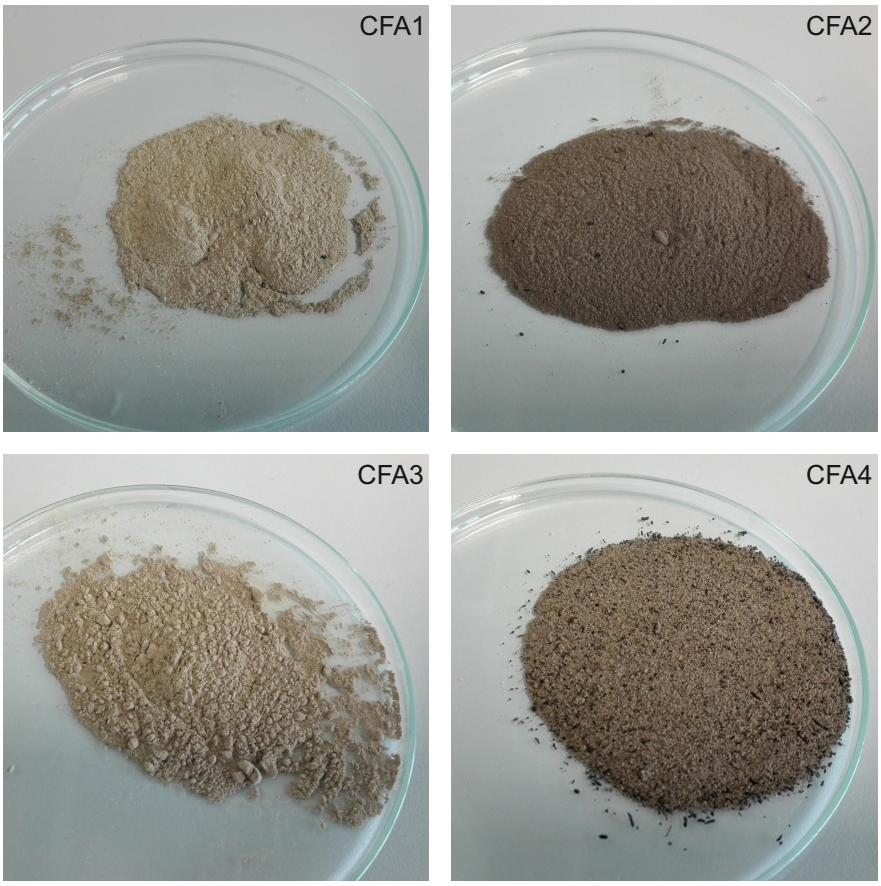

Fig. 3.1.: Photographs of the four CFA samples as received from the power plants.

In addition to the CFA samples, immersion freezing was also tested for particles of anhydrite, quicklime (CaO), and gypsum ($CaSO_4 \cdot 2H_2O$) from Merck KGaA (Darmstadt, Germany).

3.2 Methods

Part of the immersion freezing and particle characterization measurements of the CFA samples were performed during a campaign at the Leibniz Institute for Tropospheric Research (TROPOS) in Leipzig, Germany, in November 2016 together with collaborators from the Ice Nuclei research UnIT (INUIT). The main setup (see Fig. 3.2) consisted of particle generation, size selection, and distribution of the size-selected aerosol to the following instruments: 1) LACIS, 2) SPIN, 3) the Aircraft-based Laser ABlation Aerosol MAss spectrometer (ALABAMA), and 4) the Multi-Micro INertial Impactor (Multi-MINI), which sampled particles onto substrates for environmental scanning electron

microscopy coupled with energy dispersive X-ray spectroscopy (ESEM/EDX). In addition to LACIS and SPIN, immersion freezing measurements were performed with two cold stage setups: 1) the Leipzig Ice Nucleation Array (LINA), and 2) the WeIzmann Supercooled Droplets Observation on Microarray (WISDOM) setup. For this, CFA–water suspensions were prepared using the bulk material, which is why further bulk analyses regarding morphology (BET: Brunauer-Emmett-Teller specific surface area determination), chemical composition (ICP-SFMS: inductively coupled plasma–sector field mass spectrometry), crystallography (XRD: X-ray diffraction analysis), and others were performed following the campaign. Instrument availability or technical issues were the reasons why not all CFA samples were investigated using all possible analysis methods. Table 3.1 gives an overview of the CFA samples and performed analyses.

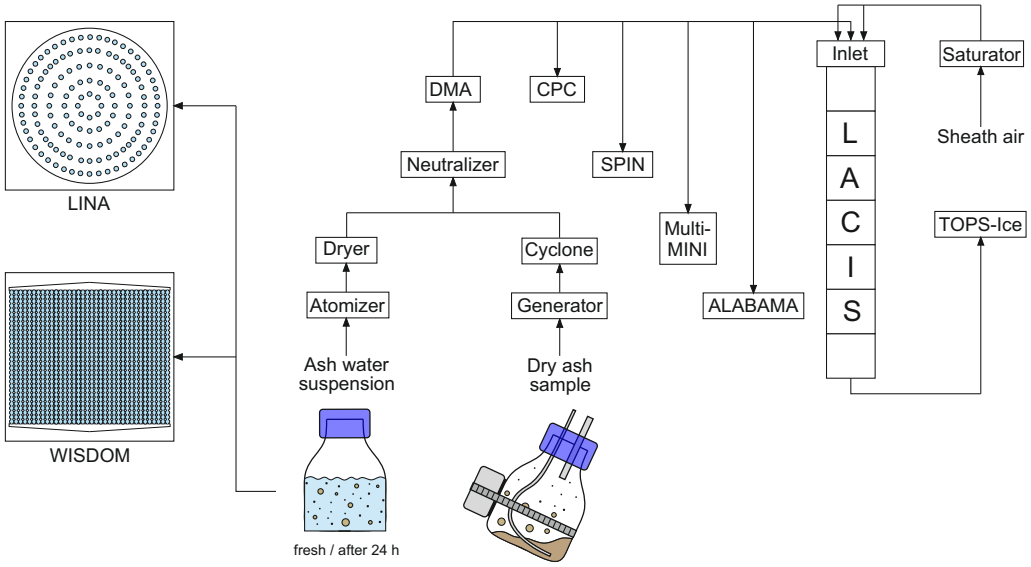

Fig. 3.2.: Experimental setup during the INUIT campaign in November 2016.

Table 3.1.: Overview of CFA samples with respect to performed immersion freezing and particle characterization measurements. PG stands for particle generation.

		Physicochemical sample characterization					Immersion freezing investigations			
Sample	PG	ALABAMA	ESEM/EDX	XRD	ICP-SFMS	BET	LACIS	SPIN	LINA	WISDOM
CFA1	dry	✓	✓	✓	✓	✓	✓	✓	–	–
	wet	✓	✓	✓	–	–	✓	✓	✓	✓
CFA2	dry	✓	✓	✓	✓	✓	✓	✓	–	–
	wet	✓	✓	✓	–	–	✓	–	✓	–
CFA3	dry	✓	✓	✓	✓	✓	✓	✓	–	–
	wet	✓	✓	✓	–	–	✓	–	✓	–
CFA4	dry	✓	✓	✓	✓	✓	✓	✓	–	–
	wet	✓	✓	✓	–	–	✓	–	✓	–

3.2.1 Sample preparation and particle generation

Dry particle generation

The dry CFA samples were placed into an aerosol generator operating via pressurized air and an electric imbalance motor (see Fig. 3.2 and Grawe et al., 2016). The samples were not sieved prior to aerosol generation. The aerosol was sent through a mixing bottle and a cyclone (D_{50} = 500 nm) to reduce the amount of large particles in the flow. Further downstream, a neutralizer was passed, before a differential mobility analyzer (DMA, Vienna type, medium) was used for size selection. A mobility diameter of 300 nm was chosen for the immersion freezing experiments with LACIS and SPIN for several reasons. Firstly, ESPs have a minimum collection efficiency for particle sizes between 0.2 and 2 µm (see Appendix A.1), meaning that CFA particles in this size range are more likely to be emitted compared to smaller or larger particles. Secondly, 300 nm particles will experience relevant atmospheric residence times once emitted (Jaenicke, 1978). Finally, 300 nm was the size at which sufficiently high and stable particle number concentrations could be generated for all samples with both particle generation methods.

Afterwards, the quasi-monodisperse aerosol was distributed to a condensation particle counter (CPC, model 3010, TSI Inc., St. Paul, MN, USA), LACIS, SPIN, Multi-MINI, and ALABAMA. The term "quasi-monodisperse" implies that the distributed aerosol contained singly-charged particles of the selected size (300 nm) and, additionally, larger multiply-charged particles with the same electrical mobility. As the aim of the single particle immersion freezing measurements was the investigation monodisperse 300 nm particles, the results needed to be corrected according to the particle size distribution after size selection. This so-called multiple charge correction was performed using ALABAMA measurements of the vacuum aerodynamic diameter. The method and results are described in detail in Appendix B.1.

Suspension preparation and wet particle generation

The CFA–water suspensions for LACIS, SPIN, and LINA measurements were prepared following the description by Umo et al. (2015). Briefly, a certain amount of CFA was mixed with distilled water (LINA: 0.1 g CFA in 100 mL

water, LACIS and SPIN: 0.5 g CFA in 100 mL water) and ultrasonicated (RK100H Sonorex Super, BANDELIN electronic GmbH & Co. KG, Berlin, Germany) for 10 min. Afterwards, the suspension was stirred with a magnetic stirrer for 24 h and then either used for pipetting droplets onto LINA or for wet particle generation. This approach was chosen to allow comparability to results by Umo et al. (2015) and Grawe et al. (2016). Furthermore, the procedure helps breaking up large aggregates and prevents fast sedimentation that would lead to an uneven distribution of material in the droplets on LINA. As sedimentation was no limiting factor for wet particle generation with LACIS (a flask shaker was used), measurements were performed with both the standard suspensions (ultrasonification and 24 h stirring) and suspensions that were prepared right before the experiment by simply mixing 0.5 g CFA with 100 mL distilled water. In this way, particles were in suspension for less than 5 min before being used for LACIS measurements. The suspensions, either fresh or standard, were sprayed with an atomizer (similar to Model 3076, TSI Inc., St. Paul, MN, USA) and the resulting droplets were sent through a diffusion dryer. Then, size selection of the particles by the DMA (300 nm) and distribution to LACIS, SPIN, CPC, Multi-MINI, and ALABAMA took place. Due to instrument availability, SPIN measurements could only be performed with the standard suspensions of CFA1.

In contrast to LINA measurements, a rough size selection of the CFA samples was necessary for WISDOM because large particles that are present in the original sample would clog the microfluidic device which is used for droplet production (see Sec. 3.2.2). Size selection was realized by running dry particle generation (aerosol generator, mixing bottle, cyclone) for several hours and collecting the accumulated material from the cyclone (D_{50} = 450 nm). During this procedure, coarse material was deposited in the mixing bottle and a sub-fraction of the bulk, hereafter referred to as fine CFA, remained in the cyclone. Suspensions of 0.1 g fine CFA in 100 mL distilled water were mixed for 3 cycles of 30 s each with 10 s break in a small volumes sonicator (UP200St, Hielscher Ultrasonics GmbH, Teltow, Germany) and were used for droplet production and immersion freezing experiments with WISDOM within 2 min.

3.2.2 Immersion freezing instrumentation

Single particle methods

LACIS is a vertically aligned, laminar flow tube consisting of seven 1 m long sections, each temperature controlled by individual thermostats. At the inlet, which is situated at the top of the tube, the aerosol flow is enclosed by a humidified sheath flow. As a result, a stable 2 mm wide particle beam is created along the LACIS centerline, ensuring that all particles experience identical thermodynamic conditions. In an immersion freezing experiment, high supersaturation with respect to water is created by adjusting the dew point of the sheath air and the wall temperature of the two lowermost sections. Like this, it is certain that each particle is activated to a droplet before it adapts to the set wall temperature close to the outlet. The ice nucleation time in LACIS is 1.6 s which is fast in comparison to other immersion freezing instrumentation (Wex et al., 2015). Prior to each measurement, a cooling routine is initiated resulting in the coverage of the wall of the two lowermost tube sections with a thin ice layer. This is a necessary step to ensure reproducible conditions. Note that an experiment usually needs to be terminated after ∼30 min because the ice layer serves as a water vapor sink and grows in thickness, causing large ice particles to break off.

Supercooled liquid droplets and ice particles coexist at the outlet of the tube in a certain temperature range above the homogeneous freezing limit. The Thermo-stabilized Optical Particle Spectrometer for the detection of Ice (TOPS-Ice; Clauß et al., 2013) is used to automatically determine the phase state of the hydrometeors and from this f_{ice} (number of frozen hydrometeors divided by total number of hydrometeors). The measurement principle exploits the difference in scattering properties, i.e., depolarization, between freshly frozen ice particles, which are not perfectly spherical, and spherical liquid droplets.

At least 2000 hydrometeors were classified for each LACIS data point presented in this thesis. The only exception to this is the measurement with the fresh CFA3 suspension, where, due to low particle number concentrations, only ∼500 hydrometeors were considered (see Fig. 5.9). Occasionally, three or more data points of separate measurements under the same conditions were averaged. In these cases, the f_{ice} error is indicated by the standard deviation of the separate measurements. Otherwise, a Poisson error is given depending on the total number of classified hydrometeors in a single mea-

surement. The temperature error of ± 0.3 K is defined by the temperature stability of the thermostats. n_s was calculated according to Eq. (2.18) assuming the particle surface area to be equal to the surface area of a sphere with a diameter of 300 nm.

SPIN is a continuous flow diffusion chamber with a parallel plate geometry which has been described in detail by Garimella et al. (2016). Figure 3.3 shows the flow velocity, saturation ratio, and vapor pressure in the ice nucleation chamber as a function of temperature. Due to a temperature difference of the ice-coated walls, heat and water vapor diffuse from the warm (here −30 °C) to the cold wall (here −40 °C) and supersaturation with respect to ice (light orange area) is created. If the temperature gradient between the walls is large enough, as in the given example, aerosol particles, which are constrained in a so-called lamina by two surrounding sheath flows, will experience supersaturated conditions with respect to liquid water (dark orange area). Hence, aerosol particles will be activated to cloud droplets as they travel along the lamina and immersion freezing can be investigated. To simplify the discrimination between ice particles and supercooled liquid droplets, the hydrometeors are sent through an evaporation section before reaching particle detection. In the evaporation section, the cold wall temperature is increased to the warm wall temperature. Under these circumstances the air is subsaturated with respect to water but saturated with respect to ice and the droplets evaporate while the ice particles persist. Ideally, dry aerosol particles and significantly larger ice particles are present at the outlet of the evaporation section.
In contrast to f_{ice}, the fraction of particles active as INPs, the activated fraction AF, is calculated by dividing the number of ice particles detected with an optical particle counter (OPC) by the total number of aerosol particles measured with a CPC (model 3772, TSI Inc., St. Paul, MN, USA) at the inlet. A threshold size of 3 µm was used to identify ice crystals in the OPC signals. The uncertainty in AF is 14 % resulting from the uncertainties of the CPC and the OPC. The temperature uncertainties represent the highest and lowest deviations from the average lamina temperature in the chamber. When compared to LACIS measurements, SPIN data provide information on how immersion freezing results are affected by the different residence times in the two instruments. The ice nucleation times in SPIN depend on the thermodynamic conditions in the chamber and are between 8 and 12 s, i.e., ∼factor 6 longer than in LACIS. In addition to the cyclone used in the dry particle generation method, an impactor (0.071 cm orifice, TSI Inc., St.

Paul, MN, USA) with $D_{50} = 500$ nm was used upstream of the SPIN inlet to minimize the amount of multiply-charged particles in the sample aerosol. This justifies the assumption of an almost monodisperse aerosol at the SPIN inlet and hence the omission of a multiple charge correction of the SPIN data.

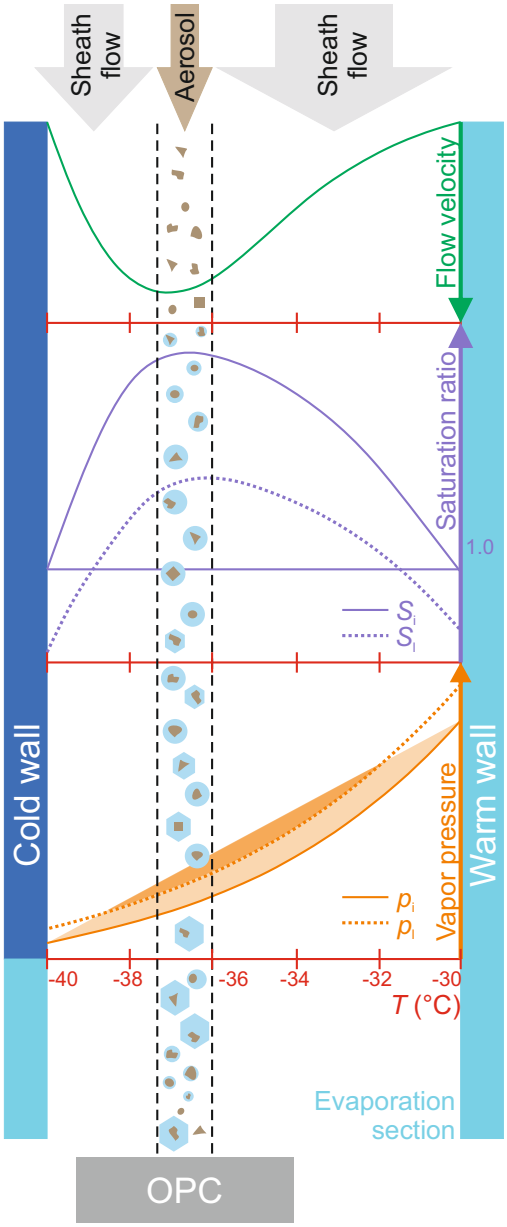

Fig. 3.3.: Setup of the SPIN ice nucleation chamber and evaporation section. Flow velocity, saturation ratios with respect to liquid water and ice (S_l, S_i), and saturation vapor pressures over liquid water and ice (p_l, p_i) are shown as a function of temperature. The light and dark orange areas correspond to supersaturation with respect to ice and water, respectively. The black dashed lines are the borders of the aerosol lamina. Adapted from Stetzer et al. (2008).

Cold stage methods

LINA is a cold stage setup based on the Bielefeld Ice Nucleation ARraY (BINARY; Budke and Koop, 2015). 90 suspension droplets, each 1 µL in volume, are placed into separate compartments onto a circular, hydrophobic glass slide (see Fig. 3.4 a). The compartments, realized by a perforated aluminum plate covered with a second glass slide, prevent interaction between the droplets, e.g., via the Wegener-Bergeron-Findeisen process or splintering while freezing. Also, the compartments suppress evaporation of the droplets. A cryostage (LTS120, Linkam Scientific Instruments, Waterfield, UK) with a 40 x 40 mm^2 Peltier element is used for cooling the droplet array at a rate of 1 K min^{-1}. The cryostage is coupled to a water-circulator (C25P thermostat, HAAKE GmbH, Karlsruhe, Germany) which is set to 10 °C to enable cooling to below −25 °C. A thin layer of squalene oil on top of the Peltier element guarantees direct contact to the glass slide and improves heat transfer away from the droplets. Nonetheless, a temperature calibration of the instrument is necessary (see Appendix B.2). The droplet array is situated in an aluminum housing which is purged with particle free, dry air during the experiment.
The determination of f_{ice} is almost fully automated. A charge-coupled device camera surrounded by an LED dome light (see Fig. 3.4 b) takes images every 6 s which is equal to a temperature resolution of 0.1 K at a cooling rate of 1 K min^{-1}. Parts of the LED light are shielded with a cardboard ring to cause ring-shaped structures being reflected from the liquid droplets. As the reflective properties of a droplet change upon freezing, the reflection of the ring vanishes directly after the phase change. The images (see Fig. 3.4 c), each relating to a certain temperature, are later imported into a computer program based on the OpenCV HoughCircles algorithm (Bradski and Kaehler, 2008) that detects the number of rings. From this, $f_{\text{ice}}(T)$ can be derived.
Freezing caused by impurities in the distilled water and on the glass slide was accounted for in the following way: Firstly, the cumulative number of sites active at a given temperature T per droplet volume V_{d} was calculated for the distilled water that was used to prepare a CFA suspension ($K_{\text{H}_2\text{O}}(T)$; Eq. (3.1); Vali, 1971) and for the respective CFA suspension ($K_{\text{CFA}}(T)$; Eq. (3.2)). Secondly, a corrected $n_{\text{s, corr}}$ value was calculated according to Umo et al. (2015; see Eq. (3.3)). Here, C is the mass concentration of CFA in the suspension and A_{BET} is the BET specific surface area.

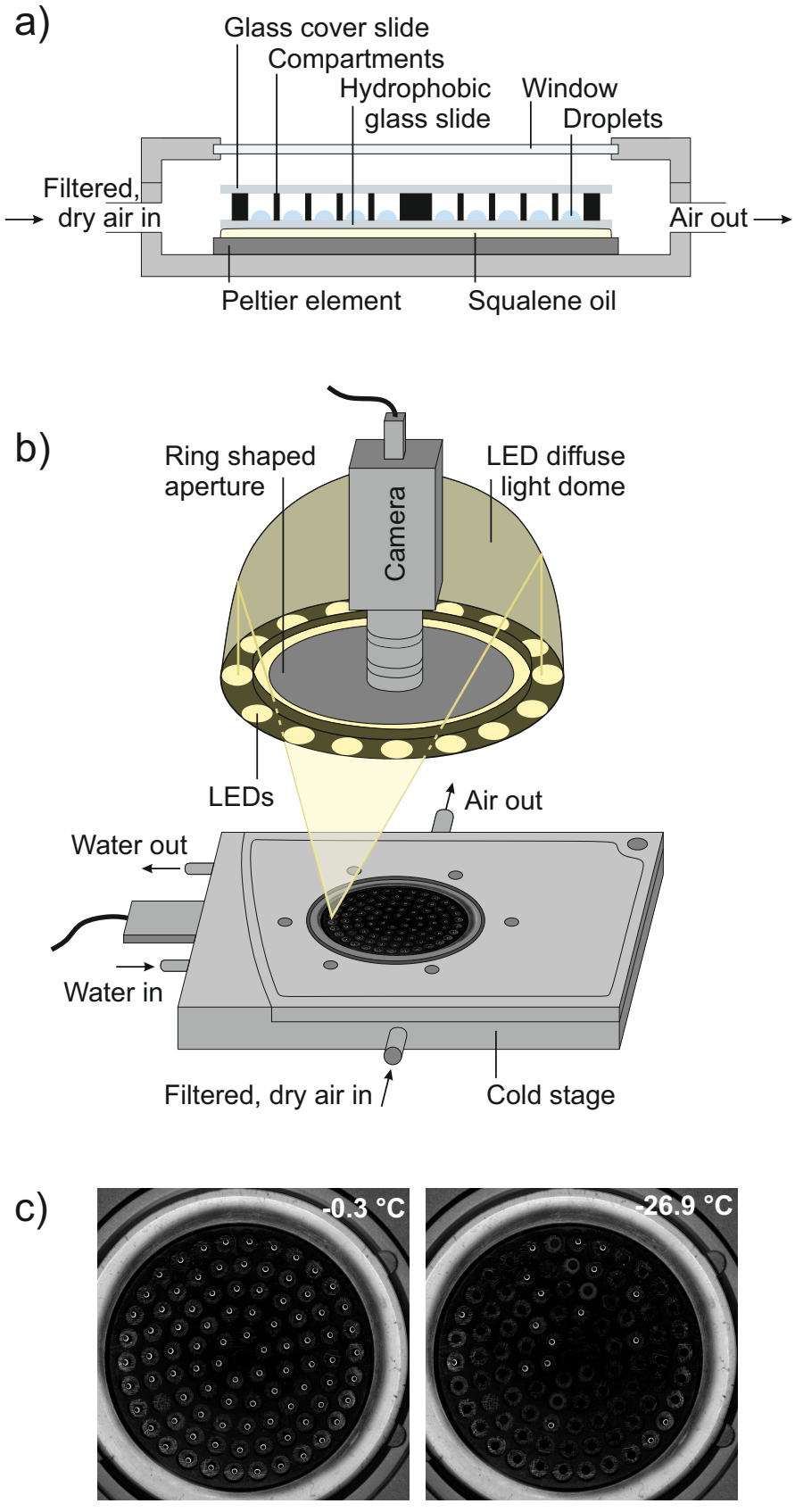

Fig. 3.4.: a) Side view of the LINA cold stage device with droplet array. b) Overview of the setup with cold stage, light dome, and camera. c) Example images with $f_{\text{ice}} = 0$ (left) and $f_{\text{ice}} = 0.8$ (right).

$$K_{\mathrm{H_2O}}(T) = -\frac{\ln\left(1 - f_{\mathrm{ice,\,H_2O}}(T)\right)}{V_\mathrm{d}} \tag{3.1}$$

$$K_{\mathrm{CFA}}(T) = -\frac{\ln\left(1 - f_{\mathrm{ice,\,CFA}}(T)\right)}{V_\mathrm{d}} \tag{3.2}$$

$$n_{\mathrm{s,\,corr}}(T) = \frac{K_{\mathrm{CFA}}(T) - K_{\mathrm{H_2O}}(T)}{C \cdot A_{\mathrm{BET}}} \tag{3.3}$$

Values of $n_{\mathrm{s,\,corr}}$ from four measurements were averaged resulting in a mean n_s value, i.e., a total number of 360 droplets was investigated for each sample. The uncertainty of the average n_s, given as vertical error bars in Sec. 4.2.2 and 5, is equal to the standard deviation of the four $n_{\mathrm{s,\,corr}}$ values. The largest possible n_s error of the LINA measurements is illustrated in Fig. 3.5. For this, the uncertainties from weighing of the CFA sample, pipetting of the distilled water and the CFA suspension, measurement of the BET specific surface area, and Poisson distribution of the particles in the suspension were propagated.

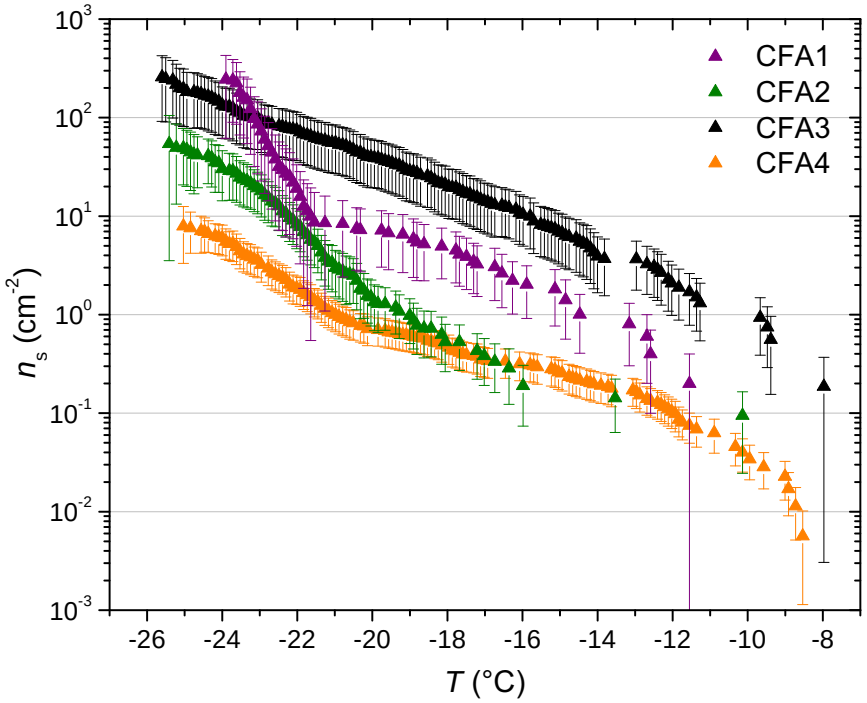

Fig. 3.5.: $n_\mathrm{s}(T)$ from LINA measurements. Vertical error bars are the result of propagating uncertainties in weighing, BET surface area, pipette volumes, and distribution of particles in the suspension.

WISDOM is a cold stage for investigating monodisperse nanoliter droplets and was developed at the Weizmann Institute of Science in Rehovot, Israel (Reicher et al., 2018). It was used to study the immersion freezing behavior of the fine CFA fraction. The droplets are produced by a microfluidic device and subsequently arrange into an array of chambers based on the method described by Schmitz et al. (2009; see Fig. 3.6 a). The droplets are suspended in an oil mixture, consisting of mineral oil (Sigma Aldrich, St. Louis, MO, USA) stabilized with 2 wt% nonionic surfactant (span80®, Sigma Aldrich, St. Louis, MO, USA). The microfluidic device is fabricated in the laboratory from polydimethylsiloxane (PDMS) and attached to a 1 mm microscope slide using oxygen plasma treatment. The microscope slide with the PDMS droplet array is then transferred to a cryostage (THMS600, Linkam Scientific Instruments, Waterfield, UK) by placing it onto a thin oil layer on top of the silver block cooling element (see Fig. 3.6 b). Experiments are conducted at a cooling rate of 1 K min^{-1} while the housing is purged with dry N_2 gas. Freezing is observed by a microscope (BX51 with 10x objective and transmission mode, Olympus Optical, Tokyo, Japan) and detected for each droplet individually when the optical brightness of the droplet decreases due to the formation of ice crystals. Pure water droplets within the device can be supercooled to below -35 °C, where first freezing occurs, i.e., above this temperature no correction regarding background INPs is necessary. The temperature calibration of WISDOM is realized by the observation of melting of aqueous and eutectic solutions with defined melting points. The temperature uncertainty is $\pm$ 0.34 °C.

n_s was determined according to Eq. (3.4), with the droplet volume $V_d = 478$ $\pm$ 78 pL, the BET specific surface area of the fine CFA fraction A_{BET}, and the concentration of CFA in suspension C. The n_s error was estimated by propagating the uncertainties in the measurements of V_d and A_{BET}, and the Poisson distribution of particles in suspension.

$$n_s(T) = -\frac{\ln(1 - f_{ice}(T))}{V_d \cdot A_{BET} \cdot C} \tag{3.4}$$

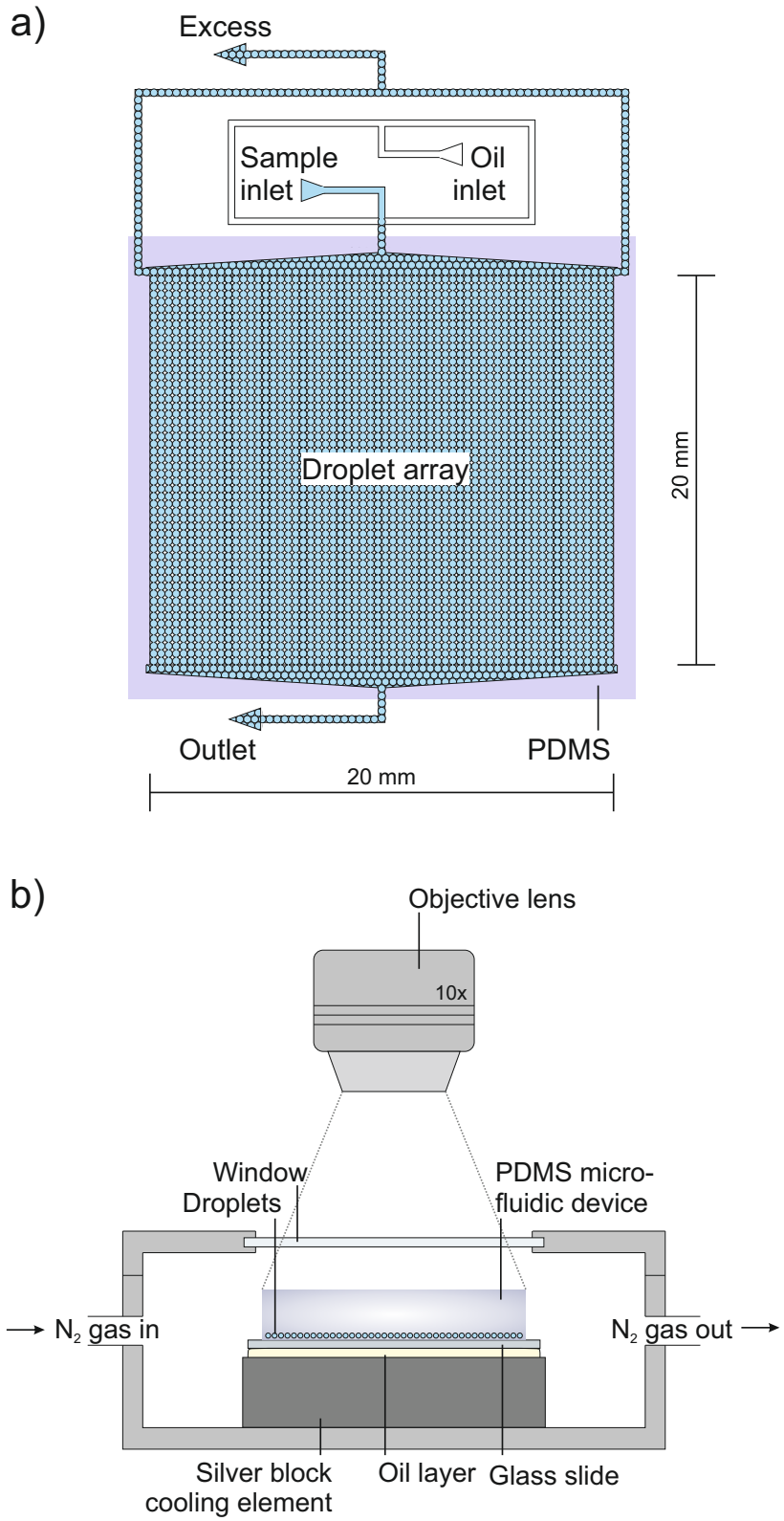

Fig. 3.6.: a) Top view of polydimethylsiloxane (PDMS) microfluidic droplet array. Adapted from Schmitz et al. (2009). b) Side view of cold stage with microfluidic device and objective lens.

3.2.3 Physicochemical sample characterization

Single particle methods

ALABAMA is a single particle mass spectrometer which was originally developed for aircraft operation (Brands et al., 2011) at the Max Planck Institute for Chemistry in Mainz, Germany, but is also used in ground-based campaigns (Roth et al., 2016; Schmidt et al., 2017). Please refer to Appendix A.2 concerning the instrumental setup.
Several thousand single particle mass spectra were analyzed for each CFA sample. The chemical compounds contained in the submicron particles were investigated by calculating the signal average for every mass-to-charge ratio. Note that different ions can occur on one mass-to-charge ratio. The averaged mass spectra must always be regarded in conjunction with the relative abundance, i.e., the information how many of the investigated particles contain a certain species. For the determination of the relative abundance, only particle related signals should be considered. Therefore, signal thresholds were derived by averaging ∼1900 background spectra (without particles) to exclude signals which originate from, e.g., molecules evaporating from surfaces, vacuum grease, or remaining air molecules. Threshold values for anions (21.6 ± 5.1 mV) and cations (8.2 ± 0.8 mV) were derived by averaging the means of the mass-to-charge ratios plus five times their standard deviation over all background spectra. In case the signal intensity at a certain mass-to-charge ratio was above (below) the threshold, the particle was classified as (not) containing this species. The averaged mass spectra include all signals regardless of whether the signals of the mass-to-charge ratios were above or below the mentioned thresholds.

ESEM/EDX analysis was performed on particles sampled onto substrates with the Multi-MINI (Ebert et al., 2016; see Appendix A.3), which was developed at the Darmstadt University of Technology (Darmstadt, Germany). One stage with $D_{50} = 1$ µm was used for particle collection behind the DMA. Sampling durations ranged from 30 s to 6 min, depending on average particle number concentrations of the different samples (80 to 300 cm^{-3}). Chemical composition, size, and morphology were investigated with a Quanta 400 FEG ESEM (FEI Company, Hillsboro, OR, USA). No coating was applied to the substrates prior to the ESEM/EDX investigations. Particles impacted on the substrate located in the impaction spot were randomly selected for

analysis. Chemical elements with an atomic number larger than 5 were detected with an EDX detector and analyzed with AZtec software (version 3.3 SP1, Oxford Instruments, Abingdon, UK). All measurements were carried out with 12.5 keV, 10 mm working distance, and 20 s acquisition time per particle.

Light microscopy images of liquid CFA suspension droplets were taken with a digital camera coupled to an optical microscope (Primovert, Carl Zeiss Microscopy GmbH, Jena, Germany). The magnification was 200x and unpolarized light was used. The suspensions were prepared in the same way as for the LACIS measurements (see Sec. 3.2.1) and pipetted onto a glass microscope slide. A second slide was put on top of the liquid droplet to increase the amount of particles in focus and to avoid evaporation. This investigation was performed because CFA particles have earlier been shown to change their morphology after contact with water (Grawe et al., 2016). So far, it was unclear whether these changes occur in the aqueous environment or due to drying of the droplets.

Bulk methods

XRD analyses were performed with both dry particles and suspension particles for the crystallographic characterization of the CFA samples. Dry particles were ground using mortar and pestle before being pressed into a sample holder as densely as possible. CFA suspensions were prepared as for the LACIS measurements (see Sec. 3.2.1) and then left in a desiccator (steady flow of particle-free, dry air) until all water was evaporated. The remaining dry powder was pressed into a sample holder. Both procedures were applied to all four samples, resulting in eight measurements. A Bragg-Brentano diffractometer with a Cu anode (Philips X'Pert, PANalytical, Almelo, the Netherlands) was used to perform 2Theta-Omega scans from 10° to 70° with a step size of 0.03° and an integration time of 20 s. Quantitative phase identification was done by Rietveld refinement using reference patterns from the Crystallography Open Database (Gražulis et al., 2009).

ICP-SFMS was used for the bulk chemical composition analysis at ALS Scandinavia AB (Luleå, Sweden). This technique is widely applied for trace element determination because of the low limit of detection (Zheng and

Yamada, 2006). In the framework of this thesis, measured mass fractions of major ions were recalculated into their most common oxide forms. Note that mass fractions of oxides and trace elements do not necessarily add up to 100 % because other than the investigated elements might be present in the samples or other counterions might be involved. For example, apart from K_2O, K may also occur in the form of KCl or K_2CO_3.

LOI (loss on ignition) values were determined at ALS Scandinavia AB by heating a defined amount of the CFA samples to 1000 °C and comparing pre- and post-ignition weights. LOI values are proportional to the amount of unburnt fuel resulting from incomplete combustion in the power plants. This residual material is presumably made up of carbonaceous particles.

Water activity measurements of the CFA suspensions were performed to make sure that freezing point depression would not influence the cold stage measurements. A 4TE AQUALAB device (Meter Group Inc., Pullman, WA, USA) was operated at the University of Aarhus (Aarhus, Denmark) for the determination of the water activity of the CFA suspensions.

pH values of the CFA suspensions were determined with standard pH-indicator strips (Merck KGaA, Darmstadt, Germany).

BET measurements, i.e., the determination of the specific surface area of the four CFA samples, were performed by 11-point analysis with a Nova 2200e instrument (Quantachrome Instruments, Boynton Beach, FL, USA) using N_2 gas adsorption (Brunauer et al., 1938). The detection limit of the instrument is 0.01 $m^2\ g^{-1}$. Samples were degassed for 3 to 4 h at 80 °C prior to the measurements.

Size distribution measurements

Electrical mobility distributions of CFA aerosol from wet particle generation were measured with a TROPOS-built differential mobility particle sizer (DMPS). Briefly, the voltage for a mobility bin is set at the DMA and the particle number concentration for this bin is measured at the CPC after a certain waiting time. Step by step, the voltage is increased to obtain particle number concentrations with respect electrical mobility, i.e., electrical mobility

distributions. An inversion routine (similar to Stratmann and Wiedensohler, 1996) was used to calculate size distributions.

It is possible that during atomization of the CFA–water suspensions, droplets are created which do not contain an insoluble CFA particle but merely dissolved substances from the bulk. Residual particles from these droplets would be water-soluble and possess physicochemical properties which are not comparable to similarly sized particles from the dry CFA sample. Purely water-soluble particles would dissolve when being activated to cloud droplets in the single particle instruments and freezing would occur due to homogeneous nucleation only. This would lead to an underestimation of f_{ice}, which would depend on the relative amount of water-soluble particles. As the water-soluble particles appear as a distinct mode in the particle size distribution, it was possible to determine the the relation between water-soluble and -insoluble particles at 300 nm. In this way, the size distribution measurements of the wet-generated CFA particles were used to assess whether a correction of the LACIS and SPIN data was necessary.

Summary

Four different instruments were employed for investigation the immersion freezing behavior of CFA samples from the ESPs of four German power plants. Among them were two single particle methods (LACIS, SPIN) and two cold stage methods (LINA, WISDOM). Due to differences in droplet size and production, droplets containing varying amounts of material were investigated with these instruments. Consequently, they operated in different temperature regimes and provided information about the immersion freezing behavior in a broad temperature range. The single particle experiments were run with two different kinds of particle generation. These were dry particle generation, i.e., aerosolization of particles from dry CFA powder, and wet particle generation, i.e., atomization and drying of CFA–water suspensions. Suspensions were also used for the cold stage experiments. The variety of different particle generation and suspension preparation methods allowed for an investigation of the effect of suspension time on the immersion freezing behavior of CFA. Different analysis techniques were used to characterize the CFA samples as detailed as possible. Single particle and bulk techniques were employed to investigate particles and particle fractions that were also present in the immersion freezing experiments. The aim was the identification of physicochemical particle properties that possibly influence the immersion freezing behavior of CFA.

4 Results

In this chapter, I firstly present the results of the physicochemical sample characterization and secondly the results of the immersion freezing experiments with CFA. The latter section is divided into results for dry-generated particles obtained with LACIS and SPIN and results obtained with the suspension methods, i.e., wet particle generation with LACIS and SPIN and cold stage measurements with LINA and WISDOM.

4.1 Physicochemical sample characterization

4.1.1 Single particle methods

ALABAMA

Averaged mass spectra (see Fig. 4.1) show that components frequently occurring in natural mineral dust are also typical constituents of dry-generated submicron CFA particles. This comprises species containing Al[$^{-43}$AlO, $^{-59}$AlO$_2$, $^{+27}$Al], Ca[$^{+40}$Ca, $^{+44}$Ca, $^{+56}$CaO, $^{+104}$CaSO$_2$], K[$^{+39}$K, $^{+41}$K], Fe[$^{+54}$Fe, $^{+56}$Fe], Si[$^{-60}$SiO$_2$, $^{-76}$SiO$_3$, $^{-88}$(SiO)$_2$, $^{-103}$AlSiO$_3$, $^{-119}$AlSiO$_4$, $^{-179}$AlSi$_2$O$_6$], Na[$^{+23}$Na], and Mg[$^{+24}$Mg, $^{+25}$Mg, $^{+26}$Mg]. The investigation of relative abundances (see Fig. 4.2) shows that more than 80 % of particles from all samples contain $^{-16}$O, $^{+27}$Al, $^{+40}$Ca, $^{+44}$Ca, and $^{+56}$CaO/Fe/Si2/KOH. Furthermore, SO$_n$ and PO$_n$ are frequently found in the CFA particles. Single particle mass spectra with high signals of the (CaO)$_n$, (CaO)$_n$H, and Ca(CaO)$_n$ cluster series together with SO$_n$ are likely related to anhydrite, as suggested by Gallavardin et al. (2008).

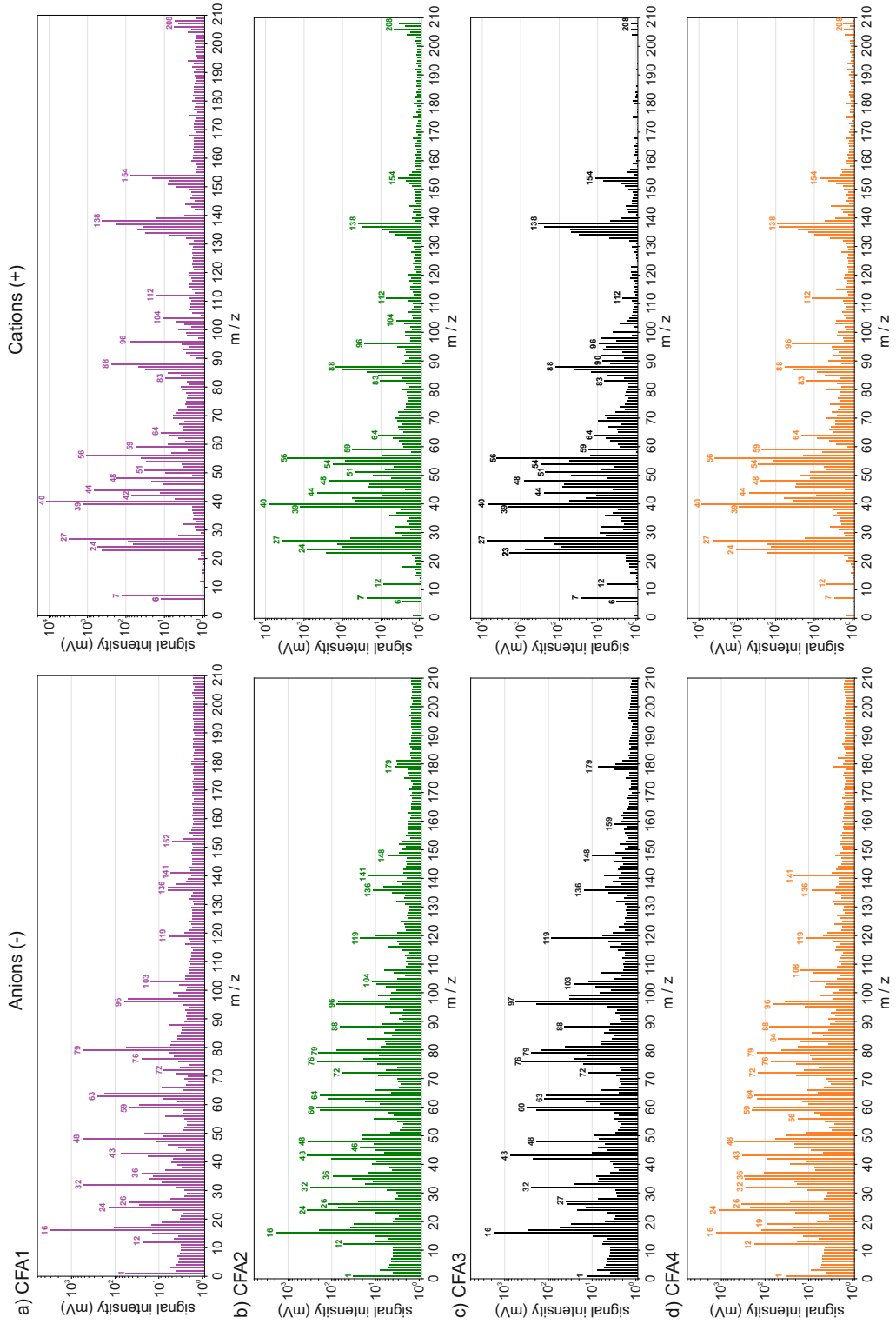

Fig. 4.1.: Averaged mass spectra of quasi-monodisperse (300 nm), dry-generated CFA particles. Common mass-to-charge ratios from left to right: [-16] O, [-32] S, [-43] AlO, [-48] SO, [-59] AlO_2, [-60] SiO_2, [-63] PO_2, [-64] SO_2, [-76] SiO_3, [-79] PO_3, [-80] SO_3, [-88] $(SiO)_2$, [-96] SO_4, [-103] $AlSiO_3$, [-119] $AlSiO_4$, [-179] $AlSi_2O_6$, [+6, +7] Li, [+23] Na, [+24, +25, +26] Mg, [+27] Al, [+39, +41] K, [+40, +44] Ca, [+46, +47, +48] Ti, [+54] Fe, [+56] CaO/Fe/Si2/KOH, [+59] Co, [+64, +68] Zn, [+86, +87, +88] Sr, [+104] SrO/$CaSO_2$, [+136, +137, +138] Ba, [+154] BaO, [+206, +207, +208] Pb.

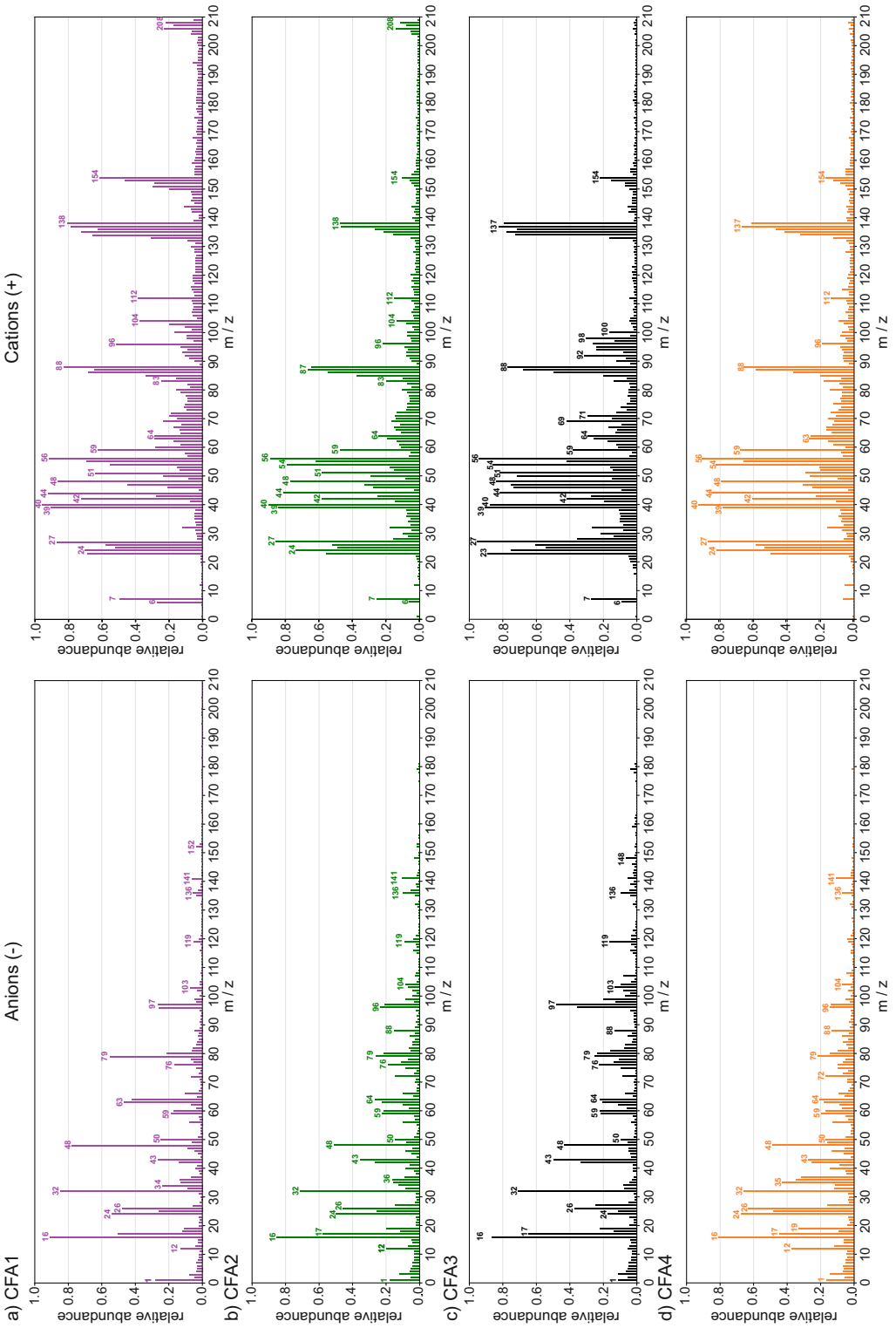

Fig. 4.2.: Relative abundance of species in quasi-monodisperse (300 nm), dry-generated CFA particles. Background signals were determined and used as a threshold to decide whether a particle contained/did not contain a certain species. Common mass-to-charge ratios from left to right: [-16] O, [-32] S, [-43] AlO, [-48] SO, [-59] AlO_2, [-60] SiO_2, [-63] PO_2, [-64] SO_2, [-76] SiO_3, [-79] PO_3, [-80] SO_3, [-88] $(SiO)_2$, [-96] SO_4, [-103] $AlSiO_3$, [-119] $AlSiO_4$, [+6, +7] Li, [+23] Na, [+24, +25, +26] Mg, [+27] Al, [+39] K, [+40, +42, +44] Ca, [+46, +47, +48] Ti, [+54] Fe, [+56] CaO/Fe/Si2/KOH, [+59] Co, [+64] Zn, [+86, +87, +88] Sr, [+104] SrO/$CaSO_2$, [+136, +137, +138] Ba, [+154] BaO, [+206, +207, +208] Pb.

It has been reported that especially submicron CFA particles often show an enrichment in trace elements (Davison et al., 1974; Kaakinen et al., 1975; Block and Dams, 1976; Gladney et al., 1976; Tan et al., 2002). This is also true for the here investigated samples as Li[$^{+6}$Li, $^{+7}$Li], Ti[$^{+46}$Ti, $^{+47}$Ti, $^{+48}$Ti], Co[$^{+59}$Co], Zn[$^{+64}$Zn, $^{+66}$Zn, $^{+68}$Zn], Sr[$^{+86}$Sr, $^{+87}$Sr, $^{+88}$Sr, $^{+104}$SrO], Ba[$^{+136}$Ba, $^{+137}$Ba, $^{+138}$Ba, $^{+154}$BaO], and Pb[$^{+206}$Pb, $^{+207}$Pb, $^{+208}$Pb] were detected. At least 50 % of the dry-generated CFA particles contained $^{+48}$Ti, $^{+88}$Sr and $^{+138}$Ba, making them potential markers for the detection of atmospheric CFA particles. However, there is the caveat that these elements are components of some mineral dust types such as illite, too (Gallavardin et al., 2008). Pb[$^{+206}$Pb, $^{+207}$Pb, $^{+208}$Pb] is present in ∼20 % of CFA1 particles and ∼10 % of CFA2 particles. In CFA3 and CFA4 almost no particles contained Pb signals above the threshold, and hence it cannot be used as a marker for CFA.

In order to find a systematic difference in the chemical composition of dry- and wet-generated CFA particles, the signal ratio wet/dry was determined (see Fig. 4.3). In the following, I only focus on features that are characteristic of all CFA samples. A significant enhancement of signal intensity up to several hundreds of percent can be seen for mass-to-charge ratios [+57, +113], hinting at the hydration of CaO. To explain the observed changes in signal intensity, I suggest the below described reactions (4.1), (4.2), (4.5), and (4.6), where reactions (4.1) and (4.2) represent the hydration reactions, and reactions (4.5) and (4.6) a possible molecular fragmentation after vaporization and ionization in ALABAMA. An increase was also found for mass-to-charge ratios [+105, +155], indicating the hydration of SrO and BaO (see reactions (4.3), (4.4), (4.7), and (4.8)). Furthermore, a decrease of S-containing substances was registered. $^{-32}$S, $^{-48}$SO, $^{-64}SO_2$, $^{-80}SO_3$, $^{-81}HSO_3$, $^{-96}SO_4$, and $^{-97}HSO_4$ all appear to be reduced in wet-generated particles, which could be an indication for S being dissolved from the 300 nm particles.

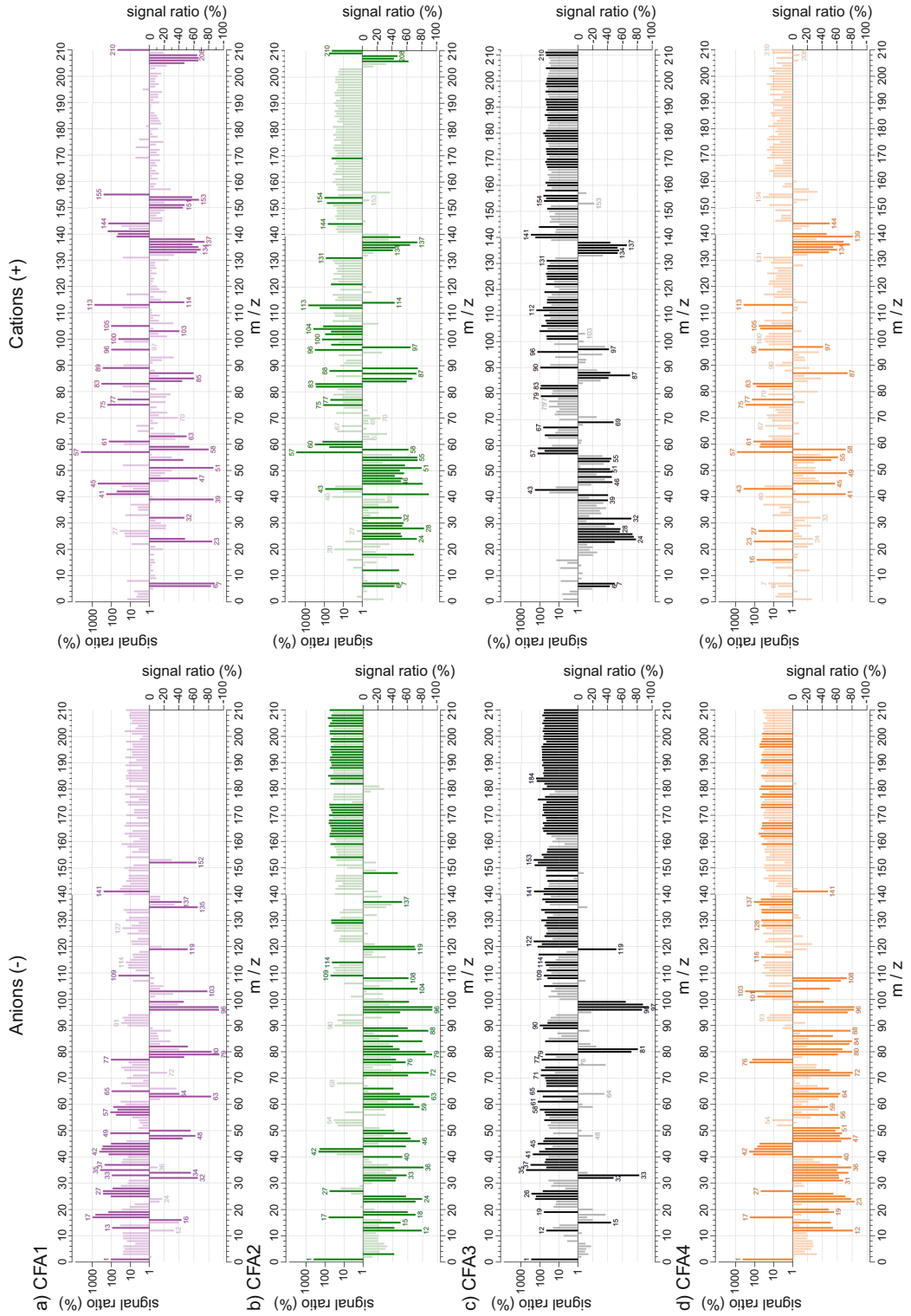

Fig. 4.3.: Signal ratio of quasi-monodisperse (300 nm) wet- vs. dry-generated CFA particles. Positive (negative) bars represent an increase (a decrease) in signal intensity for wet-generated particles in comparison to dry-generated particles. Stronger colors indicate species for which the signal intensity has changed by more than 40 %. Common mass-to-charge ratios from left to right: [-32] S, [-48] SO, [-64] SO_2, [-80] SO_3, [-81] HSO_3, [-96] SO_4, [-97] HSO_4, [+57] CaOH, [+105] SrOH, [+113] Ca_2O_2H, [+155] BaOH.

$$^{56}\mathrm{CaO} + ^{18}\mathrm{H_2O} \rightarrow \quad ^{74}\mathrm{Ca(OH)_2} \tag{4.1}$$

$$^{96}\mathrm{Ca_2O} + ^{18}\mathrm{H_2O} \rightarrow \quad ^{114}\mathrm{Ca_2(OH)_2} \tag{4.2}$$

$$^{104}\mathrm{SrO} + ^{18}\mathrm{H_2O} \rightarrow \quad ^{122}\mathrm{Sr(OH)_2} \tag{4.3}$$

$$^{154}\mathrm{BaO} + ^{18}\mathrm{H_2O} \rightarrow \quad ^{172}\mathrm{Ba(OH)_2} \tag{4.4}$$

$$^{74}\mathrm{Ca(OH)_2} \rightarrow ^{+57}\mathrm{CaOH} \quad + ^{-17}\mathrm{OH} \tag{4.5}$$

$$^{114}\mathrm{Ca_2(OH)_2} \rightarrow ^{+113}\mathrm{Ca_2O_2H} \quad + ^{-1}\mathrm{H} \tag{4.6}$$

$$^{122}\mathrm{Sr(OH)_2} \rightarrow ^{+105}\mathrm{SrOH} \quad + ^{-17}\mathrm{OH} \tag{4.7}$$

$$^{172}\mathrm{Ba(OH)_2} \rightarrow ^{+155}\mathrm{BaOH} \quad + ^{-17}\mathrm{OH} \tag{4.8}$$

ESEM/EDX

Figure 4.4 shows the ESEM images of dry- and wet-generated quasimonodisperse CFA particles. Spherical particles, often described as the main particle type in CFA in the literature (e.g., Davison et al., 1974; Ramsden and Shibaoka, 1982; Flanders, 1999; Zhang et al., 2011), were rarely detected in the dry-generated samples. Spherical shapes are thought to originate from combustion of organic substances and melting of mineral inclusions in the coal, leading to the formation of spherical ash droplets (see Sec. 2.2.1). The spherical shape is often retained as the particles cool and solidify, however, particles can also be deformed. Seames (2003) reported CFA particles in the size range between 0.1 and 1 μm with irregular shapes, comparable to the morphology shown in Fig. 4.4 and argued that this deviation from the sphere could be the result of particle inflation, cracking, or shedding due to expanding gases, partial melting, and/or agglomeration. The latter is a probable mechanism in the case of CFA1, where many particles consisting of aggregates of small spherules were found. Gieré et al. (2003) who performed transmission electron microscopy of class F CFA particles found both smooth spherical particles and irregularly shaped particles in the size range of several hundred nanometers. The irregularly shaped particles were made up of crushed glass, or glassy spheres with small crystals attached to their surface which concealed the spherical shape. Differences in the morphology of the CFA samples can be explained by differences in the coal composition and combustion conditions (Zhang et al., 2006).

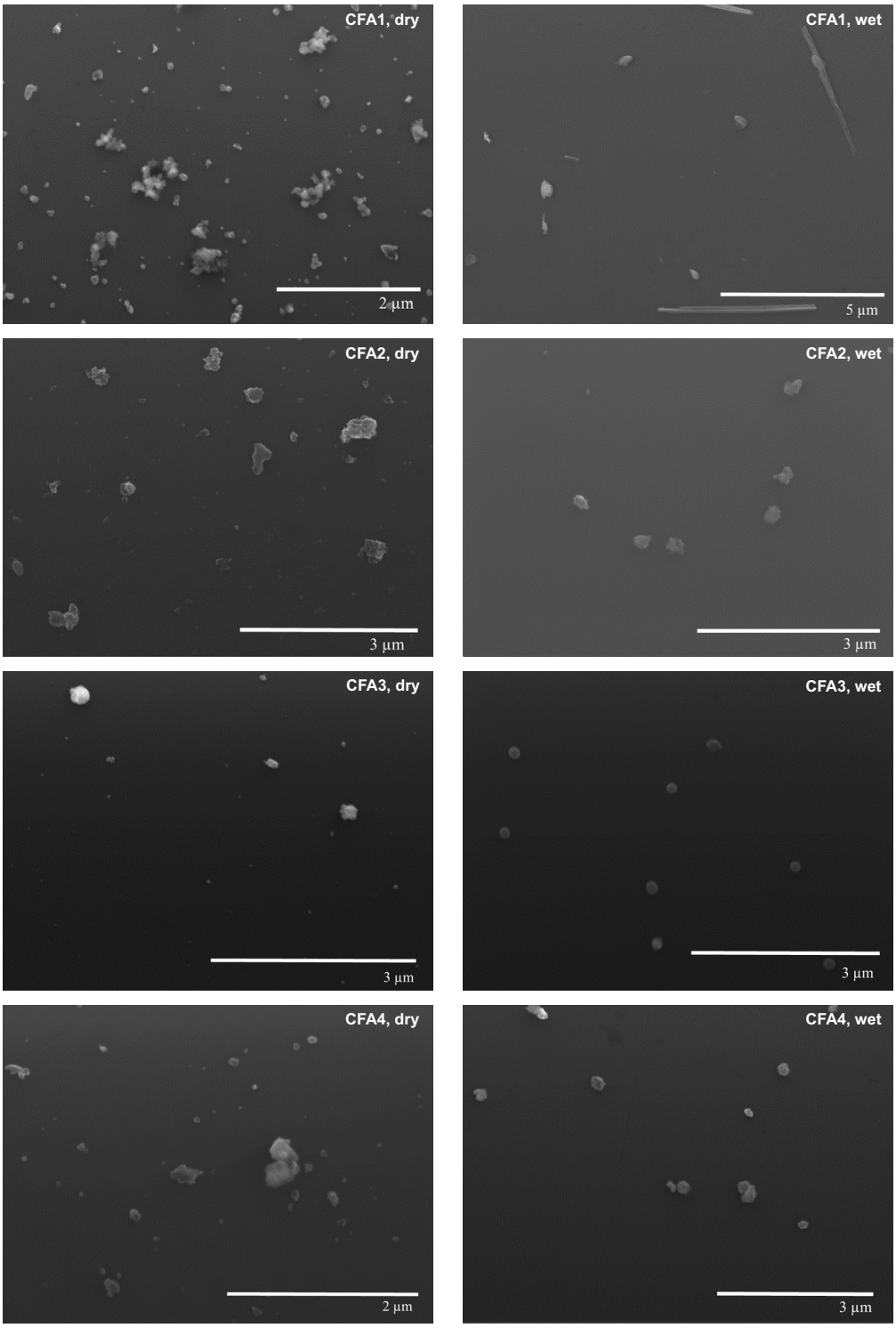

Fig. 4.4.: ESEM images of quasi-monodisperse (300 nm) CFA particles sampled onto B substrates with the Multi-MINI. Left: Dry particle generation, right: wet particle generation. Note the different magnification.

In general, the wet-generated CFA particles feature a more uniform and compact shape than the dry-generated ones, maybe because irregularities are covered by a layer of dissolved and redistributed material during suspension and subsequent atomization (Herich et al., 2009). An exception are wet-generated CFA1 particles, which, in addition to spheroidal particles, occur as needle-shaped particles (also see Fig. 4.5). The needle-shaped particles are possibly related to the high Ca content of this sample (see bulk chemical composition, Sec. 4.1.2) and composed of calcite ($CaCO_3$). Calcite can be found in CFA1 after the sample has been in contact with water (see XRD results, Sec. 4.1.2) and is known to form needle-shaped particles under certain conditions (Kim et al., 2009). Even though the substrates were loaded after size selection, needle-shaped particles which are much longer than the selected 300 nm can be seen on the ESEM images and could be introduced into LACIS. In the course of the experiments, it turned out that the occurrence of needle-shaped particles indeed biased the LACIS measurements with CFA1 presented in Grawe et al. (2016). Please refer to Appendix C for a detailed explanation of the issue and handling of biased data.

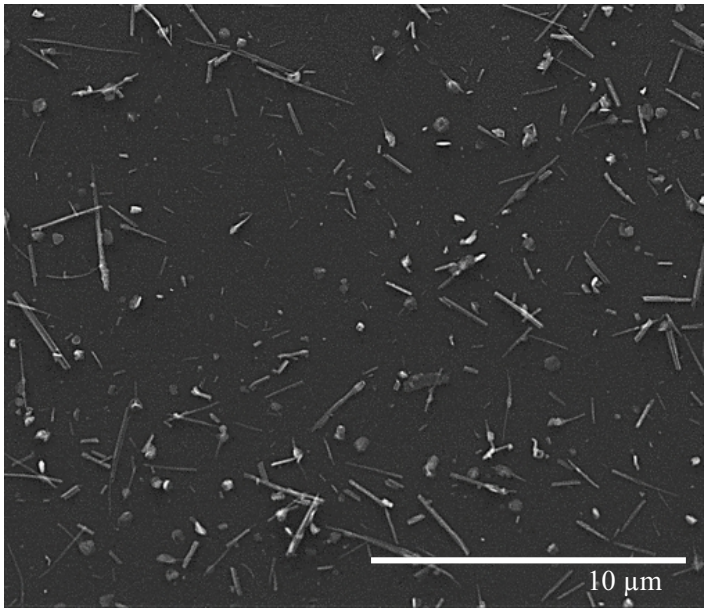

Fig. 4.5.: ESEM image of quasi-monodisperse (300 nm) CFA1 particles from wet particle generation.

A positive side note concerning the needle-shaped particles is their potential application as non-spherical reference particles for the calibration of optical particle counters. In cooperation with the Institute for Atmospheric and Climate Science at the Eidgenössische Technische Hochschule Zürich,

particles from the CFA1 suspension have successfully been used for characterization measurements with the newly developed High-Speed Particle Phase Discriminator (see conference abstract by Mahrt et al., 2018a).

Table 4.1.: Chemical composition of CFA particles from dry and wet particle generation as determined by EDX measurements. The number of investigated particles is given in parentheses. Elements in parentheses have only been detected in some of the particles.

CFA sample	Dry particle generation	Wet particle generation	Difference wet/dry
1	O, Ca, Si, S (16)	O, Ca, Al, (Fe, Si) (15)	– S
	Si, O (10)	O, Al, (Fe, Si) (12)	+ Fe, Al
2	O, Fe, Al, Si, S, Ca (9)	O, Ca, Al, Si, S (16)	– Mg
	O, Fe, Al, Si, S, Ca, Mg (7)	O, Ca, Al, Si, S, Fe (3)	
	O, Si, Ca, Fe (1)	O, Si, Ca (1)	
3	Si, O, Al, Fe, Ca, (Mg, S) (9)	Si, O, Al, Fe, Ca, (Mg, S, K) (5)	
	Si, O (3)	Si, O, (Al, Fe) (19)	
	O, S, (Al, Fe, Si) (3)	O, Ca, Si, S, (Fe, Mg) (3)	
	O, Ca, Si (1)		
	O, Ca (1)		
4	Si, O (5)	Si, O (11)	– C
	O, C, Si, Ca, Al, (Fe, S, Mg) (11)	O, Ca, Si, Al, S, (Fe) (8)	
	Si, O, Al (5)	O, Si, (Al, Fe) (2)	
	C, O (2)		

The results of the EDX chemical composition analysis are summarized in Table 4.1. EDX was performed for both dry- and wet-generated particles of each sample. Elements that were detected in all samples, either from dry or wet particle generation are O, Ca, and Si, which is in agreement with the ALABAMA mass spectra. For the most part, the identified differences between dry- and wet-generated particles agree with the mass spectra, too. However, characteristic trace elements (Ti, Co, V, Ba, Sr, Zn, and Pb), that are present in the CFA samples according to the mass spectra, were not detected by the EDX analysis. This is probably related to measurement statistics. Due to the time-consuming analysis and the, in parts, non-ideal loading of the substrates, $\sim$20 particles were characterized in each case. Hence, a more detailed comparison of EDX results of different samples and particle generation methods, and to the mass spectra cannot be provided.

Light microscopy

Figure 4.6 shows optical microscope images of liquid CFA suspension droplets. It can be seen that the needle-shaped particles are present in the aqueous environment of the CFA1 suspension, i.e., are formed in the suspension as a precipitate (see Fig. 4.6 a). This observation disproves the previous assumption of water-soluble needle-shaped particles that form in the course of drying of the suspension droplets (Grawe et al., 2016). According to the new findings, the needle-shaped particles are not or only weakly water-soluble, which is the case for calcite (Plummer and Busenberg, 1982), too. The needle-shaped particles in the CFA1 suspension are several tens of microns long. Droplets from the CFA2, CFA3, and CFA4 suspensions do not contain needle-shaped particles in the resolved size range, only irregular and spherical particles. Generally, the number of irregularly shaped particles is higher than the number of spherical particles for all samples. Coagulation of particles can be observed to some extent for all samples and might affect the surface area available for triggering immersion freezing in the cold stage experiments as described by Emersic et al. (2015).

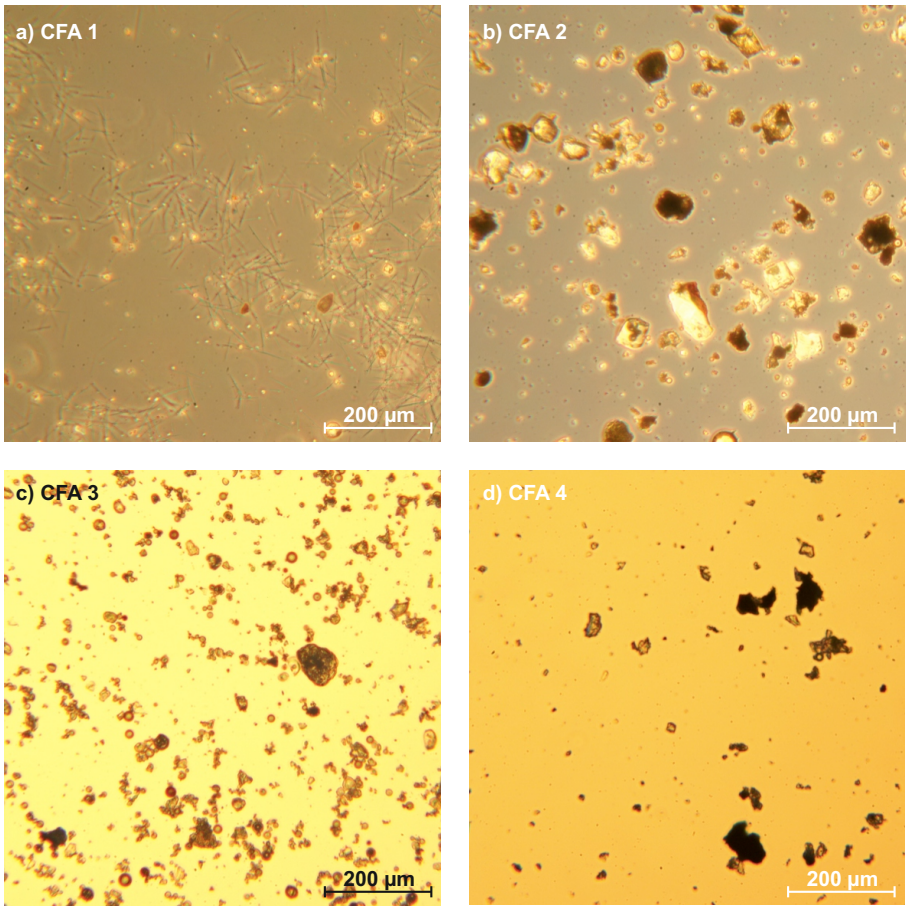

Fig. 4.6.: Optical microscope images of CFA suspension droplets. a) CFA1, where needle-shaped particles are present in the aqueous environment. b), c), and d) CFA2, CFA3, and CFA4, where no needle-shaped particles were observed.

4.1.2 Bulk methods

XRD

XRD patterns (see Fig. 4.7 to 4.10) were measured with the original samples and the samples after suspension in water which then was evaporated. This was done to identify both major crystalline phases and processes taking place during the interaction of CFA with water. Note that this is a bulk investigation, i.e., a direct connection may not be drawn between the XRD and the LACIS, SPIN, ALABAMA, and EDX results. Amounts of the identified phases are given in each plot but must be treated cautiously, as the CFA powder is quite inhomogeneous and only ∼0.5 g were used for an XRD measurement. Table 4.2 gives an overview of phases identified in the CFA samples.

Quartz is the major crystalline phase in all of the samples, either dry or after suspension. Anhydrite and quicklime occur in all of the dry samples, however, prominent peaks can only be seen for CFA1 (see Fig. 4.7). Minor crystalline phases in the dry samples include mullite, hematite, gehlenite ($Ca_2Al[AlSiO_7]$), magnetite ($Fe^{2+}/Fe_2^{3+}O_4$), periclase (MgO), rutile (r–TiO_2), anatase (a–TiO_2), and tricalcium-aluminate ($3CaO{\cdot}Al_2O_3$), all of which have been identified previously in CFA samples of different geographical origin (e.g., McCarthy et al., 1984; Querol et al., 1996; Nathan et al., 1999; Shoumkova et al., 2005; Ward and French, 2006; Liang et al., 2010; Nyambura et al., 2011).

Distinct changes in the XRD pattern of dry particles and particles that have been suspended in water can be seen for CFA1 (see Fig. 4.7). Here, the hydration of anhydrite to gypsum (see reaction (4.9)) can be observed. This is a process which is also relevant for submicron CFA particles, as those are likely to be coated with anhydrite (Enders, 1996). Furthermore, the pattern indicates that quicklime is converted into calcite via hydration and carbonation (see reactions (4.10) and (4.11)). Only minor changes between the dry bulk and the bulk after suspension can be seen for the other CFA samples, probably because they contain much less anhydrite and quicklime than CFA1 (see bulk chemical composition, Sec. 4.1.2). The difference in the bulk concentration of quicklime between CFA1 and the other samples is potentially mirrored by the registered difference in the pH values of the CFA suspensions. The CFA2, CFA3, and CFA4 suspensions are neutral to slightly alkaline (pH$\sim$7 to 8). The CFA1 suspension is strongly alkaline (pH$\sim$11), likely due to the formation of portlandite (see reaction (4.10)) which dissociates into Ca^{2+} and OH^- ions. The decrease of the magnetite fraction in suspension particles of CFA2 and CFA3 in comparison to the dry bulk (see Fig. 4.8 and 4.9) could be due to the suspension preparation routine. Ferromagnetic magnetite particles tend to stick to the magnetic agitator while stirring. When removing the agitator from the suspension, these particles are depleted.

$$CaSO_4(s) + 2H_2O(l) \rightarrow CaSO_4 \cdot 2H_2O(s) \tag{4.9}$$

$$CaO(s) + H_2O(l) \rightarrow Ca(OH)_2(s) \tag{4.10}$$

$$Ca(OH)_2(s) + CO_2(aq) \rightarrow CaCO_3(s) + H_2O(l) \tag{4.11}$$

Table 4.2.: Identified crystalline phases from XRD measurements of dry CFA and CFA after suspension and evaporation. Checkmarks in parentheses indicate minor phases (< 5 %).

		CFA1		CFA2		CFA3		CFA4	
Crystalline phase	Chemical formula	dry	wet	dry	wet	dry	wet	dry	wet
Quartz	SiO_2	✓	✓	✓	✓	✓	✓	✓	✓
Anhydrite	$CaSO_4$	✓	–	(✓)	–	(✓)	–	(✓)	–
Gypsum	$CaSO_4{\cdot}2H_2O$	–	✓	–	(✓)	–	(✓)	–	–
Quicklime	CaO	✓	–	(✓)	–	(✓)	–	(✓)	–
Calcite	$CaCO_3$	–	✓	–	–	–	(✓)	–	–
Portlandite	$Ca(OH)_2$	–	–	–	✓	–	–	–	–
Barytocalcite	$BaCa(Ca_3)_2$	–	✓	–	–	–	–	–	–
Mullite	$Al_6Si_2O_{13}$	✓	✓	✓	(✓)	✓	✓	–	–
Gehlenite	$Ca_2Al[AlSiO_7]$	✓	✓	–	–	–	–	–	(✓)
Hematite	Fe_2O_3	(✓)	–	(✓)	(✓)	(✓)	(✓)	(✓)	–
Magnetite	$Fe^{2+}/Fe^{3+}O_4$	–	–	(✓)	(✓)	(✓)	–	–	–
Periclase	MgO	(✓)	(✓)	(✓)	(✓)	–	–	–	–
Rutile	r–TiO_2	–	–	(✓)	(✓)	–	–	–	(✓)
Anatase	a–TiO_2	–	–	–	–	(✓)	(✓)	–	–
Tricalcium-aluminate	$3CaO{\cdot}Al_2O_3$	✓	(✓)	–	–	–	–	–	–

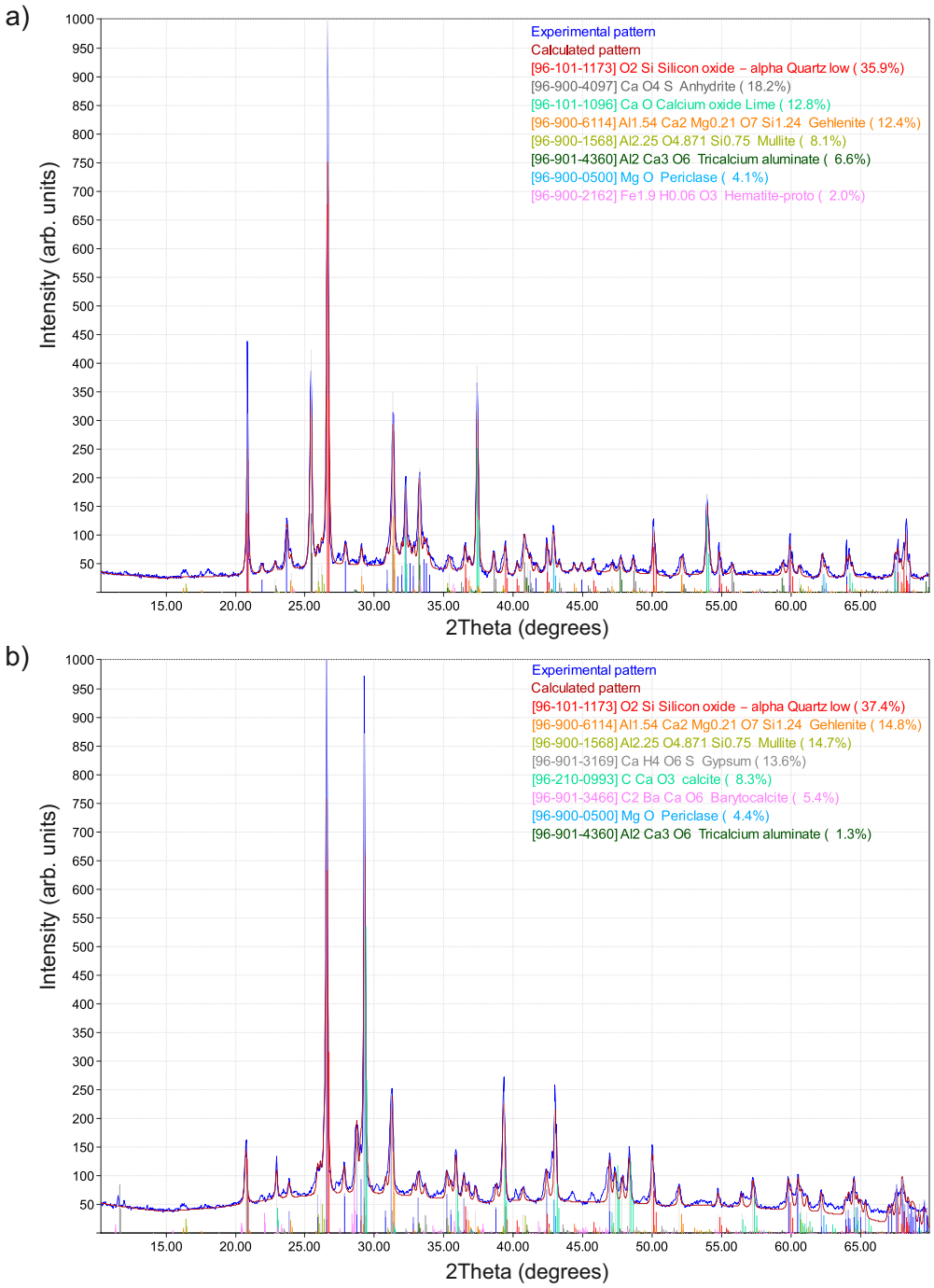

Fig. 4.7.: XRD patterns of a) dry CFA1 and b) CFA1 after suspension and evaporation. Numbers in brackets in the legend indicate reference pattern IDs from the Crystallography Open Database. Numbers in parentheses indicate the identified amount of the crystalline phase but should be treated cautiously.

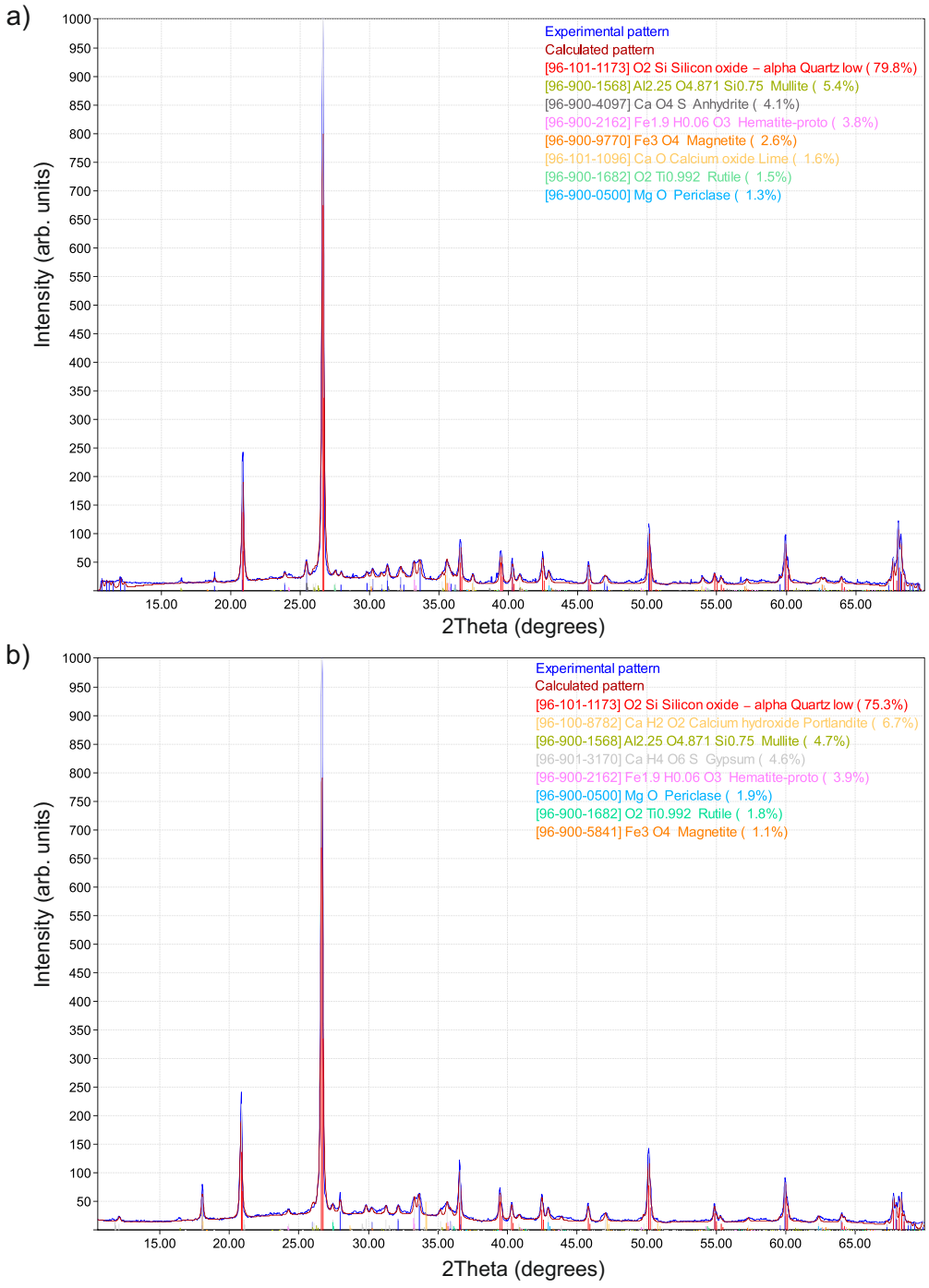

Fig. 4.8.: XRD patterns of a) dry CFA2 and b) CFA2 after suspension and evaporation. Numbers in brackets in the legend indicate reference pattern IDs from the Crystallography Open Database. Numbers in parentheses indicate the identified amount of the crystalline phase but should be treated cautiously.

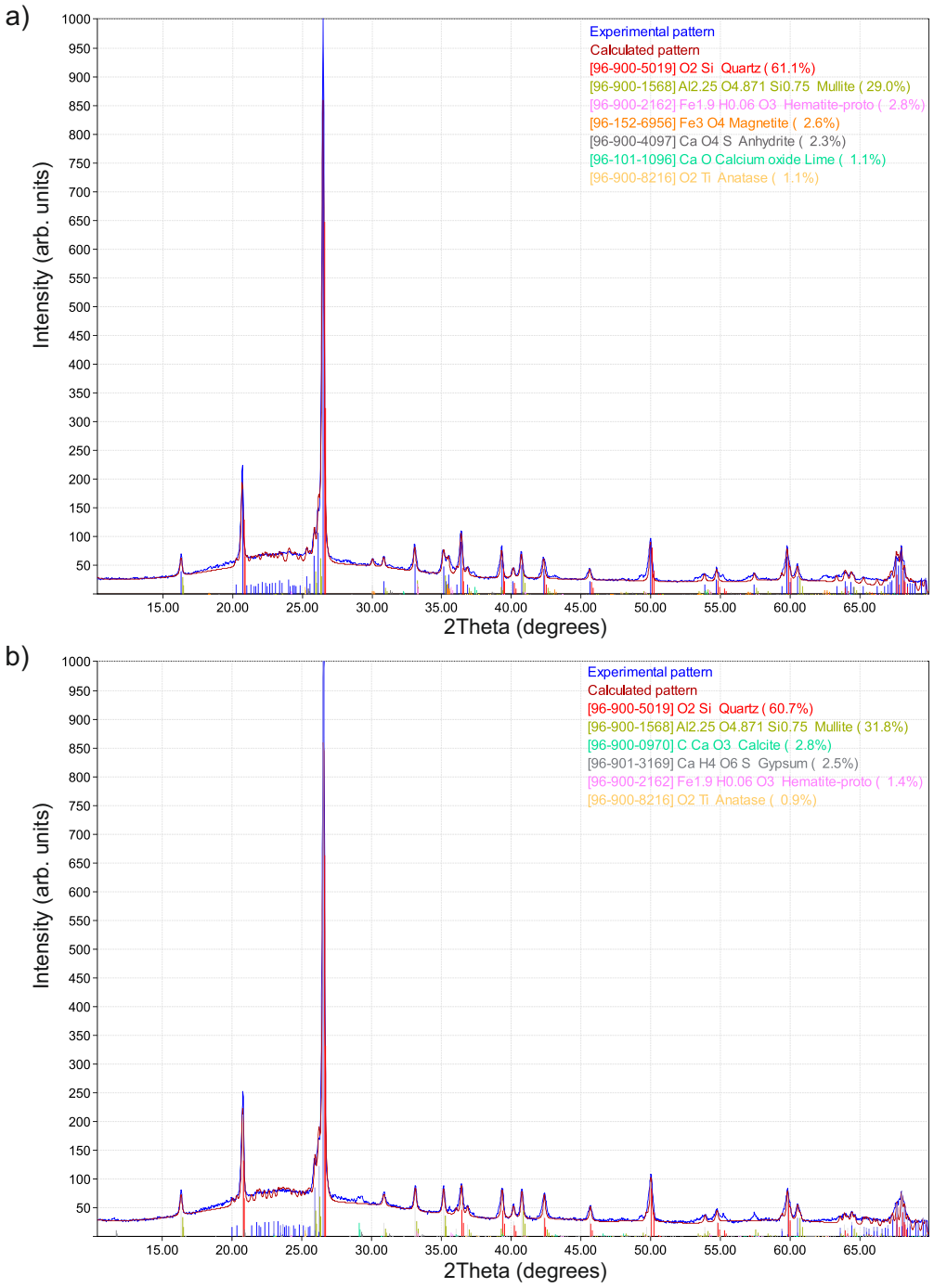

Fig. 4.9.: XRD patterns of a) dry CFA3 and b) CFA3 after suspension and evaporation. Numbers in brackets in the legend indicate reference pattern IDs from the Crystallography Open Database. Numbers in parentheses indicate the identified amount of the crystalline phase but should be treated cautiously.

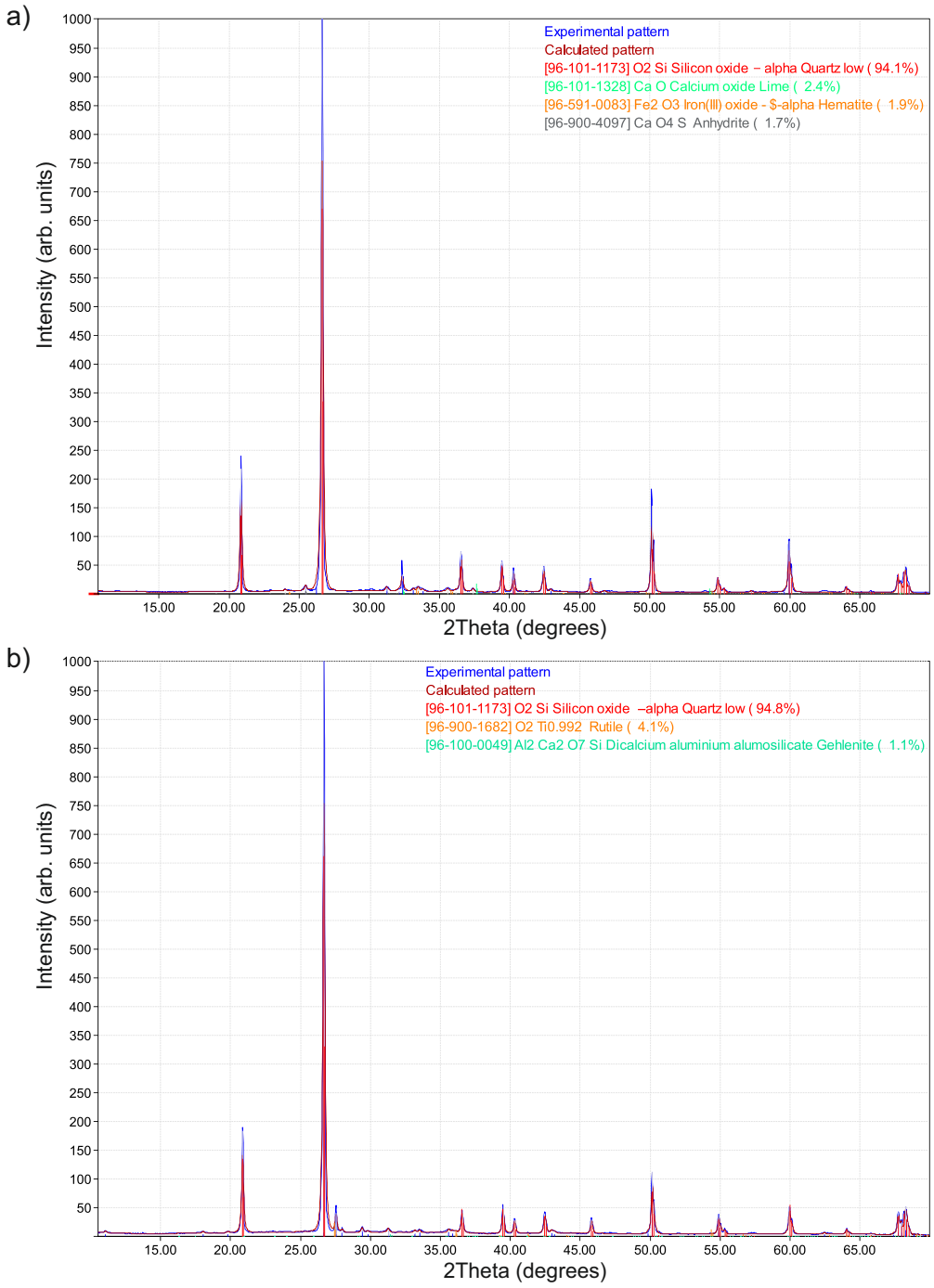

Fig. 4.10.: XRD patterns of a) dry CFA4 and b) CFA4 after suspension and evaporation. Numbers in brackets in the legend indicate reference pattern IDs from the Crystallography Open Database. Numbers in parentheses indicate the identified amount of the crystalline phase but should be treated cautiously.

It has been argued previously that the amorphous, i.e., non-crystalline, fraction may play an important role for the immersion freezing behavior of CFA particles (Umo et al., 2015). Even though the amorphous fraction was not quantitatively determined here, the broad "hump", which occurs in the region up to $\sim 40^{\circ}$ and is most prominent in the CFA3 pattern (see Fig. 4.9), indicates that this sample contains the highest amount of amorphous material in the bulk. This is in accordance with findings by Ward and French (2006) who investigated the amorphous fraction of different CFA samples and showed that CFA from black coal combustion contains more amorphous material than CFA from brown coal combustion.

Bulk chemical composition

Due to the size-dependent physicochemical particle properties of CFA, the bulk chemical composition is of limited value for identifying species influencing the immersion freezing behavior of 300 nm particles. However, the results of the ICP-SFMS measurements (see Fig. 4.11) can be used for interpretation of the cold stage measurements and to classify the CFA samples according to the ASTM standard C618 (see Sec. 2.2.1). The combined contents of SiO_2, Al_2O_3, and Fe_2O_3 of CFA1, CFA2, CFA3, and CFA4 are 51 ± 8, 84 ± 13, 85 ± 14, and 67 ± 10 wt%, respectively. The CaO contents of CFA1, CFA2, CFA3, and CFA4 are 26 ± 4, 12 ± 2, 2 ± 0.4, and 6 ± 1 wt%, respectively. Consequently, CFA1 is of class C and CFA2, CFA3, and CFA4 are of class F, within measurement uncertainty. Concerning elements other than Si, Al, Fe, and Ca, CFA1 contains $\sim$factor 4 more S than the other samples. CFA3 is the sample with the highest concentrations of many of the investigated trace elements, i.e., As, Be, Cd, Co, Cr, Mo, Ni, Sc, V, and Y, potentially because these elements are enriched in the black coal compared to the brown coals combusted in the power plants. The LOI values of the four CFA samples are -0.8 ± 5 % for CFA1, 0.2 ± 5 % for CFA2, 0.8 ± 5 % for CFA3, and 8.1 ± 5 % for CFA4, i.e., apparently only CFA4 still contains a relevant amount of unburnt fuel after combustion in the power plant. This is in line with the visual impression from photographs of the samples (see Fig. 3.1) where most charred particles can be seen for CFA4.

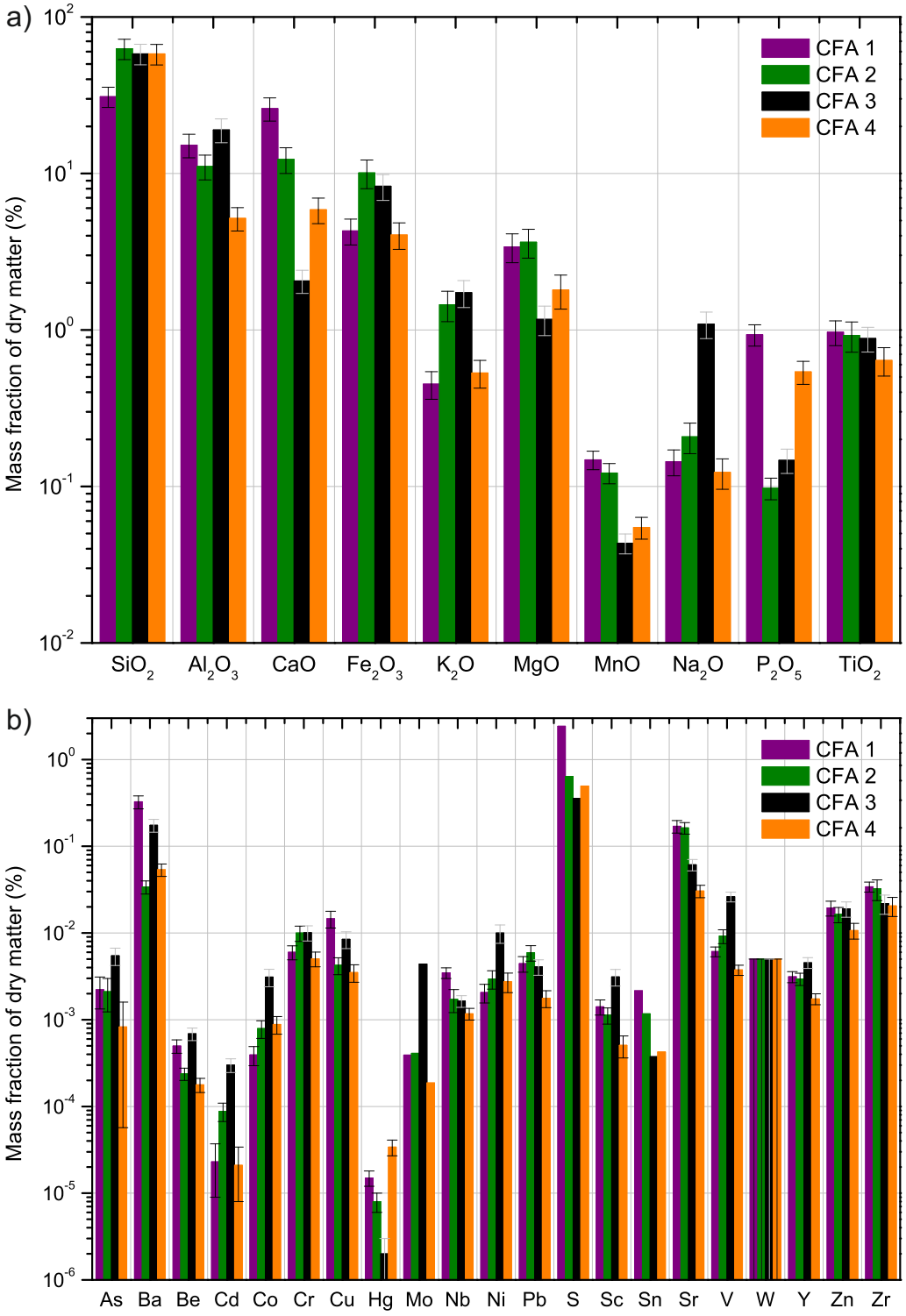

Fig. 4.11.: Mass fractions of a) major oxides (calculated from elemental mass fractions) and b) minor elements in dry bulk CFA.

BET

The results shown in Table 4.3 are average values of fits ($R^2 = 0.999$) to three BET measurements with each sample. The given errors correspond to the standard deviation of the three results of each sample. Measurements with CFA1, CFA2, and CFA3 yielded results which are quite close to the detection limit. Independent measurements with bulk CFA at a different laboratory showed very similar results (CFA1: 1.7 $m^2\ g^{-1}$, CFA2: 4 $m^2\ g^{-1}$, CFA3: 1 $m^2\ g^{-1}$, CFA4: 52 $m^2\ g^{-1}$), indicating that the low values given in Table 4.3 are trustworthy. Determination of the pore volume fraction showed that CFA1, CFA2, and CFA3 are non-porous, CFA4 has low porosity. The significantly higher surface area of CFA4 might be related to the occurrence of unburnt material in this sample. Hiranuma et al. (2008) showed that particles with high C content tend to form irregular structures because of enhanced aggregation.

Table 4.3.: BET specific surface area of bulk (used for LINA n_s calculations) and fine CFA (used for WISDOM n_s calculations).

CFA sample	BET specific surface area ($m^2\ g^{-1}$)
1 bulk	1.4 ± 0.3
1 fine	1.2 ± 0.2
2 bulk	5.9 ± 0.6
3 bulk	1.5 ± 0.3
4 bulk	49.4 ± 0.7

Summary

According to the single particle techniques, i.e., ALABAMA and EDX, dry-generated 300 nm particles contain elements that are characteristic of mineral dust. Trace elements like Sr, Ti, and Ba were found in the mass spectra of more than half of the investigated particles and can potentially be used to identify CFA particles in the atmosphere, together with the overall fingerprint of the mass spectra. However, it is not possible to provide provide unambiguous markers because of the heterogeneous nature of CFA and the fact that the aforementioned trace elements can sometimes be found in mineral dust, too. The most important finding from the microscopic images is that super-micron needle-shaped particles form in the CFA1 suspension and probably enter the single particle immersion freezing instruments. The bulk chemical

composition analysis shows that CFA1 contains most CaO and S. This is in line with the XRD measurements, where anhydrite and quicklime peaks were most prominent in the CFA1 pattern. Both anhydrite and quicklime are hydrated (quicklime also carbonated) in contact with water to form gypsum and calcite in CFA1. There is no clear evidence for hydration taking place in the suspensions of the other samples, too, because the concentrations of anhydrite and quicklime are too low to cause unambiguous peaks in the XRD patterns. However, comparing mass spectra of dry- and wet-generated 300 nm particles indicates hydration for all samples, i.e., gypsum and calcite are likely formed in CFA2, CFA3, and CFA4 as well. BET values are very low, except for CFA4. This could be related to the comparably large LOI value of CFA4 which indicates the presence of carbonaceous, potentially aggregated particles.

4.1.3 Size distribution measurements

Figure 4.12 shows size distributions of the wet-generated CFA particles. Even though they appear to be tri-modal, a bi-modal normal distribution fit was applied, because only part of the third mode was captured. Table 4.4 shows the mean values μ of both normal distribution modes for each sample. The fitting was performed to identify the size range of the different occurring modes. In contrast to earlier publications (Flagan and Friedlander, 1978; Damle et al., 1982), where CFA size distributions were characterized as bi-modal with the first submicron mode representing particles formed from the gas phase by nucleation/condensation and the second supermicron mode representing residual ash particles, Linak et al. (2002) describe a tri-modal size distribution with an additional mode enclosed between nucleation/condensation mode and residual ash mode. The irregularly shaped 300 nm particles that can be seen on the ESEM images (see Fig. 4.4) point towards the presence of such a “fine fragmentation” mode, which could be equal to mode 2 in the shown CFA size distributions. Mode 1 at smaller sizes originates from water-soluble substances in the suspension and apparently conceals the nucleation/condensation mode particles.

In case of CFA2, CFA3, and CFA4, suspensions were prepared in the same way as for LACIS measurements, i.e., by suspending 0.5 g CFA in 100 mL distilled water, 10 min of ultrasonification, and 24 h of stirring. For these samples, the ratio of concentrations of the two modes clearly shows that 300 nm particles

almost exclusively consist of water-insoluble material. Mode 1, i.e., water-soluble material, does not contribute to the measured number concentrations of CFA2, CFA3, and CFA4 at 300 nm, meaning that no correction of f_{ice} is needed.

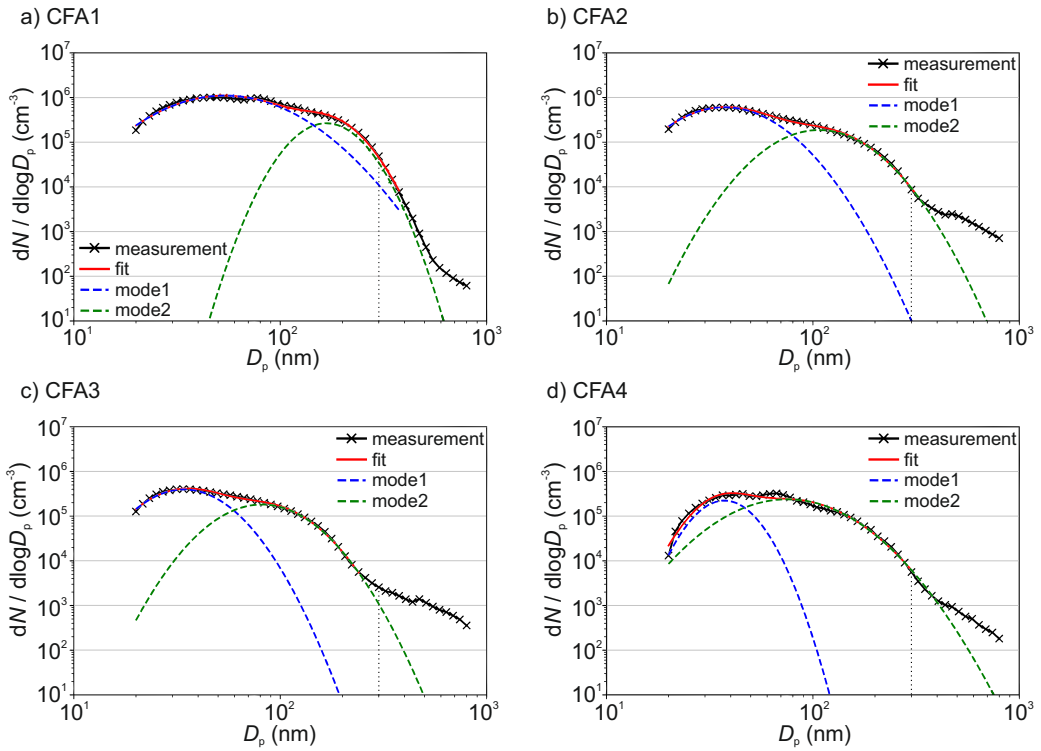

Fig. 4.12.: Size distributions from DMPS measurements with wet-generated CFA particles. a) Size distribution of particles generated from a freshly prepared CFA1 suspension. b), c), and d) Size distributions of aerosol generated from suspensions of CFA2, CFA3, and CFA4 that were ultrasonicated for 10 min and stirred for 24 h. The vertical dotted lines mark a particle size of 300 nm.

Table 4.4.: Mean values μ of the bi-modal normal distribution fits to size distributions of wet-generated CFA particles.

Sample	Mode	μ (nm)
CFA1	1	53.95
	2	167.34
CFA2	1	37.34
	2	107.19
CFA3	1	34.23
	2	81.66
CFA4	1	37.28
	2	75.21

In case of CFA1, a fresh suspension was prepared to minimize the occurrence of needle-shaped particles which would bias the size distribution measurement. However, I suspect that needle-shaped particles already started forming during the size distribution measurement, which takes ∼15 min. In fact, I observed the formation of needle-shaped particles in a fresh CFA1 suspension droplet within ∼10 min under the optical microscope. This would also explain, why the size distribution of CFA1 differs from those of the other samples. The mean of mode 1 is at ∼54 nm for CFA1, whereas it is close to 35 nm for the other three CFA samples. Also, mode 1 is much broader for CFA1 in comparison to the other samples. This suggests that I measured the size distribution of an external mixture of needle-shaped particles and spheroidal particles which cannot be separated from each other. Hence, no direct conclusion about the occurrence of purely water-soluble 300 nm particles can be drawn for CFA1, but judging from the results of the other three CFA samples, their amount is likely small compared to the amount of insoluble particles.

4.2 Immersion freezing behavior of CFA

4.2.1 Dry particle generation

LACIS

LACIS measurements with dry-generated CFA particles were performed between −27 °C, where the first signal above the limit of detection could be observed, and −37 °C, where homogeneous ice nucleation started to contribute. Data showing measurements with dry-generated particles from CFA1 are taken from Grawe et al. (2016). Comparing the n_s spectra of all four CFA samples (see Fig. 4.13) shows variation within a factor of 37 (difference between CFA2 and CFA3 at −28 °C). CFA1 has the highest n_s, followed by CFA2, CFA4, and CFA3. This order is valid throughout the whole examined temperature range, except for $T > -29$ °C, where n_s decreases rapidly in case of CFA1. The curve shape for $T < -29$ °C with the relatively shallow increase is comparable for all samples. The broad temperature range, in which the increase in n_s is observed, hints at a variety of ice nucleation active sites with different contact angles at the surface of the CFA particles. In case

of uniform ice nucleation properties, a steep increase would be observed (Niedermeier et al., 2011; Herbert et al., 2014).

To put the efficiency of the CFA particles into perspective, Fig. 4.13 includes fits to LACIS measurements with a K-feldspar sample (76 % microcline, 24 % albite) and different kinds of mineral dust which featured a similar immersion freezing behavior after coating with sulfuric acid (clay mineral baseline) by Augustin-Bauditz et al. (2014). Dry-generated CFA particles are not as efficient as the K-feldspar sample, which is also the most efficient mineral dust sample investigated with LACIS so far, but CFA1 is only 1 order of magnitude below. All of the dry-generated CFA samples are at least 1 order of magnitude above the clay mineral baseline for $T < -29$ °C. In conclusion, the dry-generated CFA particles are comparable to mineral dust in their immersion freezing behavior.

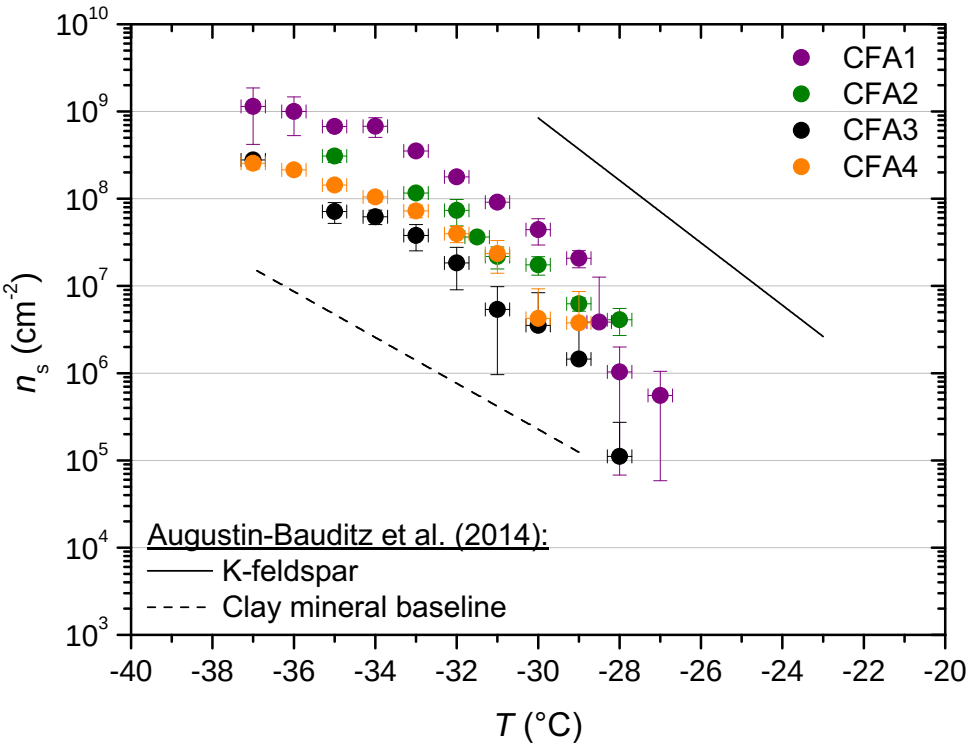

Fig. 4.13.: $n_s(T)$ from LACIS measurements with dry-generated 300 nm particles. Fit lines to LACIS measurements with a K-feldspar sample and different kinds of mineral dust coated with sulfuric acid (clay mineral baseline) are taken from Augustin-Bauditz et al. (2014).

Comparison of LACIS and SPIN

SPIN measurements above water saturation ($1.03 \leq S_{\mathrm{I}} <$ droplet breakthrough) were performed with dry-generated 300 nm particles from all four CFA samples (see Fig. 4.14). For comparison to the LACIS results, SPIN AF data are shown as measured and, additionally, multiplied by a factor of 3, based on results from a previous intercomparison campaign including LACIS and SPIN (Burkert-Kohn et al., 2017) and a comparison between a different continuous flow diffusion chamber and a cloud chamber (DeMott et al., 2015). Corrected data were interpolated for better clarity and are represented by the dashed lines.

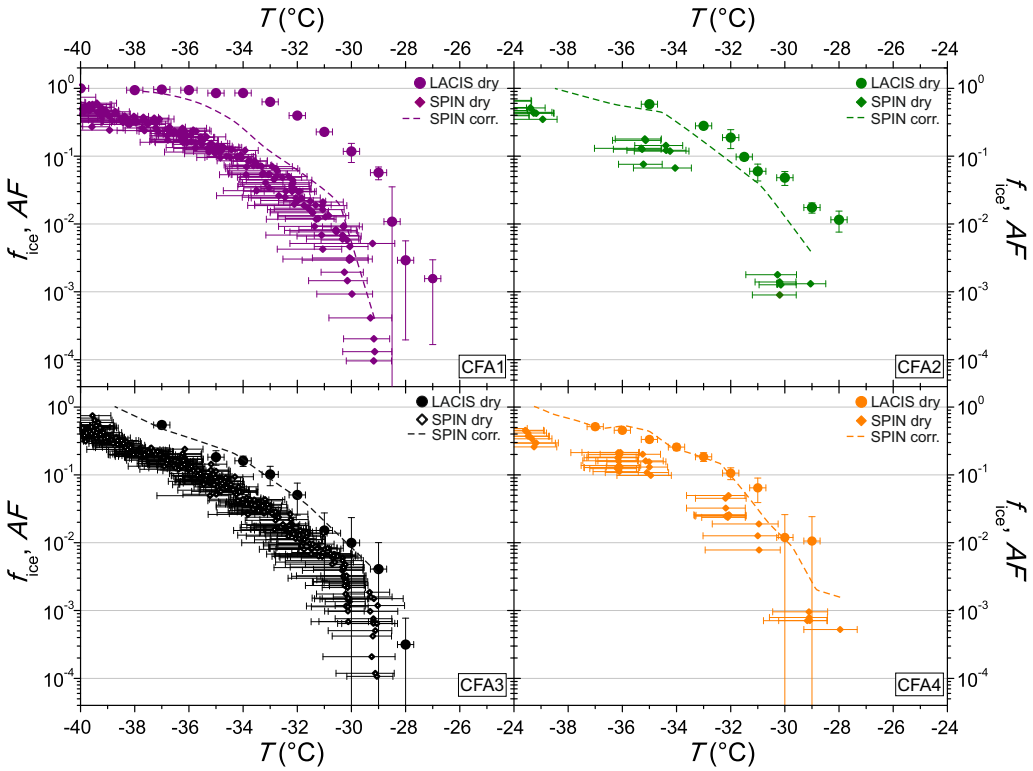

Fig. 4.14.: Comparison of dry particle generation measurements with SPIN and LACIS (300 nm particles). Dashed lines indicate interpolated SPIN data after a correction factor of 3 was applied.

For dry-generated CFA particles, there is nearly perfect agreement between LACIS and SPIN for CFA3 and CFA4 after correction. In case of CFA2, SPIN results are lower than LACIS results, especially for $T \geq -30$ °C. The biggest difference is observed for dry-generated particles of CFA1, where SPIN data is significantly below LACIS for $T \geq -35$ °C. This behavior potentially gives

insight into differences in chemical composition of the samples and the effect of suspension time on the immersion freezing behavior. These issues are discussed in Sec. 5.2.3.

4.2.2 Suspension methods

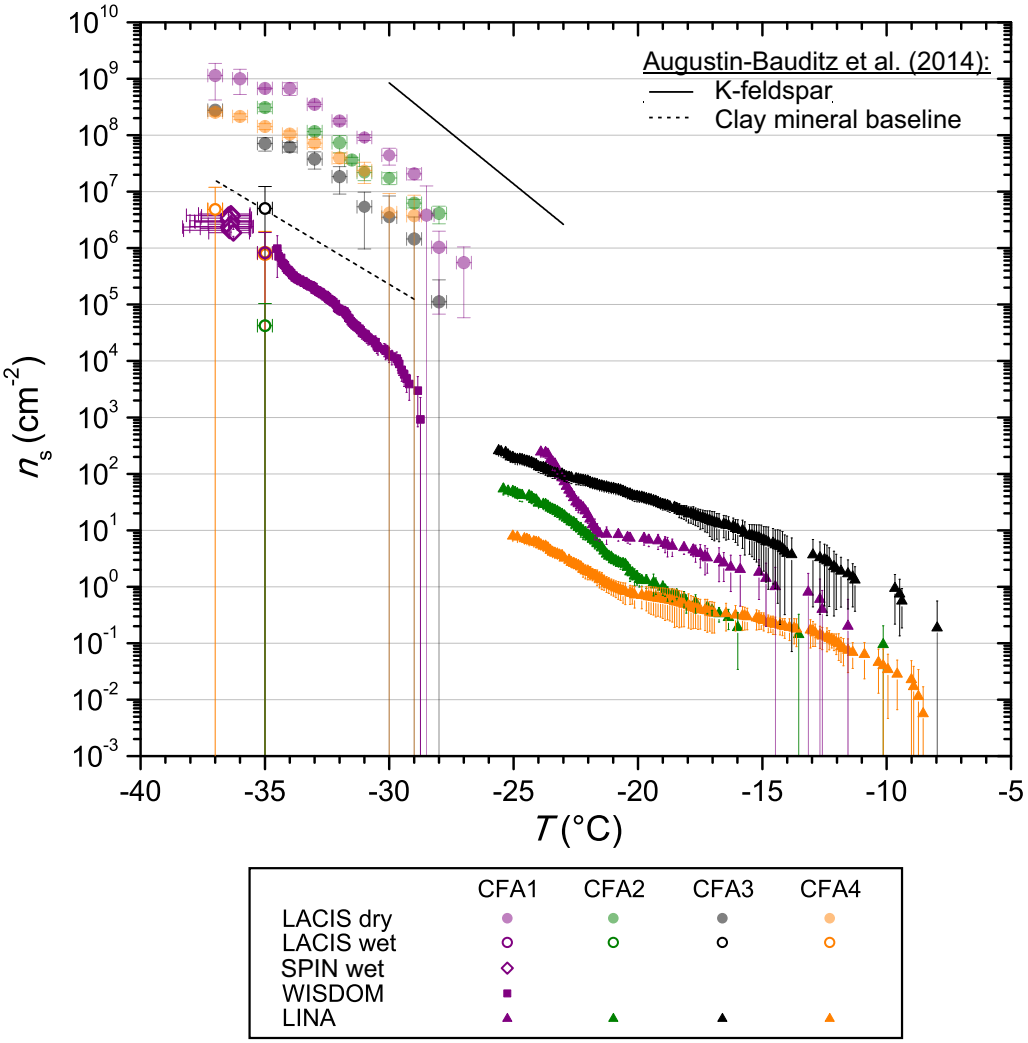

Fig. 4.15.: $n_s(T)$ from immersion freezing measurements with the suspension methods. n_s of LACIS measurements with dry-generated particles (pastel) are included for comparison. Fit lines to LACIS measurements with a K-feldspar sample and different kinds of mineral dust coated with sulfuric acid (clay mineral baseline) are taken from Augustin-Bauditz et al. (2014).

Figure 4.15 summarizes n_s derived from LACIS measurements with wet-generated 300 nm particles (open circles), n_s from SPIN measurements with wet-generated 300 nm particles (open diamonds), n_s from WISDOM measure-

ments with the fine CFA fraction (squares), and n_s from LINA measurements with the bulk CFA (triangles). Be aware that LACIS data for wet-generated CFA were close to the limit of detection which is why measurements could only be performed at one or, at most, two temperature values for the four samples. Also note that SPIN and WISDOM measurements are only available for the CFA1 suspension, due to either instrument availability or technical difficulties. LACIS data from measurements with dry-generated CFA are shown in full pastel circles for comparison. SPIN data from dry particle generation experiments were omitted for clarity. Firstly, LACIS results are described and secondly compared to those of the other three instruments.

LACIS

When comparing n_s from LACIS measurements with dry-generated particles (full circles in Fig. 4.15) to measurements with wet-generated particles (open circles), a significant decrease can be seen. n_s was lowered by between 1 (CFA3) and 4 (CFA2) orders of magnitude at -35 °C. CFA3 is the only sample for which n_s is not lowered to values below the clay mineral baseline. n_s values of wet-generated particles vary by up to 2 orders of magnitude between the four CFA samples, i.e., there is a stronger variation than for dry particle generation. This can be attributed to low values of f_{ice} which are only slightly above values usually measured for homogeneous nucleation (see Fig. C.1), i.e., close to the limit of detection. As a result, the error in f_{ice} and n_s is larger than for the dry-generated particles at the same temperature and one should be cautious when comparing the degree of reduction of n_s of the different samples. Note that data for wet-generated CFA1 particles differ from those published in Grawe et al. (2016), which were misinterpreted. The immersion freezing potential of wet-generated CFA1 particles was quantified by filtering the suspension to remove large needle-shaped particles prior to the LACIS experiments (see Appendix C).

The occurrence of needle-shaped particles suggests that compounds are dissolved from the CFA particles in suspension. During LACIS measurements, purely water-soluble particles, i.e., particles which do not contain water-insoluble material, would activate to droplets which then would only freeze homogeneously, causing an underestimation of f_{ice}. From the size distribution measurements (see Sec. 4.1.3), it can be concluded that a negligibly small number of purely water-soluble particles with a size of 300 nm was produced

from CFA2, CFA3, and CFA4, i.e., the observed decrease in immersion freezing efficiency in the transition from dry to wet particle generation is not caused by a measurement artifact. As stated earlier, the evaluation of the CFA1 size distribution is not unambiguous because of the superimposition of size distributions of spheroidal and needle-shaped particles. However, it is clear from further experiments with the CFA1 suspension (see Appendix C) that the needle-shaped particles are comparable to wet-generated particles from the other samples in their immersion freezing efficiency.

A decrease in the immersion freezing efficiency from dry to wet particle generation was already reported for CFA and coal bottom ash in Grawe et al. (2016). A possible explanation for the observed discrepancy was presented following previous investigations of Hiranuma et al. (2015a), who conducted immersion freezing measurements with both dry-dispersed mineral dust and mineral dust suspensions. There, it was hypothesized that the increased time that the particles spend in contact with water leads to a change in chemical particle properties. For our previous study (Grawe et al., 2016), it was not possible to identify relevant processes because information on the chemical composition of 300 nm particles was missing. As shown in the beginning of this chapter (see Sec. 4.1), differences in chemical composition of dry- and wet-generated CFA particles were identified in the framework of this thesis. These differences are discussed in relation with the immersion freezing results in Sec. 5.2.

Comparison of LACIS, SPIN, LINA, and WISDOM

SPIN measurements with wet-generated CFA particles are shown as open diamonds in Fig. 4.15. Note that corrected data (multiplied by a factor of 3) are shown here. Due to instrument availability, CFA1 is the only sample for which SPIN experiments with wet-generated particles were performed. A decrease in the immersion freezing efficiency of CFA1 in the transition from dry to wet particle generation, which was observed with LACIS, was also measured with SPIN. Although there is no temperature overlap between LACIS and SPIN, both instruments seem to produce similar results considering the overall temperature dependence of n_s indicated by all instruments.

LINA measurements (triangles in Fig. 4.15) were performed between 0 and -26 °C. At this point it shall be mentioned that the water activity of all

CFA suspensions was ∼1, i.e., freezing point depression did not need to be considered. In the temperature range from −8 to −23 °C, CFA3 has the highest, and CFA4 the lowest n_s values of all samples, with those being 2 orders of magnitude apart. The low immersion freezing efficiency of CFA4 in the investigated temperature range could be related to the occurrence of carbonaceous particles, which have previously been found to be inefficient at nucleating ice in the immersion mode (e.g., Chen et al., 2018). It is noteworthy that CFA4 is not the least efficient sample at −35 °C (the orange open circle for CFA4 is directly behind the purple open circle for CFA1) where solely 300 nm particles were investigated instead of bulk material. This behavior suggests that the immersion freezing efficiency of this sample might not scale with the surface area of the particles as proposed by Garimella (2016). CFA1 shows a steep increase in n_s between −21 and −24 °C, below which all droplets were frozen. The last droplets of CFA2, CFA3, and CFA4 suspensions froze below −25 °C. Note that coagulation of particles in the suspensions, which was observed to some extent for CFA suspensions with higher concentrations (see Fig. 4.6) but could not be quantified, might have a reducing effect on the surface area available for ice nucleation in the cold stage measurements (Emersic et al., 2015).

WISDOM measurements (squares in Fig. 4.15) were performed as an attempt to close the temperature gap between LACIS measurements with wet-generated particles ($T \leq -35$ °C) and LINA measurements ($T \geq -26$ °C). This could not be realized for two reasons. Firstly, CFA1 was the only sample that initiated freezing above the homogeneous nucleation limit when using 0.1 g CFA in 100 mL distilled water. Increasing the concentration to a level, for which signals above the homogeneous freezing limit could be expected in the pL droplets, led to settling of the particles in the CFA2, CFA3, and CFA4 suspensions. Secondly, freezing was only observed for $T \leq -29$ °C for CFA1, i.e., there is no temperature overlap between LINA and WISDOM. However, extrapolation suggests that both instruments could yield similar results. Very good agreement can be observed for WISDOM and LACIS at $T \sim -35$ °C with CFA1. At this temperature, the contribution of homogeneous nucleation is still minor in WISDOM measurements and hence it can be concluded that the major contribution to the observed freezing behavior is due to immersion freezing triggered by the CFA particles. The agreement between WISDOM and LACIS firstly implies that drying of the CFA1 suspension droplets after atomization (which does not take place in WISDOM experiments) does not have a strong effect on the immersion freezing efficiency of the particles.

Secondly, the successful instrument intercomparison indicates that there is no pronounced effect of the size-dependent chemical composition on the immersion freezing behavior of CFA1. This finding could be specific to CFA1, as it is in contrast to the observations by Garimella (2016) who found that n_s increases with decreasing particle size.

Concerning the hypothesis that the amorphous material in CFA has a promoting effect on its immersion freezing efficiency (Umo et al., 2015), no clear conclusion can be drawn in the framework of this thesis. XRD investigations show that CFA3 contains the highest amorphous fraction in bulk and probably also in 300 nm particles, as Matsunaga et al. (2002) described an increase of the amorphous fraction towards smaller particle sizes. On the one hand, CFA3 is the most efficient sample measured with the suspension methods LACIS and LINA. On the other hand, dry-generated 300 nm particles of CFA3 are the least efficient of all samples. Potentially, any contribution of amorphous material to the immersion freezing behavior of dry-generated CFA is concealed by the occurrence of more efficient substances (see Sec. 5.2.2).

Summary

In general, 300 nm particles from all dry-generated samples are efficient INPs and comparable to mineral dust in their immersion freezing efficiency. There is some variability with a maximum factor of 37 in the LACIS results from dry particle generation experiments. Concerning the comparison of LACIS and SPIN, it is interesting that both instruments compare well for two of the samples but there is disagreement for the other two samples. Especially towards the higher end of the examined temperature range, SPIN results are below the LACIS results for CFA1 and CFA2. Wet particle generation measurements with LACIS indicate a significant decrease of the immersion freezing efficiency of all samples in comparison to dry particle generation. This was also observed for CFA1 with SPIN. A comprehensive comparison of all suspension methods was only possible for CFA1 due to both instrument availability and technical difficulties. In the case of CFA1, no complete coverage of the whole temperature range from 0 °C to the homogeneous freezing limit could be achieved, but extrapolation of n_s values suggests that LACIS data agree well with SPIN, WISDOM, and LINA.

5 Discussion

In the following chapter, I firstly compare my findings concerning the immersion freezing behavior of CFA particles with results from the literature. In the course of this, all available literature data are compared for the first time. Secondly, I discuss possible connections between physicochemical particle properties and the observed immersion freezing behavior. In relation to this, additional immersion freezing measurements with components contained in the CFA samples are presented. Finally, I introduce a method for roughly estimating the relevance of CFA particles for atmospheric ice nucleation.

5.1 Comparison to literature results

5.1.1 Havlíček et al. (1993)

A comparison of my results to findings by Havlíček et al. (1993) is not trivial because, firstly, information on the specific surface area of the samples is missing in this study and secondly, investigations were only performed at $T = -15$ °C. Havlíček et al. (1993) provided the mass of the samples used in their immersion freezing experiments, which can be used to calculate the number of ice nucleation active sites per unit mass n_{m} according to Eq. (5.1). The results of these calculations for the nine samples from the former Czechoslovakia in relation to the LINA measurements at -15 °C can be seen in Fig. 5.1. Generally, there is good agreement between the investigations by Havlíček et al. (1993) and the LINA measurements, as seven of the nine Czechoslovakian samples are included in the n_{m} range given by the four German samples within the LINA measurement uncertainty. However, among the Czechoslovakian samples there are two outliers which cause an overall variation of more than 4 orders of magnitude in n_{m}. In contrast, the n_{m} values of the German samples only vary within a factor of 15. The lowest n_{m} value belongs to the only black coal CFA in case of the Czechoslovakian samples, whereas CFA3 (the only black coal CFA in the German sample set) has the second highest efficiency. This implies that neither the geographical origin of the coal nor the coal type allows for any

conclusions concerning the immersion freezing efficiency of the particles. An important caveat is that the n_{m} concept is probably not well suited for CFA because it does not take the specific surface area into account. This factor could indeed contribute to the large variation in the Havlíček et al. (1993) study, but it is unlikely that differences in the specific surface area cause a shift of the immersion freezing efficiency by more than 1 order of magnitude (Grawe et al., 2016). The n_{m} concept is traditionally used for water-soluble biological INPs (e.g., O'Sullivan et al., 2015; Wex et al., 2015; Pummer et al., 2015), whereas n_{s} is the better choice for water-insoluble INPs such as mineral dust (e.g., Broadley et al., 2012; Atkinson et al., 2013; Emersic et al., 2015). The fact that Havlíček et al. (1993) observed a decrease in the deposition nucleation efficiency of the separated, water-insoluble components in comparison to the original samples (see Sec. 2.2.2) is potentially mirrored by the reduction of the immersion freezing efficiency with the change from dry to wet particle generation found in the framework of this thesis. One might speculate that similar mechanisms could be responsible in both cases, however, no definite conclusion can be drawn since different nucleation modes were investigated.

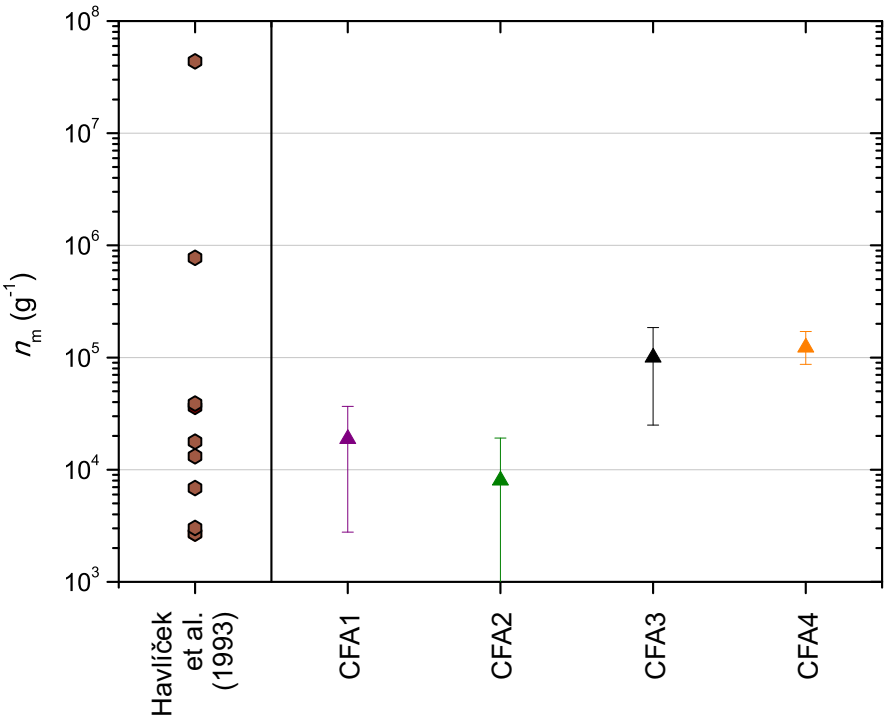

Fig. 5.1.: $n_{\mathrm{m}}(-15\ ^{\circ}\mathrm{C})$ values from cold stage measurements with nine different CFA samples from the former Czechoslovakia by Havlíček et al. (1993). $n_{\mathrm{m}}(-15\ ^{\circ}\mathrm{C})$ values from LINA measurement with CFA1, CFA2, CFA3, and CFA4 are included for comparison.

$$n_{\mathrm{m}}(T) = -\frac{\ln(1 - f_{\mathrm{ice}}(T))}{V_{\mathrm{d}} \cdot C} \tag{5.1}$$

5.1.2 Garimella (2016)

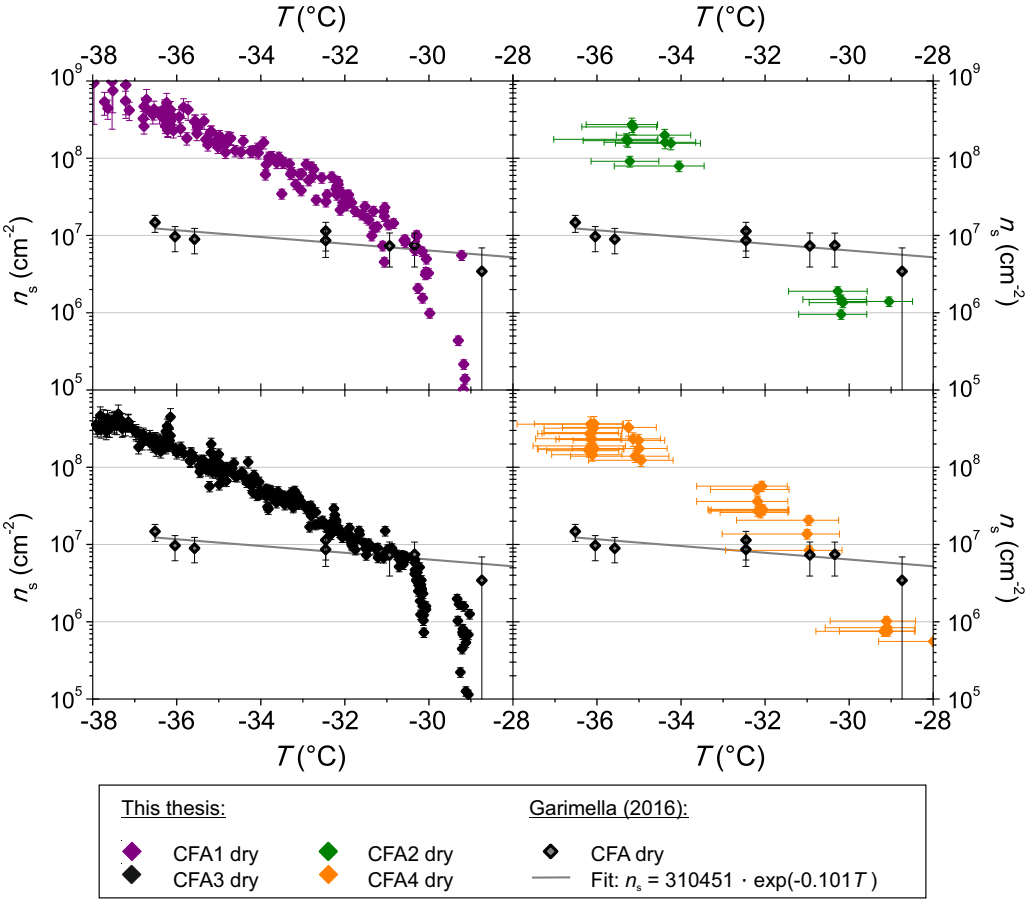

Fig. 5.2.: $n_{\mathrm{s}}(T)$ from SPIN measurements with dry-generated 300 nm CFA particles. Horizontal error bars are omitted in the CFA1 and CFA3 panels for greater clarity but are comparable to the values shown in the CFA2 and CFA4 panels. Measurements with four CFA samples from the USA (Garimella, 2016; all shown with identical markers) are included for comparison.

Figure 5.2 shows a comparison of SPIN measurements with 300 nm CFA particles between this study and Garimella (2016), who performed immersion freezing measurements with four CFA samples from the USA, two class C and two class F samples. Note that all samples investigated by Garimella (2016) are shown with the same markers as no large inter-sample variability was observed. Horizontal error bars indicating the temperature uncertainty

are only included for CFA2 and CFA4. This was done for greater clarity in the case of CFA1 and CFA3, for which more data are available. Temperature uncertainties are comparable for all cases. Only towards the warmer end of the examined temperate range, n_s of the samples from the USA is comparable to what was found for the here examined samples from Germany. At -36.5 °C, the lowest temperature at which both instruments have been operated, n_s of the samples from the USA is up to 2 orders of magnitude lower than n_s of the German samples. In general, the n_s spectra of the samples from the USA have a much shallower slope than the German CFA n_s spectra. As the same type of instrument was used for both investigations, I conclude that differences between the German samples and the samples from the USA originate from differences in physicochemical particle properties, and not from differences in methodology. Both SPIN experiments, the one performed in the framework of this thesis and that of Garimella (2016), have in common that no large inter-sample variability was observed. This is in contrast to the LACIS measurements, where the class C CFA (CFA1) clearly has the highest efficiency. See Sec. 5.2.3 with regard to possible reasons for the deviation between LACIS and SPIN in the framework of this thesis.

5.1.3 Umo et al. (2015)

Cold stage measurements with a CFA sample of unknown origin by Umo et al. (2015; see Fig. 5.3) yielded results that differ substantially from what was measured in the framework of this study. The efficiency of the sample investigated by Umo et al. (2015) increases strongly for -20 °C $< T < -15$ °C and levels off from $T < -25$ °C. This is in contrast to the gradual increase over a broad temperature range that was observed for the here investigated samples. For this thesis, suspensions were prepared in the same way as described by Umo et al. (2015). Also, LINA and the µL-NIPI, i.e., the instrument used by Umo et al. (2015), have successfully been intercompared with a different ash sample (see Fig. 5.4). Therefore, it can be inferred that the CFA samples are really different in their immersion freezing behavior and that the observed differences do not stem from artifacts related to methodology.

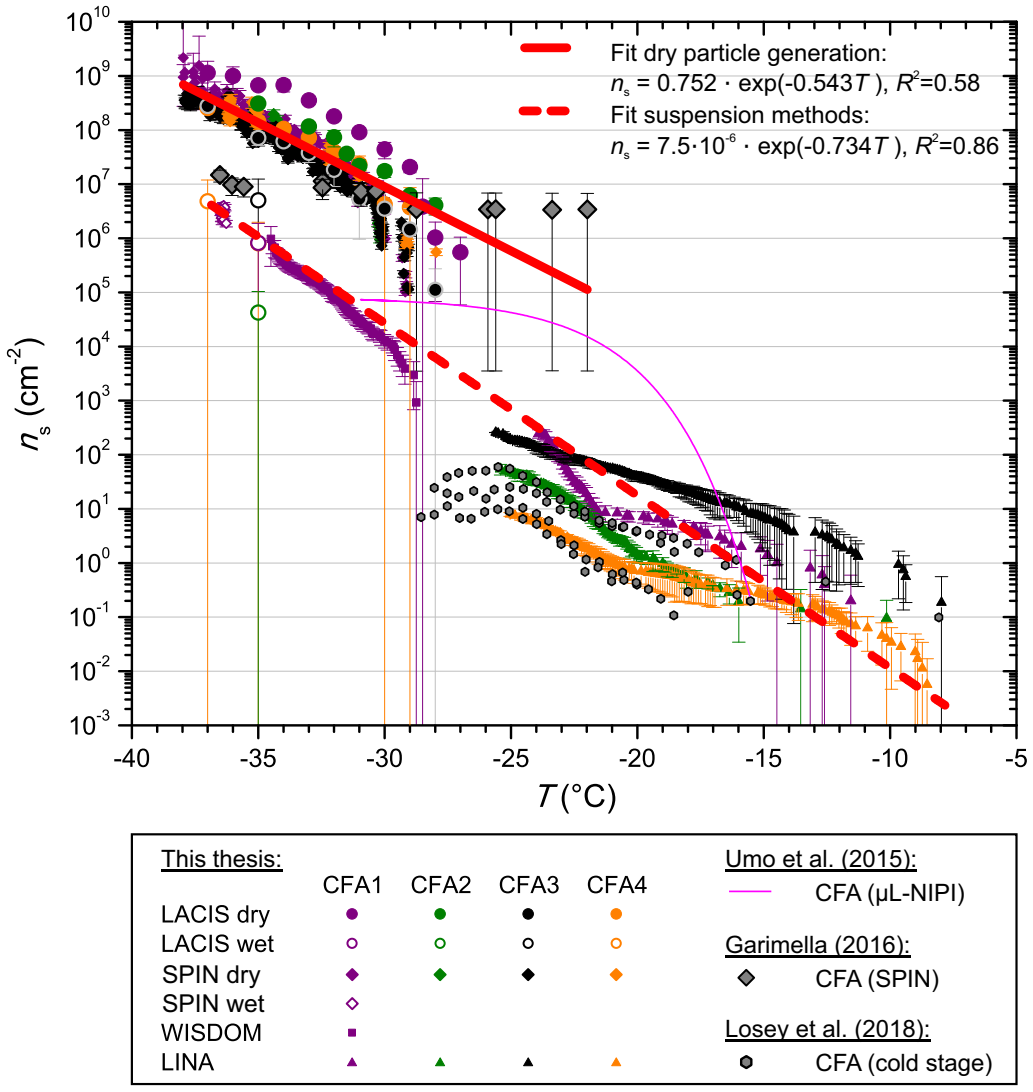

Fig. 5.3.: Summary of immersion freezing $n_s(T)$ data from this thesis and the literature. Dry particle generation data and suspension data were considered separately to yield two fit equations.

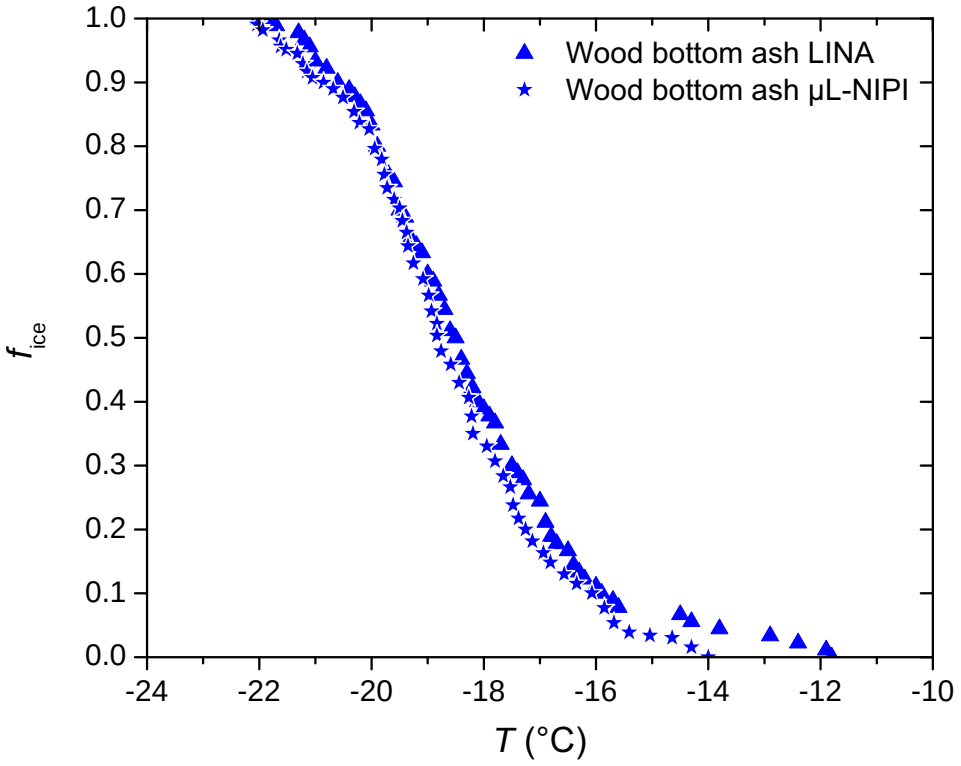

Fig. 5.4.: $f_{\mathrm{ice}}(T)$ values from LINA and µL-NIPI measurements. Both measurements were performed with identically prepared suspensions of a wood bottom ash sample (Umo et al., 2015).

5.1.4 Losey et al. (2018)

Losey et al. (2018) investigated the same commercial samples from the USA as Garimella (2016) but with a cold stage setup (Alstadt et al., 2017). The samples were prepared in such a way that 0.4 g CFA were combined with 15 mL of ultrapure water, stirred for 1.5 h, and centrifuged. After the supernatant was decanted, the sample was left for several days until all remaining water had evaporated. Once dry, the sample was used for cold stage experiments by again preparing a suspension with ultrapure water (0.3 wt%). Note that this routine, in contrast to the suspension preparation described by Umo et al. (2015) which was also applied in this thesis, leads to leaching of certain ions which are washed away when decanting the supernatant. The results can be seen in Fig. 5.3 where all samples from Losey et al. (2018) are shown with the same markers (error bars were omitted for better clarity). The decrease of n_{s} with decreasing temperature below ~ -25 °C is a result of the water background correction and indicates the regions where

heterogeneous nucleation caused by the impurities in the water outpaces heterogeneous nucleation caused by the CFA particles. This was not observed for the samples investigated in the framework of this thesis. Apart from that, the samples investigated by Losey et al. (2018) show an n_s spectrum which is within the limits given by CFA3 and CFA4 for $-25\ °C < T < -8\ °C$, i.e., both sample sets are similar in both temperature dependence and magnitude of n_s when similar methods are used. Interestingly, comparable agreement cannot be found for the dry-generated 300 nm particles from the same sample sets (see Fig. 5.2), again indicating the complexity of immersion freezing measurements with CFA. The comparison between Losey et al. (2018) and Garimella (2016), i.e., wet- and dry-generated particles of identical samples (see Fig. 5.3), reveals a discrepancy of almost 7 orders of magnitude at $-22\ °C$, with the dry-generated particles being significantly more efficient. Even though this difference is larger than the difference between dry particle generation and suspension methods in the framework of this thesis ($\sim$4 orders of magnitude between LACIS and WISDOM for CFA1 at $-28\ °C$), the same trend can be observed for both sample sets. Unlike the LINA results, measurements by Umo et al. (2015) are up to 4 orders of magnitude higher than the results by Losey et al. (2018).

Summary

The comparison of my data to Havlíček et al. (1993), Umo et al. (2015), Garimella (2016), and Losey et al. (2018) allows for two conclusions. Firstly, CFA samples from different origin show a highly variable immersion freezing behavior. Secondly, a part of this variability is introduced by differences in methodology. Discrepancies in the immersion freezing efficiency of up to 7 orders of magnitude can be observed for one sample depending on instrumentation and particle generation/suspension preparation techniques. All n_s data for immersion freezing of CFA which are available in the literature are summarized in Fig. 5.3 together with data from this thesis. Results of measurements with dry-generated CFA particles and suspension measurements were fit separately to facilitate a comparison of future results to the existing data set according to the used method. The fit equation for dry particle generation methods (this thesis: LACIS and SPIN; Garimella, 2016: SPIN) is $n_s = 0.752 \cdot \exp(-0.543T)$ and the fit equation for the suspension methods (this thesis: LACIS, SPIN, WISDOM, LINA; Umo et al., 2015: µL-NIPI; Losey et al., 2018: cold stage) is $n_s = 7.5 \cdot 10^{-6} \cdot \exp(-0.734T)$.

5.2 Physicochemical particle properties and immersion freezing behavior

So far it has become obvious that different CFA samples show varying immersion freezing efficiencies and that investigating one and the same sample with different methods might yield deviating results. In this section, I discuss how the immersion freezing efficiency of CFA particles is influenced by physicochemical properties. The focus is on the identification of substances that influence the immersion freezing behavior of the dry-generated CFA particles and possibly cause the observed decrease in the transition from dry to wet particle generation. The section is structured as follows: Firstly, species possibly influencing the immersion freezing behavior of the dry-generated particles are identified by analyzing ALABAMA mass spectra in conjunction with the immersion freezing efficiency from LACIS measurements. Secondly, additional LACIS measurements with the pure, dry-generated identified species are presented in comparison to the CFA results. Thirdly, measurements with the hydration products of the identified species from the literature are compared to the CFA measurements with the suspension methods. Finally, the effect of sample treatment (suspension time, drying, heating) on the immersion freezing behavior of both CFA and the identified substances is discussed.

5.2.1 ALABAMA signal intensity and CFA immersion freezing efficiency

Averaged mass spectra of dry-dispersed CFA particles were used for identifying species that contribute to or do not seem to have an impact on the observed immersion freezing behavior. This was done by searching the mass spectra for species whose signal intensity correlates or anti-correlates with f_{ice} from LACIS measurements of the CFA samples (see Fig. 5.5). In case of correlation (see Fig. 5.5 a), only those mass-to-charge ratios are shown for which the signal intensity is highest for CFA1 and lowest for CFA3. In case of anti-correlation (see Fig. 5.5 b), only those mass-to-charge ratios are shown for which the signal intensity is highest for CFA3 and lowest for CFA1. CFA2 and CFA4 were not considered separately because they have a very similar immersion freezing efficiency which is in between that of CFA1 and CFA3.

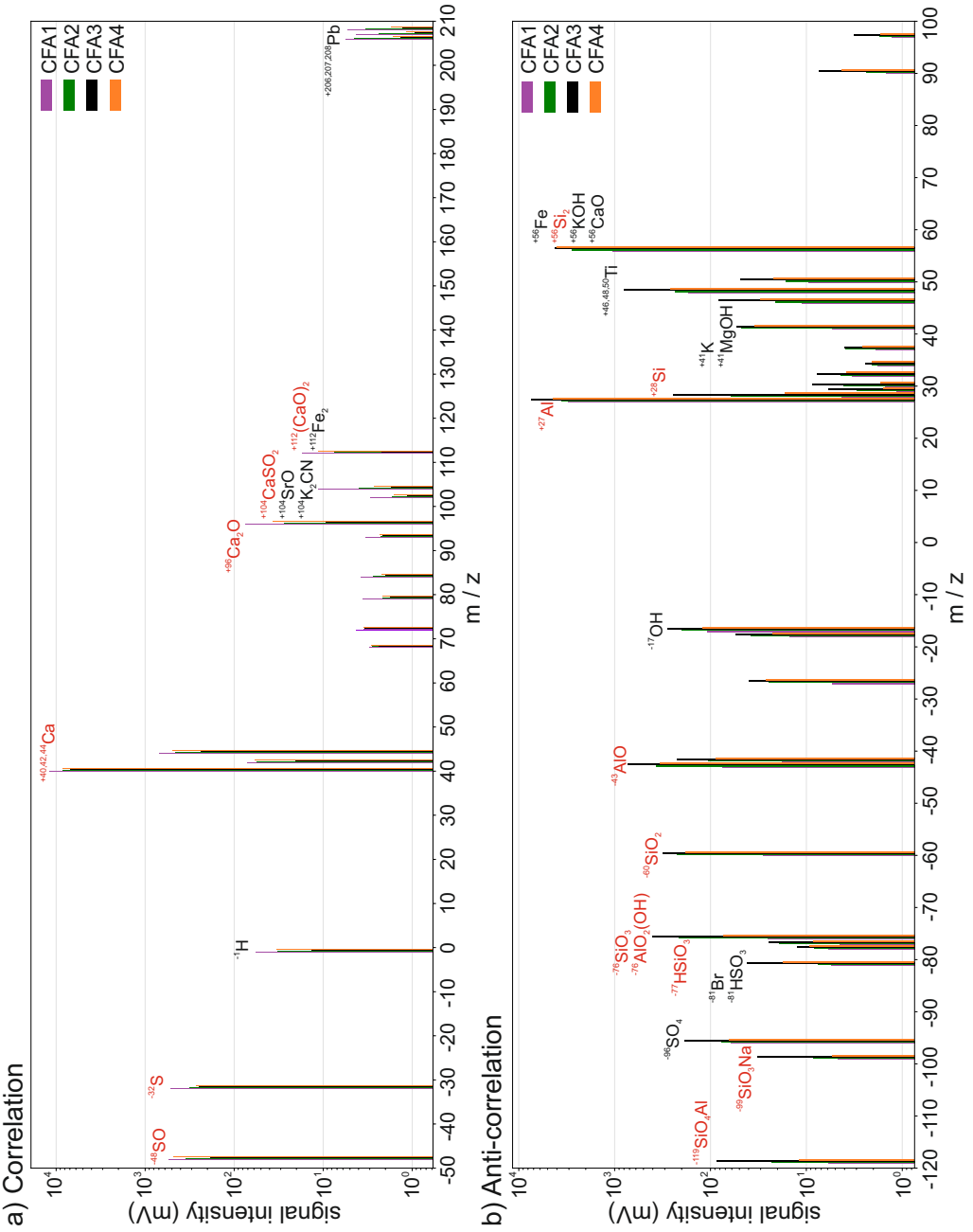

Fig. 5.5.: Averaged mass spectra. Shown are only those mass-to-charge ratios for which the signal intensity a) correlates (CFA1>CFA2,CFA4>CFA3) or b) anti-correlates (CFA3>CFA2,CFA4>CFA1) with f_{ice} of dry-generated CFA. Red labels indicate Ca- and S-containing species in case of correlation and Si- and Al-containing species in case of anti-correlation. Species with signal intensities < 10 mV were not considered, except for mass-to-charge ratios [+206, +207, +208] indicating a correlation with Pb.

Certain groups of compounds appear more often than others in relation to the total number of correlating/anti-correlating species. Ca- and S-containing species [$^{+40}$Ca, $^{+42}$Ca, $^{+44}$Ca, $^{+96}Ca_2O$, $^{+104}CaSO_2/SrO$, $^{+112}(CaO)_2$, $^{-32}$S, $^{-48}$SO] have the highest signal intensities for CFA1 and lowest for CFA3. As stated earlier, the simultaneous occurrence of the Ca cation and S anion series hints at the presence of anhydrite (Gallavardin et al., 2008). A correlation can also be seen for Pb[$^{+206}$Pb, $^{+207}$Pb, $^{+208}$Pb]. Anti-correlation was found for many compounds amongst which Si- and Al-containing species occur frequently [$^{-60}SiO_2$, $^{-76}SiO_3$, $^{-77}HSiO_3$, $^{-99}NaSiO_3$, $^{-119}AlSiO_4$, $^{+28}$Si, $^{+56}Si_2$, $^{-43}$AlO, $^{-119}AlSiO_4$, $^{+27}$Al]. Briefly, the immersion freezing behavior of the dry-generated particles seems to be influenced by species containing Ca and S, and possibly by trace elements. Si and Al do not appear to contribute to the observed differences in the immersion freezing efficiency of the dry-generated samples.

5.2.2 Comparision between CFA and identified substances

Dry particle generation

Anhydrite and quicklime, were chosen as test substances for additional LACIS measurements. Both substances are known to occur in CFA and are enriched in submicron CFA particles (Enders, 1996; Querol et al., 1996). Anhydrite is of special interest because Havlíček et al. (1993) found that the water-soluble material on the CFA particle surface is mainly anhydrite and suggested that it is responsible for initiating heterogeneous freezing on the particles. To my knowledge, the here presented are the first immersion freezing measurements using dry-generated anhydrite and quicklime particles.

Both anhydrite and quicklime are efficient INPs in the immersion mode when being dry-generated (see Fig. 5.6). Note that a multiple charge correction was not possible for LACIS measurements with anhydrite and quicklime because these data were acquired following the campaign, i.e., ALABAMA size distribution measurements were not available. The correction would shift the n_s spectra of anhydrite and quicklime towards lower n_s values but the slope would stay the same. Generally, the multiple charge correction lowers n_s values for the dry-generated CFA particles by less than a factor of 3.5 and I

expect that it would be comparable for the anhydrite and quicklime particles. Anhydrite is more efficient than quicklime at $T = -35$ °C (∼factor 2) and less efficient at $T = -30$ °C (∼factor 5), i.e., there is a slightly steeper slope of the anhydrite n_s spectrum. Shape and magnitude of the anhydrite n_s spectrum are comparable within measurement uncertainty to what was found for CFA2 and CFA4. CFA3, which contains the lowest concentration of Ca and S, and presumably the lowest concentration of anhydrite in 300 nm particles, is less efficient than pure anhydrite. CFA1 is more efficient than pure anhydrite, indicating that other compounds might influence the immersion freezing efficiency of this sample. A possible component contributing to n_s of CFA1 might be Pb, which occurs in 20 % of 300 nm particles from CFA1 (in ≤10 % of particles from CFA2, CFA3, and CFA4, see Fig. 4.2) and has previously been discussed as a potential INP, or as amplifying the ice nucleation efficiency of other compounds (Cziczo et al., 2009; Kamphus et al., 2010).

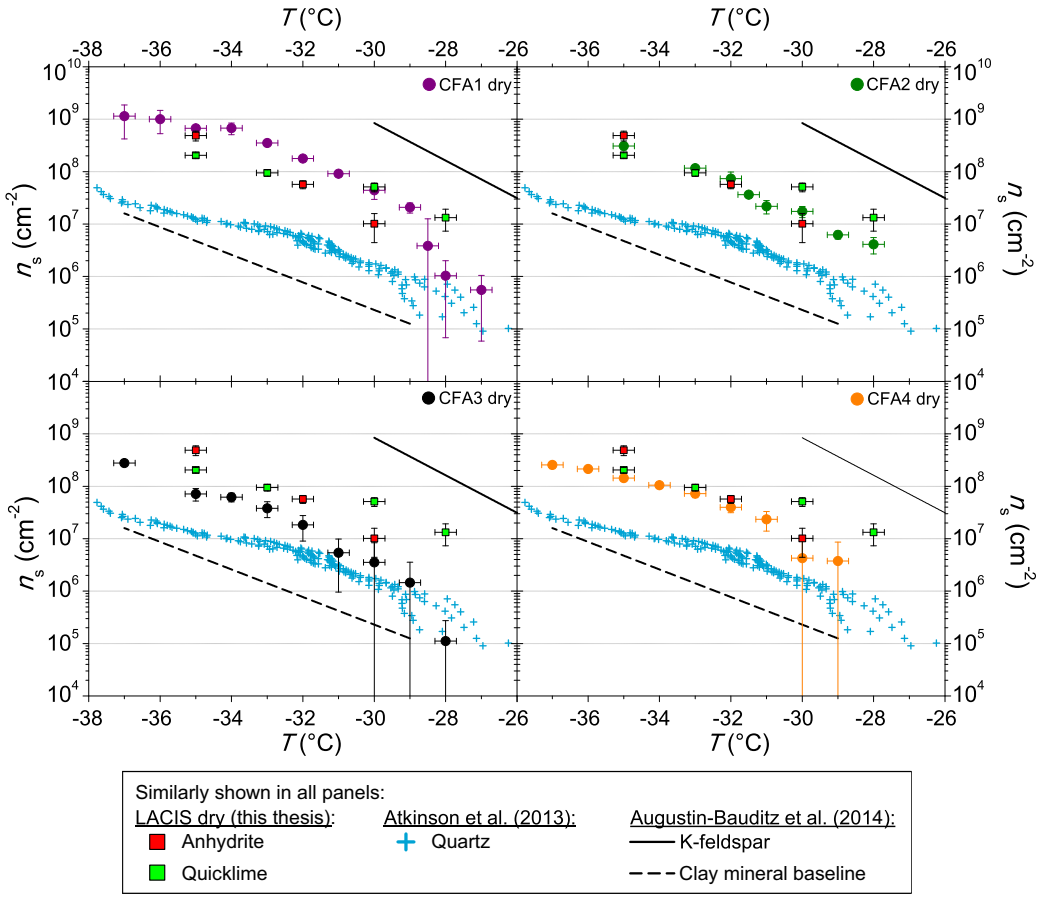

Fig. 5.6.: $n_s(T)$ from LACIS measurements with dry-generated CFA, anhydrite and quicklime particles. Note that data for anhydrite and quicklime are, in contrast to CFA, not corrected with respect to multiple charges. Measurements with quartz shown in all panels are taken from Atkinson et al. (2013).

Quartz, which is the main crystalline phase of all CFA samples according to XRD measurements and likely also occurs in 300 nm CFA particles (Si was identified by both ALABAMA and ESEM/EDX), is at least 1 order of magnitude less efficient than CFA1, CFA2, and CFA4 below −30 °C (see Fig. 5.6). The CFA results are compared to cold stage measurements of quartz suspension droplets by Atkinson et al. (2013) because this dataset spans the relevant temperature range and due to the lack of immersion freezing results of dry-generated quartz particles in the literature. n_s of CFA3, which contains the highest concentration of Si (presumably quartz) in 300 nm particles, is higher by a factor of 2 to 10 compared to the quartz n_s spectrum. This indicates that quartz might contribute to some of the observed immersion freezing behavior in the case of CFA3, but it is probably less governing in CFA1, CFA2, and CFA4. ALABAMA results showing that 300 nm particles in CFA1 have the lowest concentration of Si-containing compounds, followed by CFA2 and CFA4, support this hypothesis (see Fig. 5.5 b).

Suspension methods

It is a challenge to identify reactions responsible for the decrease in immersion freezing behavior in the measurements with the suspension methods because of the heterogeneity of the CFA samples. A comparison of ALABAMA measurements of dry- and wet-generated CFA particles hints at the hydration of several oxides (see Fig. 4.3). For bulk CFA1, there is clear evidence from XRD measurements that anhydrite and quicklime, which were already identified as species potentially influencing immersion freezing of the dry-generated particles, are hydrated in suspension, resulting in the formation of gypsum and calcite (see Fig. 4.7). Viewing XRD patterns of the original samples in comparison with samples after suspension and evaporation shows no change concerning the quartz phase. In the following, I compare immersion freezing results of CFA suspension particles to measurements of gypsum, calcite, and quartz by Atkinson et al. (2013) and Zolles et al. (2015).

In comparison to dry-generated anhydrite and quicklime (see Fig. 5.6), gypsum and calcite are lower in their immersion freezing efficiency by 3 orders of magnitude (see Fig. 5.7), i.e., as for CFA, there is a significant decrease in the efficiency of the hydration products compared to their anhydrous precursors. In general, gypsum and calcite are similar to each other in their immersion freezing behavior. LACIS measurements with wet-generated CFA

and WISDOM measurements agree with the gypsum and calcite results within 1 order of magnitude. The only exception to this is CFA3 which is discussed below in relation with quartz.

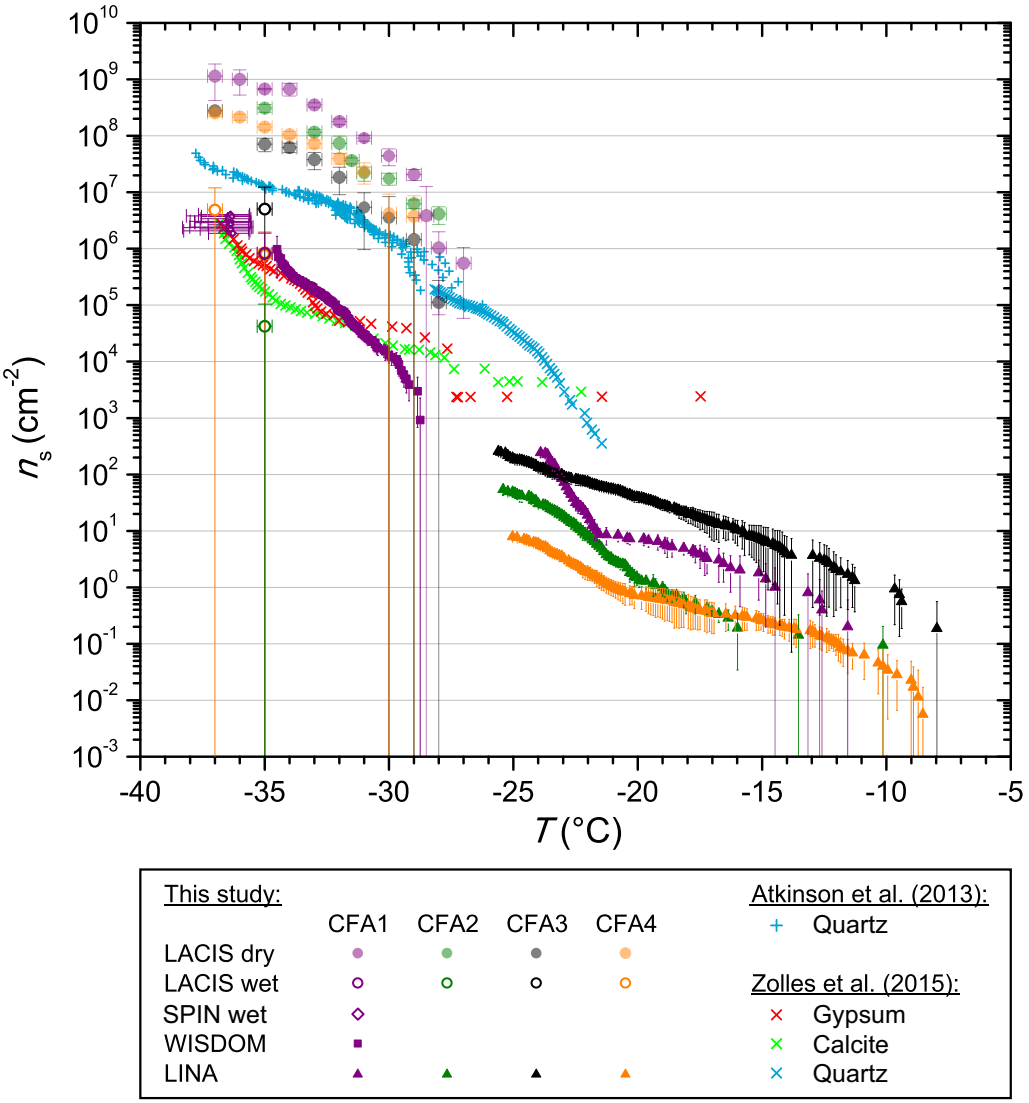

Fig. 5.7.: $n_s(T)$ from CFA immersion freezing measurements with the suspension methods. Measurements with gypsum, calcite, and quartz are taken from Zolles et al. (2015) and Atkinson et al. (2013). Results from LACIS measurements with dry-generated CFA particles are included in pastel for comparison.

The hydration of anhydrite inevitably takes place once CFA comes into contact with water, because anhydrite is often present at the particle surface. Anhydrite forms in the reaction of SO_2, O_2, and quicklime in the power plant and preferentially condenses on the surface of the quickly cooling, small CFA particles (Enders, 1996). Sievert et al. (2005) describe the hydration of pure anhydrite particles according to Fig. 5.8. Firstly, anhydrite is dissolved

from the particles and Ca^{2+} and SO_4^{2-} ions are hydrated in the solution. The hydrated ions are then adsorbed to the surface of the anhydrite particles due to electrostatic attraction (b). From this point on, further dissolution and interaction of water molecules with the anhydrite surface is reduced because of the adsorbed layer of hydrated ions. Secondly, as the thickness of the adsorbed layer increases (c), cracks are formed through which water molecules migrate to the anhydrite surface (d). Only then, nuclei of gypsum are formed (e) and crystallization takes place (f). According to Sievert et al. (2005), the first process, i.e., the formation of the adsorbed layer of hydrated ions, is thought to happen rather quickly on the time scale of seconds to minutes. The second process, i.e., the formation of gypsum, can take several hours up to days. See Sec. 5.2.3 and 5.3 for details on the duration of the hydration process for CFA particles.

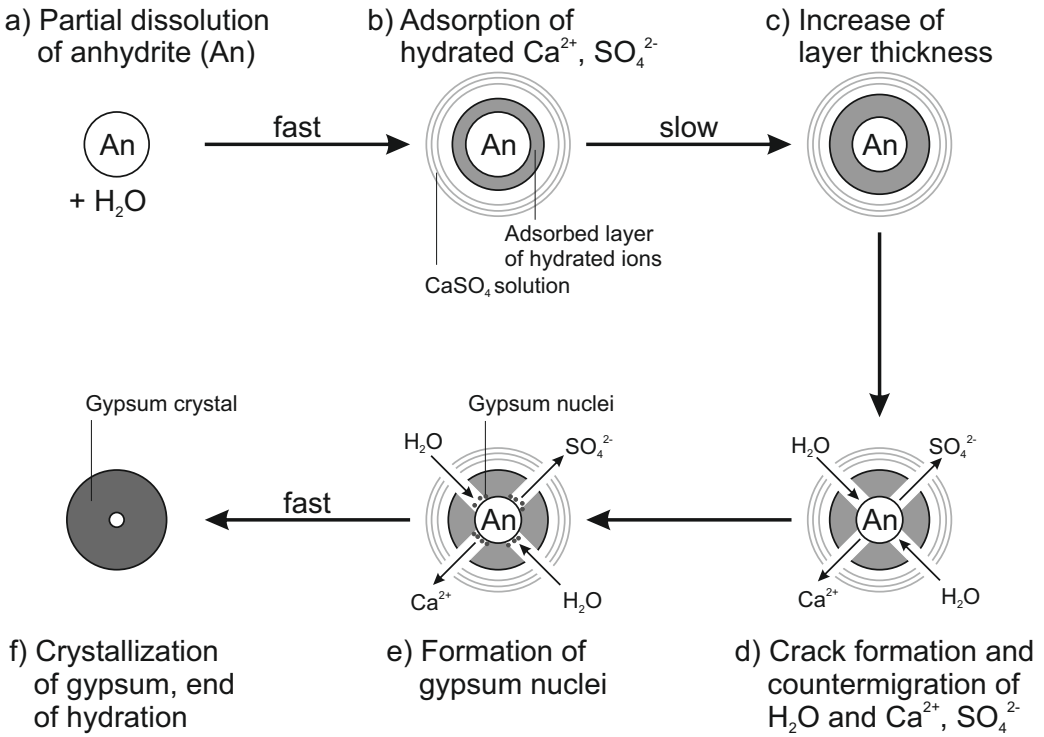

Fig. 5.8.: Two-step hydration mechanism of pure anhydrite particles in water. Adapted from Sievert et al. (2005).

The formation of calcite occurs via the hydration of quicklime to portlandite which is then carbonated (see reactions (4.10) and (4.11)). It is possible that this process causes the precipitation of the needle-shaped particles in suspension, but only if the quicklime content is sufficiently high, as for

CFA1. It cannot be ruled out that calcite is also formed in the other CFA suspensions, but in contrast to CFA1, calcite could not clearly be identified in the other samples by XRD. Both above described mechanisms (anhydrite and quicklime hydration), and potentially even more hydration reactions (see Sec. 4.1.1), might cause the observed decrease in immersion freezing efficiency in transition from dry to wet particle generation. Additional LACIS measurements with different sample treatments were performed to verify this hypothesis and are discussed below in Sec. 5.2.3.

In addition to the quartz measurements by Atkinson et al. (2013), quartz measurements by Zolles et al. (2015) are now included in the discussion because they cover $T > -28$ °C, which is the more relevant temperature range for the cold stage measurements with CFA. The n_s spectra of the quartz samples used by Zolles et al. (2015) and Atkinson et al. (2013) agree in the narrow temperature overlap (-26 °C $< T < -28$ °C). It is obvious that quartz is significantly more efficient in the immersion mode than suspended particles of CFA1, CFA2, and CFA4, with n_s being at least 1 order of magnitude higher in the investigated temperature range (see Fig. 5.7). The deviation is smallest at ~ -22 °C for CFA3 which contains the highest concentration of Si species (presumably quartz) and lowest concentration of Ca and S species in 300 nm particles. For this sample, I assume the smallest effect of the hydration reactions and a larger influence of quartz on the immersion freezing behavior compared to the other samples. The fact that the other samples also contain significant amounts of quartz, both in 300 nm particles and in bulk, and nevertheless feature a much lower efficiency when investigated with the suspension methods, supports the hypothesis of the particles being covered by a layer. In the case of the dry particle generation method, the layer is more efficient at initiating immersion freezing than quartz. In the case of the suspension methods, the layer is less efficient than quartz, with this change brought on by the above described hydration reactions. Quartz could also contribute to the high efficiency of the CFA sample investigated by Umo et al. (2015) between -16 and -30 °C. This sample did not contain detectable concentrations of anhydrite or quicklime but 7.1 % quartz.

5.2.3 Effect of sample treatment

Additional LACIS measurements with differently treated CFA and anhydrite samples, as well as pure gypsum, were performed in order to test the hypothesis that the hydration of anhydrite leads to a decrease of the immersion freezing efficiency in suspension (see Fig. 5.9). All measurements were performed at −35 °C with 300 nm particles. Here, I forewent the multiple charge correction for better comparability to measurements that took place after the campaign when no correction was possible. The corrected values for CFA, which were used for the calculation of the earlier presented n_s values, are shown as pastel circles.

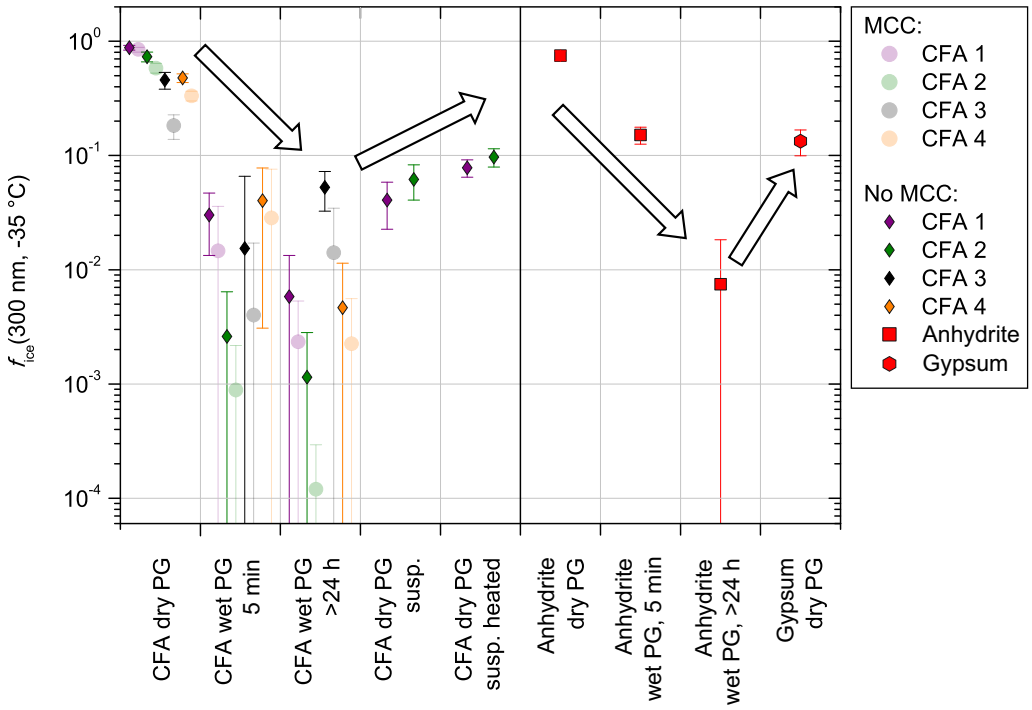

Fig. 5.9.: f_{ice}(300 nm, −35 °C) from LACIS measurements with differently treated samples. The arrows indicate the decrease and increase of the immersion freezing efficiency due to hydration and dehydration which was observed for both CFA and anhydrite. A multiple charge correction (MCC) was not performed, except for the measurements indicated by the pastel circles in the first three columns. "Dry PG susp." means dry particle generation (PG) with a sample resulting from the evaporation of a suspension and "dry PG susp. heated" means additional heating of this sample to 250 °C prior to particle generation.

When comparing dry-generated CFA particles with wet-generated particles, either from a fresh suspension (i.e., measured within 5 min after preparation), or from the standard suspension (10 min of ultrasonification and 24 h of stirring), a decrease in $f_{ice}(-35\ ^{\circ}C)$ can be observed. The particles from the freshly prepared suspension seem to be slightly more efficient than the ones from the standard suspension. The only exception is CFA3, for which it was extremely difficult to generate a sufficiently high particle number concentration from the fresh suspension, resulting in a large error due to the small amount of classified hydrometeors ($\sim$500). Dry- and wet-generated anhydrite particles show the same trend as observed for CFA, i.e., the wet-generated particles are significantly less efficient than the dry-generated particles, and the longer the particles stay in suspension, the stronger the decrease in f_{ice}. This observation is a forceful indicator of anhydrite being the reason for both the high efficiency of dry-generated CFA particles and the decrease with elongated suspension times. The fact that a significant decrease in immersion freezing efficiency can also be seen for the fresh CFA suspensions which were not stirred, i.e., not in contact with the magnetic agitator, suggests that the removal of magnetic material from the CFA suspensions (see Sec. 4.1.2) is not causing the quasi-deactivation.

Sullivan et al. (2010) found an increase in hygroscopicity of wet-generated anhydrite particles in comparison to dry-generated particles. Also, the hygroscopicity of the wet-generated particles increased with the time that the particles spent in the suspension. Sullivan et al. (2010) attributed this behavior to the formation of hydrates and hypothesized that this process could have an effect not only on hygroscopicity but also on the ice nucleation efficiency of the particles. The dependency of hygroscopicity and immersion freezing efficiency on suspension time could result from the two stages of anhydrite hydration described in Sec. 5.2.2. Firstly, on the time scale of minutes, anhydrite is dissolved and hydrated ions form a layer on top of the CFA particles causing a sudden decrease in immersion freezing efficiency. It seems that the limited suspension time of 1.6 s, that a particle experiences when activated to a droplet in LACIS in case of dry particle generation experiments, is not sufficient to cause the formation of such a hydrated layer. Secondly, on the time scale of several hours up to days, anhydrite is converted into gypsum, causing a further decrease of f_{ice}. Gypsum, like anhydrite, consists of molecules which are strong electrical dipoles (Klimchouk, 1996) and hence will also be surrounded by hydrated ions when suspended for a sufficient amount of time.

The ultrasonicated and stirred suspensions of CFA1 and CFA2 were left in a desiccator (steady flow of particle free, dry air) until all water was evaporated. XRD measurements of the resulting powder show that the anhydrite-gypsum conversion had taken place (see Fig. 4.7 and 4.8). The powder was then dry-dispersed and $f_{\mathrm{ice}}(-35\ ^{\circ}\mathrm{C})$ of 300 nm particles was measured. An increase of $\sim$1 order of magnitude for CFA1 and $\sim$2 orders of magnitude for CFA2 in comparison to the wet-generated particles was registered. For wet particle generation, possibly only the bulk water is removed in the diffusion dryer downstream of the atomizer, whereas the water molecules in the layer of hydrated ions remain. Drying in a desiccator could lead to a partial dehydration, i.e., the removal of the hydrated layer surrounding the CFA particles but not of the embedded water from the crystal structure. Similar values of $f_{\mathrm{ice}}(-35\ ^{\circ}\mathrm{C})$ of dry-generated particles from the evaporated CFA suspensions and dry-generated gypsum particles support this hypothesis.

Additionally, the powder from the evaporated suspensions of CFA1 and CFA2 was heated to 250 °C for 15 min. According to Deer et al. (1992), this temperature is sufficient to dehydrate gypsum and form anhydrite, i.e., remove embedded water from the crystal structure. $f_{\mathrm{ice}}(-35\ ^{\circ}\mathrm{C})$ of 300 nm particles slightly increased by a factor of 2 after the heat treatment, but it did not restore the immersion freezing efficiency of the original dry-dispersed particles. It is known that other hydrated species are present in the suspension particles that are only dehydrating at much higher temperatures (e.g., dehydration temperature of portlandite: 510 °C; Bai et al., 1994) and hence it is not surprising that only a small increase in f_{ice} could be achieved. Further investigations into this matter were refrained from because of the high time expenditure associated with sample preparation and LACIS measurements.

At this point, I would like to revisit the comparison between measurements of dry-generated CFA with LACIS and SPIN (see Sec. 4.2.1) where good agreement was found for CFA3 and CFA4, but significantly lower values for CFA1 and CFA2 in the SPIN experiments compared to the LACIS experiments. A possible explanation for this sample-specific behavior could be that CFA1 is the sample with the highest amount of Ca, and presumably anhydrite, that will be dissolved once the particles are activated. As stated above, the LACIS measurements indicate that a nucleation time of 1.6 s is too short to cause the formation of an adsorbed layer of hydrated ions. The residence time of the particles in SPIN is higher by a factor of $\sim$6 and this could be enough time to dissolve a sufficient amount of anhydrite. The dependency of residence

time in SPIN on the thermodynamic conditions in the chamber (9.2 s at $T = -30$ °C and 8.2 s at $T = -40$ °C) could explain why the discrepancy between SPIN and LACIS is higher at higher temperatures. An increase in residence time allows for a larger number of ions to dissolve from the CFA particle surface at higher temperatures, which consequently leads to a stronger decrease of AF at higher temperatures. Following this hypothesis, CFA3 and CFA4 do not contain a sufficient amount of anhydrite to form a hydrated shell around the particles within 9.2 s.

It is beyond the scope of this thesis to examine why hydration leads to a lower immersion freezing efficiency. Hence, I only offer some possible explanations here without further discussing their likelihood. A simple explanation would be that the adsorbed layer of hydrated ions blocks the interaction of the particle surface and surrounding water molecules as suggested by Sievert et al. (2005). Consequently, freezing would not be triggered as efficiently as for the dry-generated particles, where the contact with water is too short to dissolve a sufficient amount of anhydrite. Another hypothesis describes a change in lattice parameters upon the forced hydration of mineral dust particles towards a greater mismatch with ice, causing a reduced ice nucleation efficiency (Sihvonen et al., 2014).

Summary

Based on a comparison of ALABAMA mass spectra and results from LACIS measurements with dry-generated CFA particles, where a correlation between signal intensity and f_{ice} was found for Ca- and S-containing species, anhydrite and quicklime were chosen as test substances for additional LACIS measurements. Dry-generated anhydrite and quicklime particles efficiently trigger immersion freezing and results are comparable to the CFA measurements. For CFA1, which is more efficient than pure anhydrite, other components like Pb might play a role in influencing the immersion freezing behavior. Presumably, the immersion freezing behavior of CFA3, which contains the lowest concentration of Ca and S, is more strongly affected by quartz compared to anhydrite or quicklime. Measurements with the suspension methods were then compared to measurements with the hydration products of anhydrite and quicklime, i.e., gypsum and calcite, and good agreement was found for CFA1, CFA2, and CFA4. Particles from the CFA3 suspension, the sample with the smallest reduction in the transition from dry to wet particle genera-

tion, still showed higher comparability to quartz than to gypsum or calcite. Investigations of the effect of suspension time on the immersion freezing efficiency showed qualitative agreement between CFA and anhydrite, i.e., a significant decrease in the transition from dry to wet particle generation. Furthermore, the degree of deactivation seems to increase with increasing suspension time, which could be related to the two steps of anhydrite hydration described in the literature. The first step is the formation of an adsorbed layer of hydrated ions on the particle surface within seconds. The second step is the actual formation of gypsum which happens after several hours up to days. Attempts to cause a dehydration of hydrated CFA particles by drying and heating were partially successful but a complete restoration of the original immersion freezing efficiency was not achieved. In conclusion, the presence of anhydrite and quicklime might be the reason for the efficient triggering of immersion freezing in the dry particle generation experiments. Likewise, both substances might be responsible for the deactivation observed in the suspension experiments as their hydration products gypsum and calcite have a lower immersion freezing efficiency. Samples with a comparably low concentration of anhydrite and quicklime and a high concentration of quartz (CFA3) might be less affected by hydration mechanisms but also seem to have a lower efficiency than other samples when being dry-generated.

5.3 Atmospheric implications

In view of the atmospheric relevance of the above described findings, it is important to discuss whether the observed decrease in immersion freezing efficiency of CFA associated with the transition from dry to wet particle generation would also occur in the atmosphere. Furthermore, the immersion freezing results can be connected to atmospheric size distribution measurements of emissions from coal combustion to retrieve INP concentrations.

From immersion freezing measurements with the suspension methods, it is known that particles in the bulk suspension are deactivated within ~2 min but it is not clear if this would also be observed when a single, dry particle is activated to a cloud droplet. The comparison of results from LACIS and SPIN (see Sec. 4.2.1), allows room for speculation as to whether the longer nucleation time in SPIN (~factor 6 longer than in LACIS) leads to some deactivation by the adsorption of hydrated ions on top of those particles which contain the highest concentration of water-soluble anhydrite. However,

the effect is much more pronounced in particles from the bulk suspensions. It would be necessary to increase the nucleation time further to evaluate the time needed to decrease the immersion freezing efficiency of single particles immersed in droplets to the efficiency of particles hydrated in the bulk suspension. Within the framework of this thesis, it was not possible to maintain cloud droplets with a single immersed CFA particle for longer than a few seconds before investigating immersion freezing. Hence, I can only provide a range of how efficiently CFA induces immersion freezing in the atmosphere based on the dry particle generation and suspension experiments. For CFA containing a certain amount of hydratable substances, the impact on atmospheric ice nucleation will very likely depend on the time between activation to cloud droplets and triggering of freezing. Note that concerning the potential of CFA particles to act as cloud condensation nuclei, findings by Navea et al. (2017) suggest similar activation abilities of CFA and mineral dust particles.

Figure 5.10 shows INP concentrations estimated from the here presented CFA immersion freezing measurements in combination with size distributions measured ∼80 km downstream of a coal-fired power plant (Parungo et al., 1978a). The early study by Parungo et al. (1978a) was chosen for lack of in-plume size distribution measurements at mesoscale distance leeward of a more modern power plant. The ambient size distribution was subtracted from the size distribution in the plume to only consider particles emitted from the power plant. Furthermore, it was assumed that n_s is independent of the particle size and that CFA particles are the only component in the plume triggering immersion freezing. Equation (2.18) was used to calculate $f_{ice}(T)$ for each particle size present in the plume with the help of $n_s(T)$ values from my immersion freezing experiments. In combination with the number concentration of each particle size given by Parungo et al. (1978a), this yields INP concentrations at 80 km distance of a coal-fired power plant stack. According to this approach, the INP concentration due to the emission of dry CFA particles (full pastel circles in Fig. 5.10) is 2 orders of magnitude higher than the upper boundary for typical atmospheric INP concentrations given by Petters and Wright (2015) at −35 °C. Assuming that atmospheric processing of the particles will lead to a decrease in immersion freezing efficiency, INP concentrations were also estimated using n_s from measurements with the suspension methods (open circles in Fig. 5.10). Above −30 °C, INP concentrations derived from measurements with CFA suspensions are close to or below the lower boundary given by Petters and Wright (2015), except

for CFA3, which is within the boundaries for $T > -23$ °C. Under the specific conditions in the here chosen example, this estimate suggests that particles with high concentrations of anhydrite, i.e., CFA1, CFA2, and CFA4, only become relevant for immersion freezing at $T < -30$ °C. CFA3 would already significantly contribute to atmospheric ice nucleation at a temperature as high as -10 °C, presumably because of the weaker influence of hydration with this sample. Note that the estimate depends strongly on the overall CFA particle number concentration, i.e., INP concentrations will be much higher than estimated above in an undiluted plume directly after emission. At even greater distances from the power plant, INP concentrations will be significantly lower due to dilution. Garimella (2016) estimated that CFA particles are present at cirrus level in number concentrations of ∼0.1 to 1 L^{-1}, which, assuming monodisperse 300 nm particles, would result in very low concentrations between $\sim 10^{-5}$ and 10^{-2} L^{-1} INPs active at -35 °C according to my estimation method.

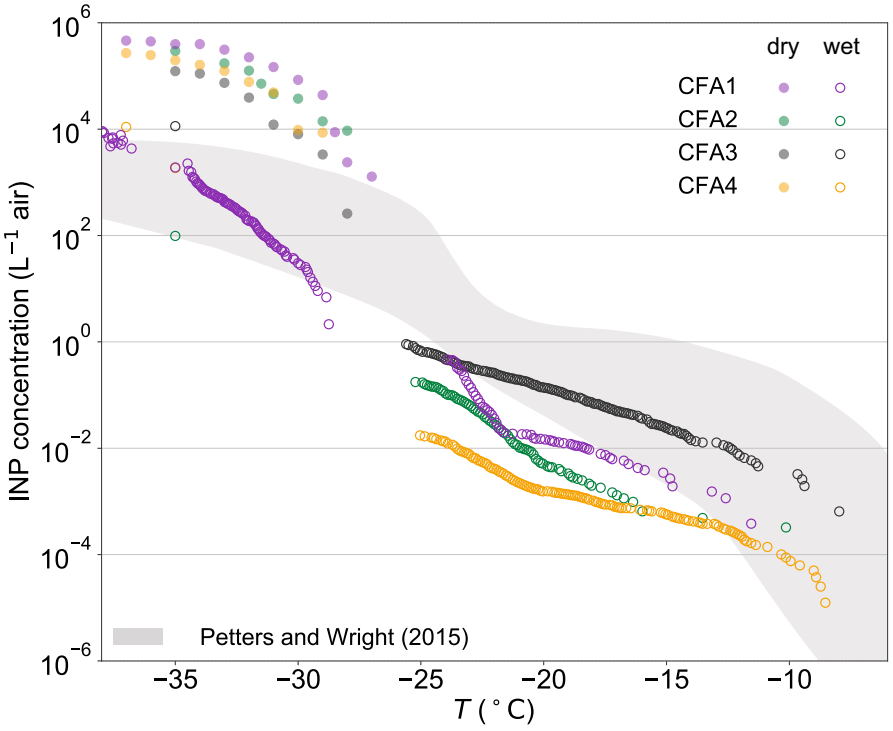

Fig. 5.10.: Estimated INP concentrations ∼80 km downstream of a coal-fired power plant based on size distributions measured in a plume by Parungo et al. (1978a). Full pastel circles represent dry-particle generation, open circles the suspension methods. The shaded area indicates typical atmospheric INP concentrations derived from precipitation samples (Petters and Wright, 2015).

6 Summary and Conclusions

In the framework of this thesis, four CFA samples from German power plants were investigated concerning their immersion freezing behavior, chemical composition, morphology, and crystallography with both single particle and bulk methods. It was shown how methodology and physicochemical particle properties can influence the immersion freezing results. In light of these new findings, I now revisit the research questions from the introduction.

- How does methodology influence CFA immersion freezing results?

All four investigated CFA samples showed a significant decrease in the immersion freezing efficiency of several orders of magnitude in the transition from dry to wet particle generation experiments with LACIS. It seems that the magnitude of the decrease is related to the suspension time of the particles in water, which is on the order of seconds in the dry particle generation experiments and on the order of minutes up to days in the wet particle generation experiments. A comparison of all suspension methods, i.e., wet particle generation with LACIS and SPIN, and the cold stage measurements with WISDOM and LINA, was only possible for CFA1, but for this sample the instrument intercomparison was successful. The comparison of dry particle generation measurements with LACIS and SPIN, whose nucleation times differ by ∼factor 6, suggests that not only particles in the bulk suspensions, but also dry-generated, individually immersed particles lose some of their immersion freezing efficiency with time. Altogether, it is important to know that for CFA, in contrast to mineral dust, it is necessary to consider dissolution effects in suspension and strong changes in immersion freezing efficiency on the time scale of seconds to minutes. Furthermore, it cannot be ruled out that the immersion freezing efficiency does not scale with the particle surface area for some CFA samples. This effect might contribute to some of the observed variability between single particle and cold stage methods in the literature.

- How do CFA samples from German power plants compare to samples from previous publications?

All four German CFA samples were found to be efficient INPs in the immersion mode below -28 °C when dry particle generation was used. The n_s spectra of dry-generated particles varied within a factor of 37 at most and steadily increased in a similar manner towards -37 °C. This variation and curve shape is in contrast to findings by Garimella (2016), the only other study in which dry-generated particles were investigated. In this study, all four CFA samples originated from the USA and showed almost identical n_s spectra with no strong temperature dependence. Samples from the identical U.S. American power plants were investigated by Losey et al. (2018) with a cold stage setup. Despite of the disagreement of the dry particle generation measurements with the German and U.S. American sample sets, the results of cold stage measurements carried out by Losey et al. (2018) and in the framework of this thesis were comparable. Data by Umo et al. (2015), who performed cold stage measurements with yet another CFA sample of unknown origin, is higher by up to 4 orders of magnitude when compared to data by Losey et al. (2018) and data from this thesis. In conclusion, there is a large variation between the reported CFA immersion freezing results, even when taking methodology into account.

- Which physicochemical particle properties influence the immersion freezing behavior of CFA?

From ALABAMA measurements it was derived that the immersion freezing efficiency of the dry-generated samples correlates with the amount of Ca and S in submicron particles. Additional LACIS measurements with anhydrite and quicklime yielded similar results as for CFA, suggesting that both substances contribute to the observed freezing behavior. Both anhydrite and quicklime are hydrated (quicklime also carbonated) in contact with water which might cause the observed decrease in immersion freezing efficiency. Cold stage measurements with the hydration products of anhydrite and quicklime, i.e., gypsum and calcite (Zolles et al., 2015), are comparable to LACIS measurements with wet-generated CFA particles and to WISDOM measurements. An exception is CFA3, which has the lowest concentration of Ca and a high concentration of Si in both 300 nm particles and bulk. Here, the decrease in immersion freezing efficiency in the transition from dry to wet particle generation is smallest, and LACIS measurements are relatively close to cold

stage measurements with quartz (Atkinson et al., 2013). Quartz was detected as the major crystalline phase in all of the bulk samples. From this, it can be concluded that an influence of quartz on the immersion freezing behavior of CFA can only be seen in case the amount of anhydrite and quicklime is below a certain, not clearly definable, threshold.

- How relevant is CFA for atmospheric immersion freezing?

From the immersion freezing investigations and literature review performed in the framework of this thesis, it has not become perfectly clear which method is representative for processes taking place after the emission of CFA particles into the atmosphere. Atmospheric droplet activation and subsequent freezing are mimicked by measurements of dry-generated particles with the single particle methods rather than by measurements with particles generated from bulk suspensions or droplets containing numerous particles. There is indication that dry-dispersed CFA particles which serve as cloud condensation nuclei become less efficient with time, but it is unknown if the efficiency would ultimately be lowered towards the values observed with the suspension methods. For estimating the contribution of CFA particles to atmospheric INP concentrations, it was assumed that this is the case, i.e., that atmospheric processing leads to a quasi-deactivation of the immersed particles. In combining information from size distribution measurements in a stable plume downstream of a coal-fired power plant (Parungo et al., 1978a) and from the here presented immersion freezing measurements, it was predicted that the majority of samples would only contribute to atmospheric immersion freezing at temperatures below -30 °C. As stated above, the immersion freezing efficiency of the CFA particles is not necessarily lowered this strongly, i.e., this result is a conservative estimate. Larger impact, i.e., higher INP concentrations at higher temperatures, can potentially be expected from class F CFA with a high concentration of quartz and low concentrations of hydratable species such as anhydrite and quicklime. In any case, the effect of CFA emission on atmospheric ice nucleation will be most pronounced in areas of high particle number concentrations, i.e., close to the source, as already indicated by the early studies about industrial snow and fog events (Benson, 1965; Agee, 1971; Parungo et al., 1978b).

7 Outlook

Estimating the large-scale atmospheric relevance of an ice-nucleating aerosol type always needs consideration of the species' efficiency, which is usually determined in laboratory ice nucleation studies, and the species' abundance in the atmosphere. In case of CFA, which is a rare example of an anthropogenic INP type, both factors remain indefinite but the present thesis could significantly contribute to our fundamental understanding of the immersion freezing behavior of CFA.

My investigations have shown that there are complex interactions between the sample characteristics and the immersion freezing behavior of CFA particles. The immersion freezing efficiency of a CFA particle may decrease drastically with increasing time between droplet activation and supercooling to a critical temperature, making the investigation of CFA particles a challenge, even under controlled conditions in laboratory settings. Future laboratory studies should focus on the effect of prolonged suspension times on the freezing behavior of single CFA particles immersed in cloud droplets. A cloud chamber, where droplets can be maintained on the time scale of minutes to hours, would be the instrument of choice for this particular research question. Furthermore, expanding the existing data set with immersion freezing measurements of additional CFA samples, also focusing on the effect of hydration and size-dependent physicochemical properties, could be worthwhile to see if new data would increase the current spread of results. The investigation of other freezing modes, especially pore condensation and freezing (Marcolli, 2014; Wagner et al., 2016), would be interesting because porous particles are known to occur in CFA. A first study concerning this matter is currently under review (Umo et al., 2019).

To date, there is a discrepancy between the number of studies investigating the freezing behavior of CFA particles on atmospheric filter samples (Schnell et al., 1976; Parungo et al., 1978a) and the number of studies performing laboratory measurements with CFA samples from ESPs (Havlíček et al., 1993; Umo et al., 2015; Garimella, 2016; Grawe et al., 2016; Grawe et al., 2018; Losey et al., 2018). At the same time, it is unresolved how representative CFA from ESPs is compared to particles that are actually emitted into the

atmosphere. Field measurements in proximity to coal-fired power plants can potentially provide an answer to this question. Future field measurements should preferably be performed within a stable plume at several locations downstream of the power plant stack and could be realized by using aircraft-based immersion freezing instrumentation or collecting filter samples for off-line analysis. Ideally, field measurements can provide information about the contribution of the plume aerosol to ambient INP concentrations and the area of influence. Together with insight about the variability of different samples from laboratory studies, these investigations can help providing a CFA ice nucleation parameterization which might be implemented into small scale simulations in the future.

Generally, estimates of the abundance of certain aerosol species in the atmosphere are available from emission inventories, satellite observations, or modeling studies. In the case of CFA, the sources, i.e., coal-fired power plants and CFA disposal sites, are well known. However, global emission estimates contain huge uncertainties because emission factors are strongly time-dependent or, as for most power plants, simply unknown. Furthermore, information from aerosol characterization studies in the field, which are abundant for almost every other aerosol species, are basically missing in the case of CFA. In fact, several mass spectrometry studies speak of indistinguishable mass spectra of mineral dust and CFA particles (Cziczo et al., 2004; Cziczo et al., 2006; Kamphus et al., 2010). Studies combining chemical composition and morphology analysis as performed by DeMott et al. (2003); Weinbruch et al. (2010); Weinbruch et al. (2012); Eriksen Hammer et al. (2018) neglect the occurrence of irregularly shaped CFA particles, which have been detected in many studies including this thesis. Hence, it is possible that part of the atmospheric ice nucleation attributed to mineral dust was indeed caused by CFA. Developing a reliable methodology for the identification of CFA particles in the atmosphere will be a challenging, maybe unresolvable, task for future investigators.

As a closing remark, a desirable objective for the future is a prompt fossil-fuel phase-out which would make the topic of CFA emission and the effect of CFA particles on atmospheric processes and human health obsolete.

Appendices

Instrumentation

A

A.1 Electrostatic precipitator

Electrostatic precipitators (ESPs) work on the principle of charging the particles and subsequently sending the flow through an electric field. Particles then migrate to the oppositely charged electrode and particulate matter is removed from the flue gas (Flagan and Seinfeld, 1988b). The ESP itself does not alter particle properties like morphology or chemical composition; only number and mass size distribution are changed (Yi et al., 2006). However, it has been argued that particles which are not captured, potentially contain a larger amount of species condensing from the gas phase onto the CFA surface upon cooling (Parungo et al., 1978a). Physicochemical particle properties can also be influenced depending on the location of the ESP with respect to the flue gas desulfurization (FGD) system.

The collection efficiency of an ESP is largely determined by the efficiency of particle charging. There are two particle charging mechanisms, field charging and diffusion charging. Field charging occurs in case ions move towards the oppositely charged electrode and get attached to particles on their way. In contrast, diffusion charging occurs not by a defined motion of the ions but rather by random thermal motion which leads ion-particle collisions (Flagan and Seinfeld, 1988b). The two mechanisms are most efficient for non-overlapping particle size regimes. According to Seinfeld et al. (2006), field charging efficiently removes particles larger than $\sim$2 μm whereas diffusion charging efficiently removes particles smaller than $\sim$0.2 μm. Hence, the collection efficiency of an ESP is expected to be minimal between 0.2 and 2 μm.

A.2 ALABAMA

ALABAMA is a single particle laser ablation instrument using a Z-shaped time-of-flight mass spectrometer. After entering the instrument, aerosol particles are focused to a narrow particle beam by an aerodynamic lens into the vacuum chamber (see Fig. A.1). The latter is separated into two pumping stages which are evacuated with the help of turbomolecular pumps. When entering the second pumping stage, the particles pass a skimmer and arrive at two subsequent detection lasers (wavelength of 405 nm) which are arranged orthogonally to each other. Scattering signals are focused onto photomultiplier tubes with the help of elliptical mirrors. Information about the time-of-flight between the detection lasers is needed to trigger the ablation laser. In addition, the time-of-flight can be used to calculate the particle vacuum aerodynamic diameter for particles in a size range between ∼200 and 2500 nm. The ablation laser, a neodymium-doped yttrium aluminum garnet (Nd:YAG) operating at a wavelength of 266 nm, evaporates the particles and ionizes the molecule fragments which are then extracted into the the flight tubes of the mass spectrometer. The ions are reflected by reflectrons and detected by multichannel plates. The result is a bipolar mass spectrum, i.e., one anion and one cation spectrum, for each single particle.

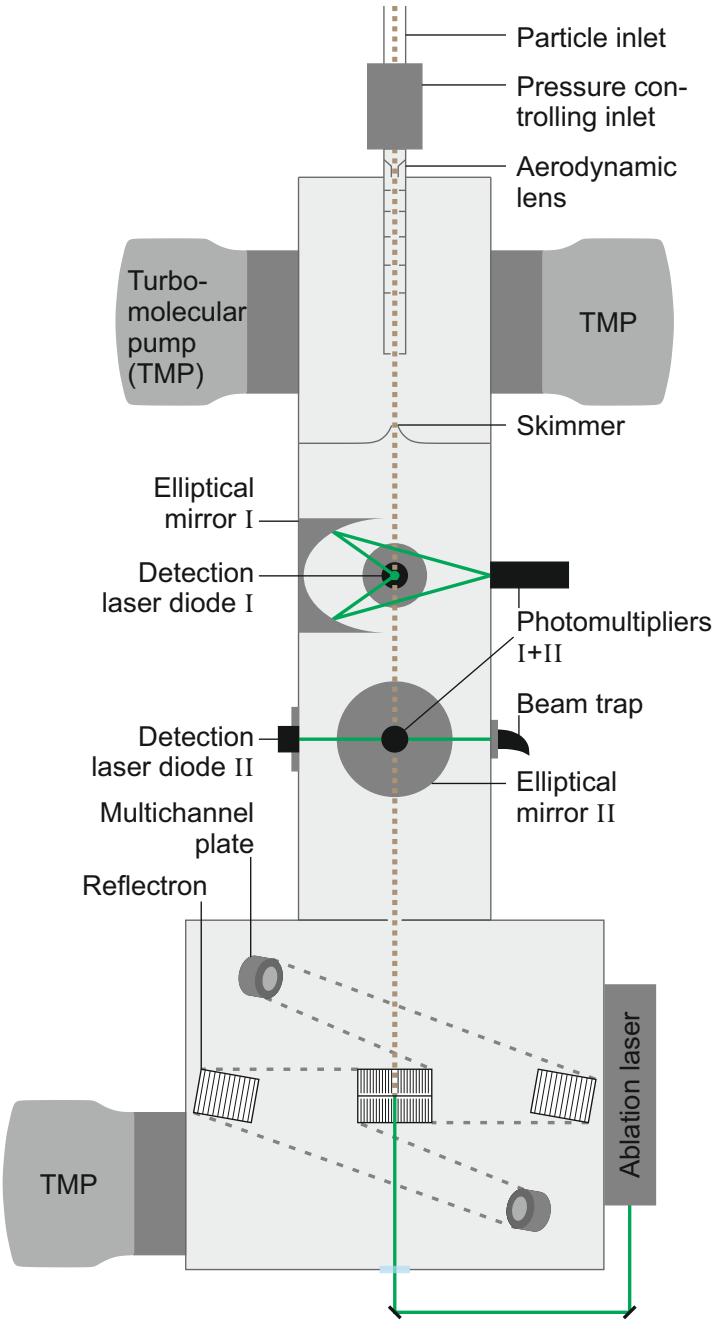

Fig. A.1.: Setup of the ALABAMA vacuum chamber with aerodynamic lens, detection and sizing region, and mass spectrometer. The two detection lasers are arranged orthogonally and shown in front and side view, respectively. Adapted from Brands et al. (2011).

A.3 Multi-MINI

The Multi-MINI is a closed impaction system for subsequent sampling onto several substrates without opening the housing. Figure A.2 a shows the design of a single impactor unit with one jet and the sample holder which carries a highly polished boron substrate. Twelve of these units are placed into the cavities of the Multi-MINI (see Fig. A.2 b). The aerosol is transported to the impactor units with the help of a 12-fold distributor. Sampling onto the individual substrates is realized with a set of valves. The Multi-MINI is equipped with a purging system which is used to fill the tubing and housing with particle-free, dry air prior to sampling.

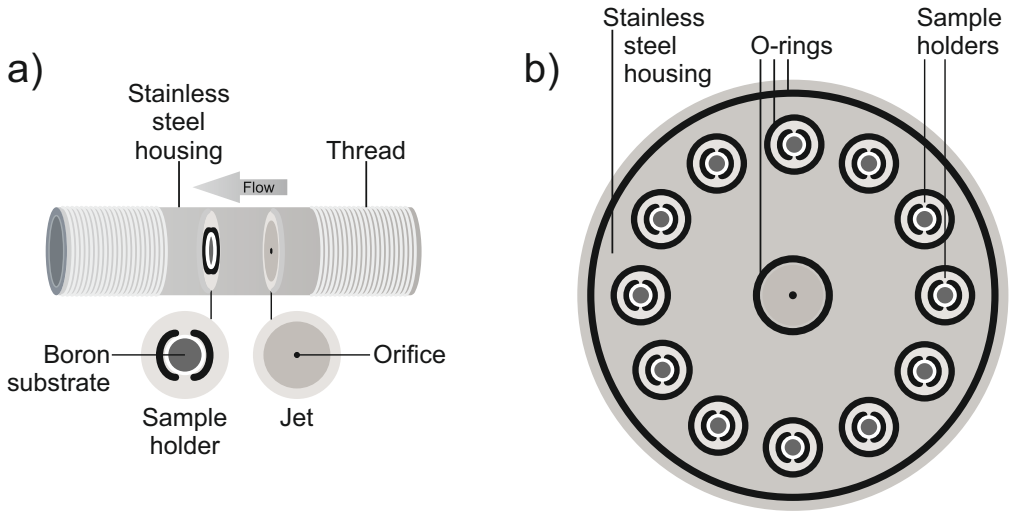

Fig. A.2.: a) Single impactor unit with one jet. b) Top view of the open Multi-MINI housing with cavities for 12 impactor units. Adapted from Ebert et al. (2016).

B Methods

B.1 Multiple charge correction

Multiply-charged fractions were determined from ALABAMA size distribution measurements of the quasi-monodisperse aerosol (see Fig. B.1). The black line represents the result of a least-squares fit assuming a four-modal normal distribution. The multiply-charged fractions were determined by dividing the number of counts in the separate modes by the total number of counts. The multiple charge correction of the measured f_{ice} values was performed according to Hartmann et al. (2016) and Burkert-Kohn et al. (2017).

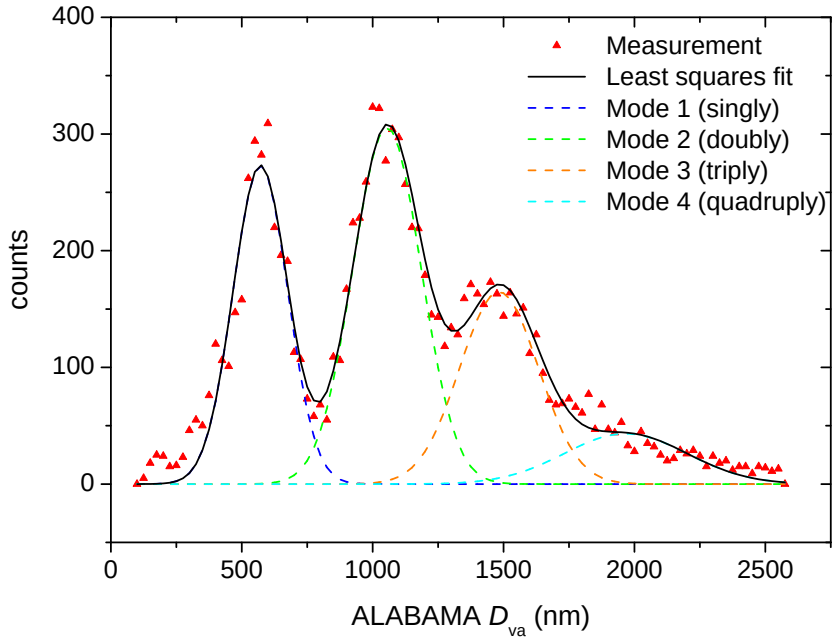

Fig. B.1.: Average size distribution of dry-generated CFA3 particles measured with ALABAMA. D_{va} is the vacuum aerodynamic diameter.

Note that multiply-charged fractions differ substantially for the different samples and particle generation methods, and, in case of dry particle generation, also increase with duration of the experiment. On the one hand, this increase is caused by a decreasing efficiency of the cyclone due to accumulated mate-

rial within. On the other hand, there is a temporal shift in size distribution of particles in the reservoir of the aerosol generator. Hence, multiply-charged fractions of dry-generated CFA were determined specifically for those points in time when LACIS measurements took place. The multiply-charged fractions given in Table B.1 are averaged values for a time frame starting ∼1 h after particle generation was turned on and lasting ∼20 min, which is when most LACIS measurements took place. LACIS data acquired at an earlier point in time were corrected with the respective multiply-charged fractions (not shown).

Table B.1.: Average multiply-charged fractions as determined from ALABAMA size distribution measurements. n is the number of charges on one particle, D_p is the Stokes diameter.

n	1	2	3	4	5
D_p (nm)	300	507	706	902	1097
CFA1 dry	0.81	0.19	-	-	
CFA2 dry	0.59	0.29	0.09	0.03	
CFA3 dry	0.28	0.38	0.24	0.1	
CFA4 dry	0.67	0.21	0.07	0.05	
CFA1 wet	0.59	0.33	0.05	0.03	
CFA2 wet	0.58	0.36	0.04	0.02	
CFA3 wet	0.34	0.40	0.09	0.09	0.08
CFA4 wet	0.6	0.29	0.06	0.05	

B.2 LINA calibration routine

A calibration of LINA is necessary because the temperature value given by the control unit of the Peltier element is not identical to the temperature of the glass slide and the temperature of the droplets. The calibration is realized by using LINA based on the principle of a dew point mirror. A glass slide is put on top of the oil layer on the Peltier element and the instrument is cooled down at the usual cooling rate (1 K min^{-1}). In contrast to the experiments with droplets, the housing is then purged with humidified, not with dry air. As the dew point of the humidified air needs to be adjustable depending on the temperature of the Peltier element, i.e., in a range from 0 to −25 °C, humidification is performed by mixing two air streams. Firstly, air is led through a Nafion humidifier (MH-110-12S-4, Perma Pure, Toms River, NJ, USA) which is kept at 10 °C with the help of a thermostat (C25P, HAAKE GmbH, Karlsruhe, Germany). Secondly, dry air is mixed with the

humidified air to obtain dew point values below 0 °C. The dew point of the mixed air is monitored with a dew point mirror (Dew Prime I-S2, Edge Tech, Milford, MA, USA). As the temperature of the glass slide approaches the dew point, the glass slide starts to fog due to the onset of condensation. By our definition, the real temperature of the glass slide, T_{real}, is equal to the dew point registered at the dew point mirror at the moment when the glass slide is 50 % fogged. The biased temperature of the instrument, T_{LINA}, is defined as the temperature given by the control unit at the point in time when the glass slide is 50 % fogged. T_{LINA} is obtained by employing optical detection as in the experiments and evaluating brightness differences between the first image without condensation and the following images with gradually increasing condensation. This routine results in a sigmoidal curve to which a fit is applied to determine the image and corresponding temperature of 50 % condensation. T_{LINA} is determined at eight different values of T_{real} between 0 and -25 °C (see Fig. B.2). Each of the shown data points is a result of averaging 10 measurements of T_{LINA}. Horizontal (standard deviation of the 10 T_{LINA} measurements) and vertical error bars (uncertainty of dew point mirror) are smaller than the symbol size in Fig. B.2. The LINA temperature calibration function is the linear fit through the calibration data. All LINA measurements presented in this thesis are corrected by applying the calibration function to temperature values from the control unit of the Peltier element.

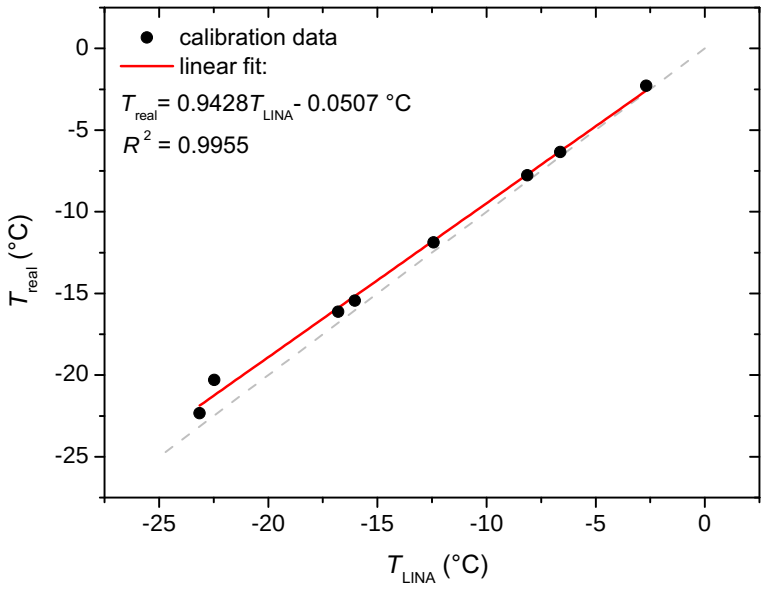

Fig. B.2.: Relation between the temperature output from the Peltier element, T_{LINA}, and the real temperature determined during calibration, T_{real}. The dashed gray line indicates the 1:1 relation.

C

LACIS Measurements with Wet-generated CFA1

The data presented in Fig. C.1 are taken from Grawe et al. (2016; similar to Fig. 4 d) and show $f_{\mathrm{ice}}(T)$ for dry- and wet-generated CFA1 particles. Measurements with dry-generated particles (full circles) are identical to those shown in Fig. 4.13 and the following. Measurements with wet-generated particles from a suspension, prepared as described by Umo et al. (2015), i.e., 10 min of ultrasonification and 24 h of stirring (open circles), suggest that CFA1 retains some activity even when being wet-generated. f_{ice} was found to be around 5 % between -24 and -35 °C, indicating no strong temperature dependence.

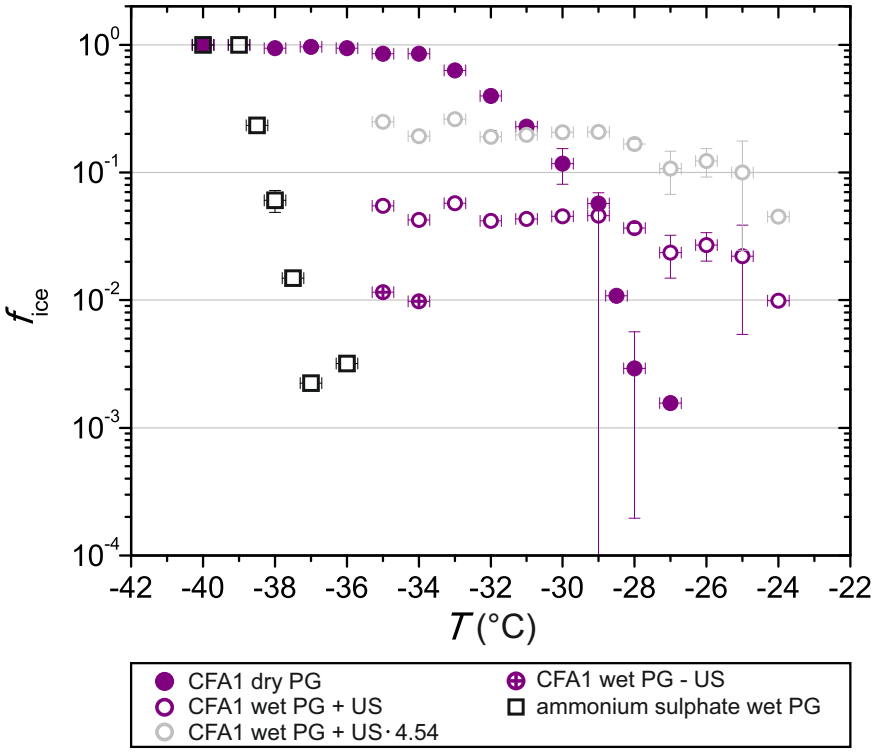

Fig. C.1.: Data taken from Fig. 4 d of Grawe et al. (2016) showing f_{ice} of dry- and wet-generated CFA1 particles (300 nm). US: ultrasonification, PG: particle generation.

At this point it was already known that needle-shaped particles are present among wet-generated CFA1 particles. However, it was assumed that the needle-shaped particles only form in the process of drying after sampling them on a substrate and that they are composed of water-soluble material which will dissolve once they are immersed in a droplet. f_{ice} would be underestimated due to the occurrence of such purely water-soluble particles, and according to this hypothesis, f_{ice} was multiplied by a scaling factor of 4.54 (=1/0.22; derived from ESEM images showing 22 % irregular and 78 % needle-shaped particles). When the suspension was prepared without ultrasonification, just stirring, lower f_{ice} values around 1 % at -35 °C were observed. These values were only slightly higher than the results of measurements with highly diluted ammonium sulphate droplets, where freezing was induced by homogeneous nucleation.

Optical microscope images of liquid suspension droplets taken in the framework of this thesis (see Fig. 4.6 a) show that the needle-shaped particles are in fact present in the aqueous environment, disproving the earlier hypothesis of purely water-soluble needle-shaped particles. As stated earlier, the ESEM images (see Fig. 4.4 and 4.5) show needle-shaped particles which are much longer than the selected 300 nm, even though the substrates were loaded after size selection. This is due to the fact that the dynamic shape factor of the needle-shaped particles differs significantly from unity. The images suggest that some of the needle-shaped particles are even longer than the usual droplet diameter at the LACIS outlet, which is 5 µm. This represents a challenge for the optical detection, because the determination of f_{ice} is based on depolarization and hence largely on the shape of the hydrometeors (Clauß et al., 2013). In usual LACIS immersion freezing experiments with 300 nm particles, the supercooled liquid droplets are spherical because a sufficient amount of water vapor is provided to form a thick (with respect to the particle diameter) layer of liquid water on top of the particles upon activation. However, if we imagine an experiment with particles from the CFA1 suspension, the long needle-shaped particles have a much larger surface area that will be covered by water molecules when exposed to the same supersaturation with respect to liquid water. As a result, a much thinner water layer is formed which will not be able to "hide" the irregular particle shape. Apparently, there is a fraction of needle-shaped particles ($\sim$5 %) which are longer than 5 µm causing droplets being non-spherical, yet unfrozen. Consequently, depolarization signals, which are associated with ice particles, are produced. This artifact can also be observed at $T > 0$ °C, demonstrating that

signals caused by the long needle-shaped particles were falsely interpreted as ice particles in Grawe et al. (2016).

To determine the realistic freezing potential of wet-generated CFA1 particles, the suspension was put through a filter (4 to 7 μm particle retention, grade 595, Whatman International Ltd., Maidstone, UK) prior to wet particle generation in order to remove large needle-shaped particles. Consequently, experiments could be conducted with 5 μm sized droplets, which were then spherical when unfrozen. f_{ice} was found to be below 0.1 % at −35 °C, i.e., the wet-generated CFA1 particles are ∼3 orders of magnitude less efficient than the dry-generated ones. This deactivation is in line with the LACIS results of the other CFA samples. At this point, it shall be mentioned again that CFA1 is the only sample for which this measurement artifact was observed. Hence, there was no need to perform experiments with filtered suspensions of CFA2, CFA3, and CFA4.

Concerning the lower f_{ice} values for particles from the CFA1 suspension without ultrasonification from Grawe et al. (2016), it can be hypothesized that, due to the lack of agitation, less of the material responsible for the formation of needle-shaped particles was dissolved from the CFA particles. Consequently, less and/or shorter needle-shaped particles might have formed which would not disturb the spherical shape of the droplets and the optical detection.

List of Abbreviations

ALABAMA	Aircraft-based Laser ABlation Aerosol MAss spectrometer
ASTM	American Society for Testing and Materials
BET	Brunauer Emmett Teller N_2 gas adsorption
BINARY	Bielefeld Ice Nucleation ARraY
CFA	Coal fly ash
CPC	Condensation particle counter
DMA	Differential mobility analyzer
DMPS	Differential mobility particle sizer
EDX	Energy dispersive X-ray spectroscopy
ESEM	Environmental scanning electron microscopy
ESP	Electrostatic precipitator
FGD	Flue gas desulfurization
ICP-SFMS	Inductively coupled plasma–sector field mass spectrometry
INP	Ice-nucleating particle
INUIT	Ice Nuclei research UnIT
IPCC	Intergovernmental Panel on Climate Change
KFA	Kohle-Flugasche
LACIS	Leipzig Aerosol Cloud Interaction Simulator
LINA	Leipzig Ice Nucleation Array
LOI	Loss on ignition
MCC	Multiple charge correction
MINI	Micro INertial Impactor
Nd:YAG	Neodymium-doped yttrium aluminum garnet
NIPI	Nucleation by Immersed Particle Instrument
OPC	Optical particle counter
PDMS	Polydimethylsiloxane
PG	Particle generation

SPIN	SPectrometer for Ice Nuclei
TMP	Turbomolecular pump
TOPS-Ice	Thermo-stabilized Optical Particle Spectrometer for the detection of Ice
TROPOS	Leibniz Institute for Tropospheric Research
US	Ultrasonification
WISDOM	WeIzmann Supercooled Droplets Observation on Microarray
XRD	X-ray diffraction analysis

List of Symbols

A_{BET}	(m^2 g^{-1})	Brunauer-Emmett-Teller specific surface area
A_{n}	(m^2)	INP surface area
AF		Activated fraction
C	(g L^{-1})	Mass concentration in suspension
D_{p}	(nm)	Stokes diameter
D_{va}	(nm)	Vacuum aerodynamic diameter
D_{50}	(nm)	Cut-off diameter
ΔF	(J)	Activation energy for diffusion across liquid-solid interface
f_{ice}		Frozen fraction
$f_{\mathrm{ice,CFA}}$		Frozen fraction of a population of CFA suspension droplets
$f_{\mathrm{ice,H_2O}}$		Frozen fraction of a population of water droplets
$f(\theta)$		Reduction factor
ΔG	(J)	Gibbs free energy change
ΔG_{het}	(J)	Gibbs free energy change for heterogeneous nucleation
$\Delta G^*_{\mathrm{het}}$	(J)	Critical Gibbs free energy change for heterogeneous nucleation
ΔG_{hom}	(J)	Gibbs free energy change for homogeneous nucleation
$\Delta G^*_{\mathrm{hom}}$	(J)	Critical Gibbs free energy change for homogeneous nucleation
ΔG_{S}	(J)	Gibbs free energy change due to surface formation
ΔG_{V}	(J)	Gibbs free energy change due to volume formation
h	(J s)	Planck's constant
j_{het}	(m^{-2} s^{-1})	Heterogeneous nucleation rate coefficient
j_{hom}	(m^{-3} s^{-1})	Homogeneous nucleation rate coefficient

K_{CFA}	(L^{-1})	Cumulative surface site concentration in CFA suspension
$K_{\mathrm{H_2O}}$	(L^{-1})	Cumulative surface site concentration in water
k	($\mathrm{m}^{-2}\ {}^{\circ}\mathrm{C}^{-1}$)	Differential surface site concentration
k_{B}	($\mathrm{J\ K}^{-1}$)	Boltzmann constant
m	(kg)	Molecular mass of ice
μ	(nm)	Mean value of normal distribution
N		Total number of droplets in population
N_{f}		Number of frozen droplets in population
N_{u}		Number of unfrozen droplets in population
n		Number of elementary charges
n^*	(m^{-3})	Equilibrium number of critical clusters in liquid phase
n_{il}	(m^{-2})	Number density of water molecules at the liquid-solid interface
n_{l}	(m^{-3})	Number density of water molecules in the liquid phase
n_{m}	(g^{-1})	Number of ice nucleation active sites per unit mass
n_{s}	(cm^{-2})	Ice nucleation active surface site density
$n_{\mathrm{s,corr}}$	(cm^{-2})	Ice nucleation active surface site density after water background correction
ν	(m^3)	Molecular volume of ice
p_{i}	(hPa)	Saturation vapor pressure over ice
p_{l}	(hPa)	Saturation vapor pressure over liquid water
r	(m)	Radius of molecular cluster
r^*	(m)	Critical radius of molecular cluster
R^2		Coefficient of determination
ρ	($\mathrm{kg\ m}^{-3}$)	Density of ice
S		Ratio of saturation vapor pressures
S_{i}		Saturation ratio with respect to ice
S_{l}		Saturation ratio with respect to liquid water
σ_{il}	($\mathrm{N\ m}^{-1}$)	Interfacial energy between solid and liquid phase
σ_{nl}	($\mathrm{N\ m}^{-1}$)	Interfacial energy between INP surface and liquid phase
σ_{ni}	($\mathrm{N\ m}^{-1}$)	Interfacial energy between INP surface and solid phase
T	(°C)	Temperature
T_0	(°C)	Temperature at start
T_{c}	(°C)	Critical temperature

T_{LINA}	(°C)	Temperature of Peltier element
T_{min}	(°C)	Minimum temperature
T_{real}	(°C)	Temperature of glass slide
t	(s)	Time
t_{c}	(s)	Characteristic ice nucleation time
θ	(°)	Contact angle
V_{d}	(m^3)	Droplet volume
$w^{\downarrow}$	(s^{-1})	Diffusive flux of water molecules across liquid-solid interface

List of Figures

2.1 Gibbs free energy change as a function of cluster radius. Surrounding droplets depict different situations during the cooling process. . . . 8
2.2 Scanning electron microscope images of CFA particles from a Bulgarian power plant. . . . 19
2.3 Overview of $n_s(T)$ from previous immersion freezing measurements with CFA samples of different origin. . . . 24

3.1 Photographs of the four CFA samples as received from the power plants. . . . 26
3.2 Experimental setup during the INUIT campaign in November 2016. . . . 27
3.3 Setup of the SPIN ice nucleation chamber and evaporation section. . . . 33
3.4 Setup of the LINA cold stage and example images. . . . 35
3.5 $n_s(T)$ from LINA measurements with uncertainties from error propagation. . . . 36
3.6 Setup of the WISDOM cold stage. . . . 38

4.1 Averaged mass spectra of quasi-monodisperse (300 nm), dry-generated CFA particles. . . . 44
4.2 Relative abundance of species in quasi-monodisperse (300 nm), dry-generated CFA particles. . . . 45
4.3 ALABAMA signal ratio of quasi-monodisperse (300 nm) wet- vs. dry-generated CFA particles. . . . 47
4.4 ESEM images of quasi-monodisperse (300 nm) CFA particles sampled with the Multi-MINI. . . . 49
4.5 ESEM image of quasi-monodisperse (300 nm) CFA1 particles from wet particle generation. . . . 50
4.6 Optical microscope images of CFA suspension droplets. . . . 53
4.7 XRD patterns of a) dry CFA1 and b) CFA1 after suspension and evaporation. . . . 56

4.8 XRD patterns of a) dry CFA2 and b) CFA2 after suspension and evaporation. 57
4.9 XRD patterns of a) dry CFA3 and b) CFA3 after suspension and evaporation. 58
4.10 XRD patterns of a) dry CFA4 and b) CFA4 after suspension and evaporation. 59
4.11 Mass fractions of major oxides and minor elements in dry bulk CFA from ICP-SFMS measurements. 61
4.12 Size distributions from DMPS measurements with wet-generated CFA particles. 64
4.13 $n_s(T)$ from LACIS measurements with dry-generated 300 nm particles. 66
4.14 Comparison of dry particle generation measurements with SPIN and LACIS (300 nm particles). 67
4.15 $n_s(T)$ from immersion freezing measurements with the suspension methods. 68

5.1 $n_m(-15\ °C)$ values from cold stage measurements with CFA by Havlíček et al. (1993) and from this thesis. 74
5.2 $n_s(T)$ from SPIN measurements with dry-generated 300 nm CFA particles from this thesis and Garimella (2016). 75
5.3 Summary of immersion freezing $n_s(T)$ data from this thesis and the literature. 77
5.4 Comparison of $f_{ice}(T)$ values from LINA and µL-NIPI measurements with a wood bottom ash sample. 78
5.5 Averaged mass spectra of species for which the ALABAMA signal intensity correlates/anti-correlates with the immersion freezing efficiency of dry-generated CFA. 81
5.6 $n_s(T)$ from LACIS measurements with dry-generated CFA, anhydrite and quicklime particles. 83
5.7 Comparison of $n_s(T)$ from suspension measurements with CFA and cold stage measurements with gypsum, calcite, and quartz (Atkinson et al., 2013; Zolles et al., 2015). 85
5.8 Two-step hydration mechanism of pure anhydrite particles in water. 86
5.9 f_{ice}(300 nm, $-35\ °C$) from LACIS measurements with differently treated samples. 88

5.10 Estimated INP concentrations ∼80 km downstream of a coal-fired power plant based on size distributions measured in a plume by Parungo et al. (1978a). 94

A.1 Setup of the ALABAMA vacuum chamber with aerodynamic lens, detection and sizing region, and mass spectrometer. . . 105
A.2 Setup of a single impactor unit and the Multi-MINI. 106

B.1 Average size distribution of dry-generated CFA3 particles measured with ALABAMA. 107
B.2 Relation between the temperature output from the Peltier element and the real temperature determined during the calibration of LINA. 109

C.1 Data taken from Fig. 4 d of Grawe et al. (2016) showing f_{ice} of dry- and wet-generated CFA1 particles (300 nm). 111

List of Tables

3.1 Overview of CFA samples with respect to performed immersion freezing and particle characterization measurements 28

4.1 Chemical composition of CFA particles from dry and wet particle generation as determined by EDX measurements. 51
4.2 Identified crystalline phases from XRD measurements of dry CFA and CFA after suspension and evaporation. 55
4.3 BET specific surface area of bulk and fine CFA. 62
4.4 Mean values μ of the bi-modal normal distribution fits to size distributions of wet-generated CFA particles. 64

B.1 Average multiply-charged fractions as determined from ALABAMA size distribution measurements. 108

References

Abbatt, J. P. D. (2003). “Interactions of atmospheric trace gases with ice surfaces: Adsorption and reaction”. In: *Chemical Reviews* 103.12, pp. 4783–4800.

Agee, E. M. (1971). “An artificially induced local snowfall”. In: *Bulletin of the American Meteorological Society* 52.7, pp. 557–560.

Ahmaruzzaman, M. (2010). “A review on the utilization of fly ash”. In: *Progress in Energy and Combustion Science* 36.3, pp. 327–363.

Alstadt, V. J., J. N. Dawson, D. J. Losey, S. K. Sihvonen, and M. A. Freedman (2017). “Heterogeneous Freezing of Carbon Nanotubes: A Model System for Pore Condensation and Freezing in the Atmosphere”. In: *The Journal of Physical Chemistry A* 121.42, pp. 8166–8175.

Ansmann, A., M. Tesche, D. Althausen, D. Müller, P. Seifert, V. Freudenthaler, B. Heese, M. Wiegner, G. Pisani, P. Knippertz, and O. Dubovik (2008). “Influence of Saharan dust on cloud glaciation in southern Morocco during the Saharan Mineral Dust Experiment”. In: *Journal of Geophysical Research: Atmospheres* 113.D04210. DOI: 10.1029/2007JD008785.

ASTM (2017). *Standard Specification for Coal Fly Ash and Raw or Calcined Natural Pozzolan for Use in Concrete*. Technical Report C618 - 17a. American Society for Testing and Materials (ASTM).

Atkinson, J. D., B. J. Murray, M. T. Woodhouse, T. F. Whale, K. J. Baustian, K. S. Carslaw, S. Dobbie, D. O’Sullivan, and T. L. Malkin (2013). “The importance of feldspar for ice nucleation by mineral dust in mixed-phase clouds”. In: *Nature* 498, pp. 355–358.

Augustin-Bauditz, S., H. Wex, S. Kanter, M. Ebert, D. Niedermeier, F. Stolz, A. Prager, and F. Stratmann (2014). “The immersion mode ice nucleation behavior of mineral dusts: A comparison of different pure and surface modified dusts”. In: *Geophysical Research Letters* 41.20, pp. 7375–7382.

Bai, T. B., A. F. Koster van Groos, and S. Guggenheim (1994). "Phase transition, dehydration, and melting relationships of portlandite". In: *American Mineralogist* 79.11, pp. 1223–1226.

Bauerecker, S., P. Ulbig, V. Buch, L. Vrbka, and P. Jungwirth (2008). "Monitoring ice nucleation in pure and salty water via high-speed imaging and computer simulations". In: *The Journal of Physical Chemistry C* 112.20, pp. 7631–7636.

Benson, C. (1965). *Ice fog: Low temperature air pollution*. Research Report 121. U.S. Army Cold Regions Research and Engineering Laboratory (CRREL).

Bigg, E. K. (1953a). "The formation of atmospheric ice crystals by the freezing of droplets". In: *Quarterly Journal of the Royal Meteorological Society* 79.342, pp. 510–519.

– (1953b). "The supercooling of water". In: *Proceedings of the Physical Society, Section B* 66.8, pp. 688–694.

Block, C. and R. Dams (1976). "Study of fly ash emission during combustion of coal". In: *Environmental Science and Technology* 10.10, pp. 1011–1017.

Boer, G. de, H. Morrison, and M. D. Shupe (2011). "Evidence of liquid dependent ice nucleation in high-latitude stratiform clouds from surface remote sensors". In: *Geophysical Research Letters* 38.1. DOI: 10.1029/2010GL046016.

Boose, Y., A. Welti, J. Atkinson, F. Ramelli, A. Danielczok, H. G. Bingemer, M. Plötze, B. Sierau, Z. A. Kanji, and U. Lohmann (2016a). "Heterogeneous ice nucleation on dust particles sourced from nine deserts worldwide – Part 1: Immersion freezing". In: *Atmospheric Chemistry and Physics* 16, pp. 15075–15095.

Boose, Y., Z. A. Kanji, M. Kohn, B. Sierau, A. Zipori, I. Crawford, G. Lloyd, N. Bukowiecki, E. Herrmann, P. Kupiszewski, M. Steinbacher, and U. Lohmann (2016b). "Ice nucleating particle measurements at 241 K during winter months at 3580 m MSL in the Swiss Alps". In: *Journal of the Atmospheric Sciences* 73.5, pp. 2203–2228.

Boucher, O., D. Randall, P. Artaxo, C. Bretherton, G. Feingold, P. Forster, V.-M. Kerminen, Y. Kondo, H. Liao, U. Lohmann, P. Rasch, S. K. Satheesh, S. Sherwood, B. Stevens, and X. Y. Zhan (2013). "Clouds and Aerosols". In: *Climate Change 2013: The Physical Science Basis. Contribution of Working Group I to the Fifth Assessment Report of the Intergovernmental Panel on Climate Change*. Ed. by T.F. Stocker, D. Qin, G.-K. Plattner, M. Tignor, S. K. Allen, J. Boschung, A. Nauels, Y. Xia, V. Bex, and P. M. Midgley. Cambridge University Press, Cambridge, UK and New York, NY, USA.

Bradski, G. and A. Kaehler (2008). *Learning OpenCV: Computer vision with the OpenCV library*. O'Reilly & Associates, Sebastopol, CA, USA.

Brands, M., M. Kamphus, T. Böttger, J. Schneider, F. Drewnick, A. Roth, J. Curtius, C. Voigt, A. Borbon, M. Beekmann, A. Bourdon, T. Perrin, and S. Borrmann (2011). "Characterization of a newly developed aircraft-based laser ablation aerosol mass spectrometer (ALABAMA) and first field deployment in urban pollution plumes over Paris during MEGAPOLI 2009". In: *Aerosol Science and Technology* 45.1, pp. 46–64.

Broadley, S. L., B. J. Murray, R. J. Herbert, J. D. Atkinson, S. Dobbie, T. L. Malkin, E. Condliffe, and L. Neve (2012). "Immersion mode heterogeneous ice nucleation by an illite rich powder representative of atmospheric mineral dust". In: *Atmospheric Chemistry and Physics* 12.1, pp. 287–307.

Brunauer, S., P. H. Emmett, and E. Teller (1938). "Adsorption of gases in multimolecular layers". In: *Journal of the American Chemical Society* 60.2, pp. 309–319.

Budke, C. and T. Koop (2015). "BINARY: An optical freezing array for assessing temperature and time dependence of heterogeneous ice nucleation". In: *Atmospheric Measurement Techniques* 8, pp. 689–703.

Burkert-Kohn, M., H. Wex, A. Welti, S. Hartmann, S. Grawe, L. Hellner, P. Herenz, J. D. Atkinson, F. Stratmann, and Z. A. Kanji (2017). "Leipzig Ice Nucleation chamber Comparison (LINC): Inter-comparison of four online ice nucleation counters". In: *Atmospheric Chemistry and Physics* 17, pp. 11683–11705.

Canpolat, F., K. Yılmaz, M. M. Köse, M. Sümer, and M. A. Yurdusev (2004). "Use of zeolite, coal bottom ash and fly ash as replacement materials in cement production". In: *Cement and Concrete Research* 34, pp. 731–735.

Carte, A. E. (1956). "The freezing of water droplets". In: *Proceedings of the Physical Society, Section B* 69.10, pp. 1028–1037.

Chakraborty, S., R. Fu, S. T. Massie, and G. Stephens (2016). "Relative influence of meteorological conditions and aerosols on the lifetime of mesoscale convective systems". In: *Proceedings of the National Academy of Sciences* 113.27, pp. 7426–7431.

Chen, J., Z. Wu, S. Augustin-Bauditz, S. Grawe, M. Hartmann, X. Pei, Z. Liu, D. Ji, and H. Wex (2018). "Ice-nucleating particle concentrations unaffected by urban air pollution in Beijing, China". In: *Atmospheric Chemistry and Physics* 18, pp. 3523–3539.

Clauß, T., A. Kiselev, S. Hartmann, S. Augustin, S. Pfeifer, D. Niedermeier, H. Wex, and F. Stratmann (2013). "Application of linear polarized light for the

discrimination of frozen and liquid droplets in ice nucleation experiments". In: *Atmospheric Measurement Techniques* 6, pp. 1041–1052.

Connolly, P. J., O. Möhler, P. R. Field, H. Saathoff, R. Burgess, T. Choularton, and M. Gallagher (2009). "Studies of heterogeneous freezing by three different desert dust samples". In: *Atmospheric Chemistry and Physics* 9, pp. 2805–2824.

Cziczo, D., O. Stetzer, A. Worringen, M. Ebert, S. Weinbruch, M. Kamphus, S. J. Gallavardin, J. Curtius, S. Borrmann, K. D. Froyd, S. Mertes, O. Möhler, and U. Lohmann (2009). "Inadvertent climate modification due to anthropogenic lead". In: *Nature Geoscience* 2, pp. 333–336.

Cziczo, D. J., D. M. Murphy, P. K. Hudson, and D. S. Thomson (2004). "Single particle measurements of the chemical composition of cirrus ice residue during CRYSTAL-FACE". In: *Journal of Geophysical Research* 109.D04201. DOI: 10.1029/2003JD004032.

Cziczo, D. J., D. S. Thomson, T. L. Thompson, P. J. DeMott, and D. M. Murphy (2006). "Particle analysis by laser mass spectrometry (PALMS) studies of ice nuclei and other low number density particles". In: *International Journal of Mass Spectrometry* 258.1, pp. 21–29.

Damle, A. S., D. S. Ensor, and M. B. Ranade (1982). "Coal combustion mechanisms: A review". In: *Aerosol Science and Technology* 1, pp. 119–133.

Davison, R. L., D. F. S. Natusch, J. R. Wallace, and C. A. Evans Jr. (1974). "Trace elements in fly ash: dependence of concentration on particle size". In: *Environmental Science & Technology* 8.13, pp. 1107–1113.

Deer, W. A., R. A. Howie, and J. Zussman (1992). *An Introduction to the Rock Forming Minerals*. 2nd ed. Longman Scientific and Technical, Essex, UK.

DeMott, P. J. (2002). "Laboratory studies of cirrus cloud processes". In: *Cirrus*. Oxford University Press, Oxford, UK, pp. 102–135.

DeMott, P. J., D. J. Cziczo, A. J. Prenni, D. M. Murphy, S. M. Kreidenweis, D. S. Thomson, R. Borys, and D. C. Rogers (2003). "Measurements of the concentration and composition of nuclei for cirrus formation". In: *Proceedings of the National Academy of Sciences* 100.25, pp. 14655–14660.

DeMott, P. J., A. J. Prenni, G. R. McMeeking, R. C. Sullivan, M. D. Petters, Y. Tobo, M. Niemand, O. Möhler, J. R. Snider, Z. Wang, and S. M. Kreidenweis (2015). "Integrating laboratory and field data to quantify the immersion freezing ice nucleation activity of mineral dust particles". In: *Atmospheric Chemistry and Physics* 15.1, pp. 393–409.

DeMott, P. J., T. C. J. Hill, C. S. McCluskey, K. A. Prather, D. B. Collins, R. C. Sullivan, M. J. Ruppel, R. H. Mason, V. E. Irish, T. Lee, C. Y. Hwang, T. S. Rhee, J. R. Snider, G. R. McMeeking, S. Dhaniyala, E. R. Lewis, J.

J. B. Wentzell, J. Abbatt, C. Lee, C. M. Sultana, A. P. Ault, J. L. Axson, M. Diaz Martinez, I. Venero, G. Santos-Figueroa, M. D. Stokes, G. B. Deane, O. L. Mayol-Bracero, V. H. Grassian, T. H. Bertram, A. K. Bertram, B. F. Moffett, and G. D. Franc (2016). "Sea spray aerosol as a unique source of ice nucleating particles". In: *Proceedings of the National Academy of Sciences* 113.21, pp. 5797–5803.

DeMott, P. J., T. C. J. Hill, M. D. Petters, A. K. Bertram, Y. Tobo, R. H. Mason, K. J. Suski, C. S. McCluskey, E. J. T. Levin, G. P. Schill, Y. Boose, A. M. Rauker, A. J. Miller, J. Zaragoza, K. Rocci, N. E. Rothfuss, H. P. Taylor, J. D. Hader, C. Chou, J. A. Huffman, U. Pöschl, A. J. Prenni, and S. M. Kreidenweis (2017). "Comparative measurements of ambient atmospheric concentrations of ice nucleating particles using multiple immersion freezing methods and a continuous flow diffusion chamber". In: *Atmospheric Chemistry and Physics* 17, pp. 11227–11245.

Dreischmeier, K., C. Budke, L. Wiehemeier, T. Kottke, and T. Koop (2017). "Boreal pollen contain ice-nucleating as well as ice-binding 'antifreeze' polysaccharides". In: *Scientific Reports* 7. DOI: 10.1038/srep41890.

Dufour, L. and R. Defay (1963). *Thermodynamics of Clouds*. Academic Press, New York, NY, USA.

Durant, A. J. and R. A. Shaw (2005). "Evaporation freezing by contact nucleation inside-out". In: *Geophysical Research Letters* 32.L20814. DOI: 10.1029/2005GL024175.

Ebert, M., R. Weigel, K. Kandler, G. Günther, S. Molleker, J.-U. Grooß, B. Vogel, S. Weinbruch, and S. Borrmann (2016). "Chemical analysis of refractory stratospheric aerosol particles collected within the arctic vortex and inside polar stratospheric clouds". In: *Atmospheric Chemistry and Physics* 16, pp. 8405–8421.

Emersic, C., P. J. Connolly, S. Boult, M. Campana, and Z. Li (2015). "Investigating the discrepancy between wet-suspension- and dry dispersion-derived ice nucleation efficiency of mineral particles". In: *Atmospheric Chemistry and Physics* 15, pp. 11311–11326.

endcoal.org (2018). *Coal plants by country (Units) - July 2018*. Retrieved November 8, 2018. URL: https://endcoal.org/global-coal-plant-tracker/summary-statistics/.

Enders, M. (1996). "The CaO distribution to mineral phases in a high calcium fly ash from Eastern Germany". In: *Cement and Concrete Research* 26.2, pp. 243–251.

Ensor, D. S., S. Cowen, R. Hooper, and G. Markowski (1979). *Evaluation of the George Neal No. 3 electrostatic precipitator*. Technical Report FP-1145. Electric Power Research Institute (EPRI).

Ensor, D. S., S. Cowen, A. Shendrikar, G. Markowski, and G. Waffinden (1981). *Kramer station fabric filter evaluation*. Technical Report CS-1669. Electric Power Research Institute (EPRI).

Eriksen Hammer, S., S. Mertes, J. Schneider, M. Ebert, K. Kandler, and S. Weinbruch (2018). "Composition of ice particle residuals in mixed-phase clouds at Jungfraujoch (Switzerland): enrichment and depletion of particle groups relative to total aerosol". In: *Atmospheric Chemistry and Physics* 18, pp. 13987–14003.

Felgitsch, L., P. Baloh, J. Burkart, M. Mayr, M. E. Momken, T. M. Seifried, P. Winkler, D. G. Schmale III, and H. Grothe (2018). "Birch leaves and branches as a source of ice-nucleating macromolecules". In: *Atmospheric Chemistry and Physics* 18, pp. 16063–16079.

Field, P. R., R. P. Lawson, P. R. A. Brown, G. Lloyd, C. Westbrook, D. Moisseev, A. Miltenberger, A. Nenes, A. Blyth, T. Choularton, P. Connolly, J. Buehl, J. Crosier, Z. Cui, C. Dearden, P. DeMott, A. Flossmann, A. Heymsfield, Y. Huang, H. Kalesse, Z. A. Kanji, A. Korolev, A. Kirchgaessner, S. Lasher-Trapp, T. Leisner, G. McFarquhar, V. Phillips, J. Stith, and S. Sullivan (2017). "Secondary Ice Production: Current State of the Science and Recommendations for the Future". In: *Meteorological Monographs* 58, pp. 7.1–7.20.

Fisher, G. L., D. P. Y. Chang, and M. Brummer (1976). "Fly ash collected from electrostatic precipitators: microcrystalline structures and the mystery of the spheres". In: *Science* 192.4239, pp. 553–555.

Flagan, R. C. and S. K. Friedlander (1978). "Particle formation in pulverized coal combustion - A review". In: *Recent Developments in Aerosol Science*. Wiley, New York, NY, USA, pp. 25–59.

Flagan, R. C. and J. H. Seinfeld (1988a). "Particle Formation in Combustion". In: *Fundamentals of Air Pollution Engineering*. Prentice-Hall Inc., Englewood Cliffs, NJ, USA, pp. 358–390.

– (1988b). "Removal of Particles from Gas Streams". In: *Fundamentals of Air Pollution Engineering*. Prentice-Hall Inc., Englewood Cliffs, NJ, USA, pp. 391–478.

Flanders, P. J. (1999). "Identifying fly ash at a distance from fossil fuel power stations". In: *Environmental Science & Technology* 33.4, pp. 528–532.

Fletcher, N. H. (1959). "Entropy effect in ice crystal nucleation". In: *Journal of Chemical Physics* 30, pp. 1476–1482.

Frey, W., D. Hu, J. Dorsey, M. R. Alfarra, A. Pajunoja, A. Virtanen, P. Connolly, and G. McFiggans (2018). “The efficiency of secondary organic aerosol particles acting as ice-nucleating particles under mixed-phase cloud conditions”. In: *Atmospheric Chemistry and Physics* 18, pp. 9393–9409.

Fröhlich-Nowoisky, J., T. C. J. Hill, B. G. Pummer, P. Yordanova, G. D. Franc, and U. Pöschl (2015). “Ice nucleation activity in the widespread soil fungus Mortierella alpina”. In: *Biogeosciences* 12.4, pp. 1057–1071.

Gallavardin, S. J., U. Lohmann, and D. J. Cziczo (2008). “Analysis and differentiation of mineral dust by single particle laser mass spectrometry”. In: *International Journal of Mass Spectrometry* 274.1-3, pp. 56–63.

Garimella, S. (2016). “A vertically-integrated approach to climate science: From measurements and machine learning to models and policy”. PhD thesis. Massachusetts Institute of Technology, Cambridge, MA, USA.

Garimella, S., T. B. Kristensen, K. Ignatius, A. Welti, J. Voigtländer, G. R. Kulkarni, F. Sagan, G. L. Kok, J. Dorsey, L. Nichman, D. A. Rothenburg, M. Rösch, A. C. R. Kirchgässner, R. Ladkin, H. Wex, T. W. Wilson, L. A. Ladino, J. P. D. Abbatt, O. Stetzer, U. Lohmann, F. Stratmann, and D. J. Cziczo (2016). “The SPectrometer for Ice Nuclei (SPIN): an instrument to investigate ice nucleation”. In: *Atmospheric Measurement Techniques* 9, pp. 2781–2795.

Genareau, K., S. Cloer, K. Primm, M. Tolbert, and T. Woods (2018). “Compositional and Mineralogical Effects on Ice Nucleation Activity of Volcanic Ash”. In: *Atmosphere* 9.7. DOI: 10.3390/atmos9070238.

Gianoncelli, A., A. Zacco, R. P. W. Struis, L. Borgese, L. E. Depero, and E. Bontempi (2013). “Fly ash pollutants, treatment and recycling”. In: *Pollutant Diseases, Remediation and Recycling*. Springer International Publishing, Cham, Switzerland, pp. 103–213.

Gieré, R., L. E. Carleton, and G. R. Lumpkin (2003). “Micro-and nanochemistry of fly ash from a coal-fired power plant”. In: *American Mineralogist* 88.11-12, pp. 1853–1865.

Gladney, E. S., J. A. Small, G. E. Gordon, and W. H. Zoller (1976). “Composition and size distribution of in-stack particulate material at a coal-fired power plant”. In: *Atmospheric Environment* 10, pp. 1071–1077.

Grawe, S., S. Augustin-Bauditz, S. Hartmann, L. Hellner, J. B. C. Pettersson, A. Prager, F. Stratmann, and H. Wex (2016). “The immersion freezing behavior of ash particles from wood and brown coal burning”. In: *Atmospheric Chemistry and Physics* 16, pp. 13911–13928.

Grawe, S., S. Augustin-Bauditz, H.-C. Clemen, M. Ebert, S. Eriksen Hammer, J. Lubitz, N. Reicher, Y. Rudich, J. Schneider, R. Staacke, F. Stratmann,

A. Welti, and H. Wex (2018). “Coal fly ash: linking immersion freezing behavior and physicochemical particle properties”. In: *Atmospheric Chemistry and Physics* 18, pp. 13903–13923.

Gražulis, S., D. Chateigner, R. T. Downs, A. F. T. Yokochi, M. Quirós, L. Lutterotti, E. Manakova, J. Butkus, P. Moeck, and A. Le Bail (2009). “Crystallography Open Database - an open-access collection of crystal structures”. In: *Journal of Applied Crystallography* 42.4, pp. 726–729.

Gute, E. and J. P. D. Abbatt (2018). “Oxidative processing lowers the ice nucleation activity of birch and alder pollen”. In: *Geophysical Research Letters* 45.3, pp. 1647–1653.

Hartmann, S., D. Niedermeier, J. Voigtländer, T. Clauß, R. A. Shaw, H. Wex, A. Kiselev, and F. Stratmann (2011). “Homogeneous and heterogeneous ice nucleation at LACIS: Operating principle and theoretical studies”. In: *Atmospheric Chemistry and Physics* 11, pp. 1753–1767.

Hartmann, S., H. Wex, T. Clauß, S. Augustin-Bauditz, D. Niedermeier, M. Rösch, and F. Stratmann (2016). “Immersion freezing of kaolinite: Scaling with particle surface area”. In: *Journal of the Atmospheric Sciences* 73, pp. 263–278.

Havlíček, D., R. Přibil, and B. Kratochvíl (1989). “Content of quartz and mullite in some selected power-plant fly ash in Czechoslovakia”. In: *Atmospheric Environment* 23.3, pp. 701–706.

Havlíček, D., R. Přibil, and O. Školoud (1993). “The chemical and mineralogical composition of the water-soluble fraction of power-plant ash and its effect on the process of crystallization of water”. In: *Atmospheric Environment* 27A.5, pp. 655–660.

Herbert, R. J., B. J. Murray, T. F. Whale, S. J. Dobbie, and J. D. Atkinson (2014). “Representing time-dependent freezing behaviour in immersion mode ice nucleation”. In: *Atmospheric Chemistry and Physics* 14, pp. 8501–8520.

Herich, H., T. Tritscher, A. Wiacek, M. Gysel, E. Weingartner, U. Lohmann, U. Baltensperger, and D. J. Cziczo (2009). “Water uptake of clay and desert dust aerosol particles at sub- and supersaturated water vapor conditions”. In: *Physical Chemistry Chemical Physics* 11, pp. 7804–7809.

Hill, T. C. J., P. J. DeMott, Y. Tobo, J. Fröhlich-Nowoisky, B. F. Moffett, G. D. Franc, and S. M. Kreidenweis (2016). “Sources of organic ice nucleating particles in soils”. In: *Atmospheric Chemistry and Physics* 16, pp. 7195–7211.

Hiranuma, N., S. D. Brooks, B. W. Auvermann, and R. Littleton (2008). “Using environmental scanning electron microscopy to determine the hy-

groscopic properties of agricultural aerosols". In: *Atmospheric Environment* 42, pp. 1983–1994.

Hiranuma, N., S. Augustin-Bauditz, H. Bingemer, C. Budke, J. Curtius, A. Danielczok, K. Diehl, K. Dreischmeier, M. Ebert, F. Frank, N. Hoffmann, K. Kandler, A. Kiselev, T. Koop, T. Leisner, O. Möhler, B. Nillius, A. Peckhaus, D. Rose, S. Weinbruch, H. Wex, Y. Boose, P. J. DeMott, J. D. Hader, T. C. J. Hill, Z. A. Kanji, G. Kulkarni, E. J. T. Levin, C. S. McCluskey, M. Murakami, B. J. Murray, D. Niedermeier, M. D. Petters, D. O'Sullivan, A. Saito, G. P. Schill, T. Tajiri, M. A. Tolbert, A. Welti, T. F. Whale, T. P. Wright, and K. Yamashita (2015a). "A comprehensive laboratory study on the immersion freezing behavior of illite NX particles: A comparison of 17 ice nucleation measurement techniques". In: *Atmospheric Chemistry and Physics* 15, pp. 2489–2518.

Hiranuma, N., O. Möhler, K. Yamashita, T. Tajiri, A. Saito, A. Kiselev, N. Hoffmann, C. Hoose, E. Jantsch, T. Koop, and M. Murakami (2015b). "Ice nucleation by cellulose and its potential contribution to ice formation in clouds". In: *Nature Geoscience* 8.4, pp. 273–277.

Hoose, C. and O. Möhler (2012). "Heterogeneous ice nucleation on atmospheric aerosols: a review of results from laboratory experiments". In: *Atmospheric Chemistry and Physics* 12, pp. 9817–9854.

Houghton, H. G. (1950). "A preliminary quantitative analysis of precipitation mechanisms". In: *Journal of Meteorology* 7, pp. 363–369.

Ignatius, K., T. B. Kristensen, E. Järvinen, L. Nichman, C. Fuchs, H. Gordon, P. Herenz, C. R. Hoyle, J. Duplissy, S. Garimella, A. Dias, C. Frege, N. Höppel, J. Tröstl, R. Wagner, C. Yan, A. Amorim, U. Baltensperger, J. Curtius, N. M. Donahue, M. W. Gallagher, J. Kirkby, M. Kulmala, O. Möhler, H. Saathoff, M. Schnaiter, A. Tomé, A. Virtanen, D. Worsnop, and F. Stratmann (2016). "Heterogeneous ice nucleation of viscous secondary organic aerosol produced from ozonolysis of α-pinene". In: *Atmospheric Chemistry and Physics* 16, pp. 6495–6509.

Jaenicke, R. (1978). "Über die Dynamik atmosphärischer Aitkenteilchen". In: *Berichte der Bunsengesellschaft für physikalische Chemie* 82.11, pp. 1198–1202.

Kaakinen, J. W., R. M. Jorden, M. H. Lawasani, and R. E. West (1975). "Trace element behavior in coal-fired power plant". In: *Environmental Science and Technology* 9.9, pp. 862–869.

Kampe, H. J aufm and H. K. Weickmann (1951). "The effectiveness of natural and artificial aerosols as freezing nuclei". In: *Journal of Meteorology* 8.5, pp. 283–288.

Kamphus, M., M. Ettner-Mahl, T. Klimach, F. Drewnick, L. Keller, D. J. Cziczo, S. Mertes, S. Borrmann, and J. Curtius (2010). "Chemical composition of ambient aerosol, ice residues and cloud droplet residues in mixed-phase clouds: Single particle analysis during the Cloud and Aerosol Characterization Experiment (CLACE 6)". In: *Atmospheric Chemistry and Physics* 10, pp. 8077–8095.

Kaufmann, L., C. Marcolli, J. Hofer, V. Pinti, C. R. Hoyle, and T. Peter (2016). "Ice nucleation efficiency of natural dust samples in the immersion mode". In: *Atmospheric Chemistry and Physics* 16, pp. 11177–11206.

Kim, Y. Y., A. N. Kulak, Y. Li, T. Batten, M. Kuball, S. P. Armes, and F. C. Meldrum (2009). "Substrate-directed formation of calcium carbonate fibres". In: *Journal of Materials Chemistry* 19, pp. 387–398.

Kiselev, A., F. Bachmann, P. Pedevilla, S. J. Cox, A. Michaelides, D. Gerthsen, and T. Leisner (2017). "Active sites in heterogeneous ice nucleation–the example of K-rich feldspars". In: *Science* 355.6323, pp. 367–371.

Klimchouk, A. (1996). "The dissolution and conversion of gypsum and anhydrite". In: *International Journal of Speleology* 25.3, pp. 21–36.

Knackstedt, K., B. F. Moffett, S. Hartmann, H. Wex, T. C. J. Hill, E. Glasgo, L. Reitz, S. Augustin-Bauditz, B. Beall, G. S. Bullerjahn, J. Fröhlich-Nowoisky, S. Grawe, J. Lubitz, F. Stratmann, and R. M. McKay (2018). "A terrestrial origin for abundant riverine nanoscale ice-nucleating particles". In: *Environmental Science & Technology* 52.21, pp. 12358–12367.

Kulkarni, G., M. Nandasiri, A. Zelenyuk, J. Beranek, N. Madaan, A. Devaraj, V. Shutthanandan, S. Thevuthasan, and T. Varga (2015). "Effects of crystallographic properties on the ice nucleation properties of volcanic ash". In: *Geophysical Research Letters* 42, pp. 3048–3055.

Kulkarni, G., S. China, S. Liu, M. Nandasiri, N. Sharma, J. Wilson, A. C. Aiken, D. Chand, A. Laskin, C. Mazzoleni, M. Pekour, J. Shilling, V. Shutthanandan, A. Zelenyuk, and R. A. Zaveri (2016). "Ice nucleation activity of diesel soot particles at cirrus relevant temperature conditions: Effects of hydration, secondary organics coating, soot morphology, and coagulation". In: *Geophysical Research Letters* 43.7, pp. 3580–3588.

Lacher, L., P. J. DeMott, E. J. T. Levin, K. J. Suski, Y. Boose, A. Zipori, E. Herrmann, N. Bukowiecki, M. Steinbacher, E. Gute, J. P. D. Abbatt, U. Lohmann, and Z. A. Kanji (2018). "Background Free-Tropospheric Ice Nucleating Particle Concentrations at Mixed-Phase Cloud Conditions". In: *Journal of Geophysical Research: Atmospheres* 123.18, pp. 10506–10525.

Ladino Moreno, L. A., O. Stetzer, and U. Lohmann (2013). "Contact freezing: a review of experimental studies". In: *Atmospheric Chemistry and Physics* 13.19, pp. 9745–9769.

Langham, E. J. and B. J. Mason (1958). "The heterogeneous and homogeneous nucleation of supercooled water". In: *Proceedings of the Physical Society, Section A* 247, pp. 493–505.

Levin, E. J. T., G. R. McMeeking, P. J. DeMott, C. S. McCluskey, C. M. Carrico, S. Nakao, T. Jayarathne, E. A. Stone, C. E. Stockwell, R. J. Yokelson, and S. M. Kreidenweis (2016). "Ice-nucleating particle emissions from biomass combustion and the potential importance of soot aerosol". In: *Journal of Geophysical Research: Atmospheres* 121.10, pp. 5888–5903.

Levine, J. (1950). *Statistical explanation of spontaneous freezing of water droplets*. Technical Report NACA-TN-2172. National Aeronautics and Space Administration (NASA).

Liang, Z., X. He, and J. Ni (2010). "Change of crystallinity and mineral composition of fly ash with mechanical and chemical activation for the improvement of phosphate uptake". In: *Waste Management & Research* 28.10, pp. 901–907.

Linak, W. P., C. A. Miller, W. S. Seames, J. O. L. Wendt, T. Ishinomori, Y. Endo, and S. Miyamae (2002). "On trimodal particle size distributions in fly ash from pulverized-coal combustion". In: *Proceedings of the Combustion Institute* 29.1, pp. 441–447.

Ling, M. L., H. Wex, S. Grawe, J. Jakobsson, J. Löndahl, S. Hartmann, K. Finster, T. Boesen, and T. Šantl-Temkiv (2018). "Effects of ice nucleation protein repeat number and oligomerization level on ice nucleation activity". In: *Journal of Geophysical Research: Atmospheres* 123.3, pp. 1802–1810.

Lohmann, U. and K. Diehl (2006). "Sensitivity studies of the importance of dust ice nuclei for the indirect aerosol effect on stratiform mixed-phase clouds". In: *Journal of the Atmospheric Sciences* 63, pp. 968–982.

Losey, D., S. K. Sihvonen, D. Veghte, E. Chong, and M. A. Freedman (2018). "Acidic Processing of Fly Ash: Chemical Characterization, Morphology, and Immersion Freezing". In: *Environmental Science: Processes & Impacts* 20, pp. 1581–1592.

Lüönd, F., O. Stetzer, A. Welti, and U. Lohmann (2010). "Experimental study on the ice nucleation ability of size-selected kaolinite particles in the immersion mode". In: *Journal of Geophysical Research* 115.D14201. DOI: 10.1029/2009JD012959.

Mahrt, F., J. Wieder, R. Dietlicher, H. R. Smith, C. Stopford, and Z. A. Kanji (2018a). "Cloud Particle Phase Determination using a High-Speed Particle

Phase Discriminator". In: *15th Conference on Cloud Physics of the American Meteorological Society, 9-13 July, Vancouver, Canada*. Oral presentation.

Mahrt, F., C. Marcolli, R. O. David, P. Grönquist, E. J. Barthazy Meier, U. Lohmann, and Z. A. Kanji (2018b). "Ice nucleation abilities of soot particles determined with the Horizontal Ice Nucleation Chamber". In: *Atmospheric Chemistry and Physics* 18, pp. 13363–13392.

Mangan, T. P., J. D. Atkinson, J. W. Neuberg, D. O'Sullivan, T. W. Wilson, T. F. Whale, L. Neve, N. S. Umo, T. L. Malkin, and B. J. Murray (2017). "Heterogeneous Ice Nucleation by Soufriere Hills Volcanic Ash Immersed in Water Droplets". In: *PloS one* 12.1. DOI: 10.1371/journal.pone.0169720.

Marcolli, C. (2014). "Deposition nucleation viewed as homogeneous or immersion freezing in pores and cavities". In: *Atmospheric Chemistry and Physics* 14, pp. 2071–2104.

Marcolli, C., S. Gedamke, T. Peter, and B. Zobrist (2007). "Efficiency of immersion mode ice nucleation on surrogates of mineral dust". In: *Atmospheric Chemistry and Physics* 7, pp. 5081–5091.

Matsunaga, T., J. K. Kim, S. Hardcastle, and P. K. Rohatgi (2002). "Crystallinity and selected properties of fly ash particles". In: *Materials Science and Engineering: A* 325.1-2, pp. 333–343.

McCarthy, G. J., K. D. Swanson, L. P. Keller, and W. C. Blatter (1984). "Mineralogy of western fly ash". In: *Cement and Concrete Research* 14.4, pp. 471–478.

Moffett, B. F. (2016). "Fresh water ice nuclei". In: *Fundamental and Applied Limnology* 188.1, pp. 19–23.

Mueller, S. F., J. W. Mallard, Q. Mao, and S. L. Shaw (2013). "Fugitive particulate emission factors for dry fly ash disposal". In: *Journal of the Air and Waste Management Association* 63.7, pp. 806–818.

Murray, B. J., S. L. Broadley, T. W. Wilson, J. D. Atkinson, and R. H. Wills (2011). "Heterogeneous freezing of water droplets containing kaolinite particles". In: *Atmospheric Chemistry and Physics* 11, pp. 4191–4207.

Murray, B. J., D. O'Sullivan, J. D. Atkinson, and M. E. Webb (2012). "Ice nucleation by particles immersed in supercooled cloud droplets". In: *Chemical Society Reviews* 41, pp. 6519–6554.

Nathan, Y., M. Dvorachek, I. Pelly, and U. Mimran (1999). "Characterization of coal fly ash from Israel". In: *Fuel* 78.2, pp. 205–213.

Navea, J. G., E. Richmond, T. Stortini, and J. Greenspan (2017). "Water adsorption isotherms on fly ash from several sources". In: *Langmuir* 33.39, pp. 10161–10171.

Niedermeier, D., S. Hartmann, R. Shaw, D. Covert, T. F. Mentel, J. Schneider, L. Poulain, P. Reitz, C. Spindler, T. Clauss, A. Kiselev, E. Hallbauer, H. Wex, K. Mildenberger, and F. Stratmann (2010). "Heterogeneous freezing of droplets with immersed mineral dust particles - measurements and parameterization". In: *Atmospheric Chemistry and Physics* 10, pp. 3601–3614.

Niedermeier, D., R. A. Shaw, S. Hartmann, H. Wex, T. Clauss, J. Voigtländer, and F. Stratmann (2011). "Heterogeneous ice nucleation: exploring the transition from stochastic to singular freezing behavior". In: *Atmospheric Chemistry and Physics* 11, pp. 8767–8775.

Niedermeier, D., S. Augustin-Bauditz, S. Hartmann, H. Wex, K. Ignatius, and F. Stratmann (2015). "Can we define an asymptotic value for the ice active surface site density for heterogeneous ice nucleation?" In: *Journal of Geophysical Research: Atmospheres* 102, pp. 5036–5046.

Nyambura, M. G., G. W. Mugera, P. L. Felicia, and N. P. Gathura (2011). "Carbonation of brine impacted fractionated coal fly ash: Implications for CO_2 sequestration". In: *Journal of Environmental Management* 92.3, pp. 655–664.

O'Sullivan, D., B. J. Murray, J. F. Ross, T. F. Whale, H. C. Price, J. D. Atkinson, N. S. Umo, and M. E. Webb (2015). "The relevance of nanoscale biological fragments for ice nucleation in clouds". In: *Scientific Reports* 5.8082. DOI: 10.1038/srep08082.

Parungo, F. P., E. Ackerman, H. Proulx, and R. F. Pueschel (1978a). "Nucleation properties of fly ash in a coal-fired power-plant plume". In: *Atmospheric Environment* 12, pp. 929–935.

Parungo, F. P., P. A. Allee, and H. K. Weickmann (1978b). "Snowfall induced by a power plant plume". In: *Geophysical Research Letters* 5.6, pp. 515–517.

Petters, M. D. and T. P. Wright (2015). "Revisiting ice nucleation from precipitation samples". In: *Geophysical Research Letters* 42, pp. 8758–8766.

Plummer, L. N. and E. Busenberg (1982). "The solubilities of calcite, aragonite and vaterite in CO_2–H_2O solutions between 0 °C and 90 °C, and an evaluation of the aqueous model for the system $CaCO_3$–CO_2–H_2O". In: *Geochimica et Cosmochimica Acta* 46, pp. 1011–1040.

Polen, M., E. Lawlis, and R. C. Sullivan (2016). "The unstable ice nucleation properties of Snomax® bacterial particles". In: *Journal of Geophysical Research: Atmospheres* 121.19, pp. 11666–11678.

Pósfai, M., A. Gelencsér, R. Simonics, K. Arató, J. Li, P. V. Hobbs, and P. R. Buseck (2004). "Atmospheric tar balls: Particles from biomass and

biofuel burning". In: *Journal of Geophysical Research* 109.D06213. DOI: 10.1029/2003JD004169.

Pratt, K. A., P. J. DeMott, J. R. French, Z. Wang, D. L. Westphal, A. J. Heymsfield, C. T. Twohy, A. J. Prenni, and K. A. Prather (2009). "In situ detection of biological particles in cloud ice-crystals". In: *Nature Geoscience* 2, pp. 398–401.

Pruppacher, H. R. (1995). "A new look at homogeneous ice nucleation in supercooled water drops". In: *Journal of the Atmospheric Sciences* 52.11, pp. 1924–1933.

Pruppacher, H. R. and J. D. Klett (1997). *Microphysics of Clouds and Precipitation*. Kluwer Academic Publishers, Dodrecht, The Netherlands.

Pummer, B. G., H. Bauer, J. Bernardi, S. Bleicher, and H. Grothe (2012). "Suspendable macromolecules are responsible for ice nucleation activity of birch and conifer pollen". In: *Atmospheric Chemistry and Physics* 12, pp. 2541–2550.

Pummer, B. G., C. Budke, S. Augustin-Bauditz, D. Niedermeier, L. Felgitsch, C. J. Kampf, R. G. Huber, K. R. Liedl, T. Loerting, T. Moschen, M. Schauperl, M. Tollinger, C. E. Morris, H. Wex, H. Grothe, U. Pöschl, T. Koop, and J. Fröhlich-Nowoisky (2015). "Ice nucleation by water-soluble macromolecules". In: *Atmospheric Chemistry and Physics* 15, pp. 4077–4091.

Querol, X., A. Alastuey, A. Lopez-Soler, E. Mantilla, and F. Plana (1996). "Mineral composition of atmospheric particulates around a large coal-fired power station". In: *Atmospheric Environment* 30.21, pp. 3557–3572.

Ramsden, A. R. and M. Shibaoka (1982). "Characterization and analysis of individual fly-ash particles from coal-fired power stations by a combination of optical microscopy, electron microscopy and quantitative electron microprobe analysis". In: *Atmospheric Environment* 16.9, pp. 2191–2206.

Reff, A., P. V. Bhave, H. Simon, T. G. Pace, G. A. Pouliot, J. D. Mobley, and M. Houyoux (2009). "Emissions inventory of PM2.5 trace elements across the United States". In: *Environmental Science & Technology* 43.15, pp. 5790–5796.

Reicher, N., L. Segev, and Y. Rudich (2018). "The WeIzmann Supercooled Droplets Observation on a Microarray (WISDOM) and application for ambient dust". In: *Atmospheric Measurement Techniques* 11.1, pp. 233–248.

Rogers, R. R. and M. K. Yau (1989). *A Short Course in Cloud Physics*. Butterworth-Heinemann, Oxford, UK.

Rosenfeld, D. and W. L. Woodley (2000). "Deep convective clouds with sustained supercooled liquid water down to -37.5 °C". In: *Nature* 405, pp. 440–442.

Roth, A., J. Schneider, T. Klimach, S. Mertes, D. van Pinxteren, H. Herrmann, and S. Borrmann (2016). "Aerosol properties, source identification, and cloud processing in orographic clouds measured by single particle mass spectrometry on a central European mountain site during HCCT-2010". In: *Atmospheric Chemistry and Physics* 16.2, pp. 505–524.

Saunders, C. P. R. (1993). "A Review of Thunderstorm Electrification Processes". In: *Journal of Applied Meteorology* 32.4, pp. 642–655.

Schill, G. P., S. H. Jathar, J. K. Kodros, E. J. T. Levin, A. M. Galang, B. Friedman, M. F. Link, D. K. Farmer, J. R. Pierce, S. M. Kreidenweis, and P. J. DeMott (2016). "Ice-nucleating particle emissions from photochemically aged diesel and biodiesel exhaust". In: *Geophysical Research Letters* 43.10, pp. 5524–5531.

Schmidt, S., J. Schneider, T. Klimach, S. Mertes, L. P. Schenk, P. Kupiszewski, J. Curtius, and S. Borrmann (2017). "Online single particle analysis of ice particle residuals from mountain-top mixed-phase clouds using laboratory derived particle type assignment". In: *Atmospheric Chemistry and Physics* 17.1, pp. 575–594.

Schmitz, C. H. J., A. C. Rowat, S. Köster, and D. A. Weitz (2009). "Dropspots: a picoliter array in a microfluidic device". In: *Lab on a Chip* 9.1, pp. 44–49.

Schnell, R. C., C. C. Van Valin, and R. F. Pueschel (1976). "Atmospheric ice nuclei: No detectable effect from a coal-fired powerplant plume". In: *Geophysical Research Letters* 3.11, pp. 657–660.

Seames, W. S. (2003). "An initial study of the fine fragmentation fly ash particle mode generated during pulverized coal combustion". In: *Fuel Processing Technology* 81.2, pp. 109–125.

Sedlacek III, A. J., P. R. Buseck, K. Adachi, T. B. Onasch, S. R. Springston, and L. Kleinman (2018). "Formation and evolution of tar balls from northwestern US wildfires". In: *Atmospheric Chemistry and Physics* 18.15, pp. 11289–11301.

Seinfeld, J. H., Y. Kousaka, and K. Okuyama (2006). "Aerosols". In: *Encyclopedia of Environmental Science and Engineering*. 5th ed. Vol. 1. CRC Press, Boca Raton, FL, USA, pp. 15–28.

Shen, J. H., K. Klier, and C. Zettlemoyer (1977). "Ice Nucleation by Micas". In: *Journal of the Atmospheric Sciences* 34, pp. 957–960.

Sherwood, S. C., V. T. J. Phillips, and J. S. Wettlaufer (2006). "Small ice crystals and the climatology of lightning". In: *Geophysical Research Letters* 33.5. DOI: 10.1029/2005GL025242.

Shoumkova, A., T. Tsacheva, V. Stoyanova, I. Grancharov, S. Shumkov, and M. Marinov (2005). "Physico-chemical and morphological properties of

coal fly ash from Varna power plant, Bulgaria". In: *Proceedings of the Third International Conference on Ecological Chemistry*, pp. 560–570.

Sievert, T., A. Wolter, and N. B. Singh (2005). "Hydration of anhydrite of gypsum ($CaSO_4$. II) in a ball mill". In: *Cement and Concrete Research* 35.4, pp. 623–630.

Sihvonen, S. K., G. P. Schill, N. A. Lyktey, D. P. Veghte, M. A. Tolbert, and M. A. Freedman (2014). "Chemical and physical transformations of aluminosilicate clay minerals due to acid treatment and consequences for heterogeneous ice nucleation". In: *Journal of Physical Chemistry A* 118.38, pp. 8787–8796.

Smil, V. (2008). *Energy in Nature and Society: General Energetics of Complex Systems*. MIT Press, Cambridge, MA, USA.

Srivastava, R. K. and W. Jozewicz (2001). "Flue gas desulfurization: the state of the art". In: *Journal of the Air & Waste Management Association* 51.12, pp. 1676–1688.

Steinke, I., R. Funk, J. Busse, A. Iturri, S. Kirchen, M. Leue, O. Möhler, T. Schwartz, M. Schnaiter, B. Sierau, E. Toprak, R. Ullrich, A. Ulrich, C. Hoose, and T. Leisner (2016). "Ice nucleation activity of agricultural soil dust aerosols from Mongolia, Argentina, and Germany". In: *Journal of Geophysical Research: Atmospheres* 121.22, pp. 13559–13576.

Stetzer, O., B. Baschek, F. Lüönd, and U. Lohmann (2008). "The Zurich Ice Nucleation Chamber (ZINC) - A new instrument to investigate atmospheric ice nucleation". In: *Aerosol Science and Technology* 42.1, pp. 64–74.

Storelvmo, T., C. Hoose, and P. Eriksson (2011). "Global modeling of mixed-phase clouds: The albedo and lifetime effects of aerosols". In: *Journal of Geophysical Research* 116.D05207. DOI: 10.1029/2010JD014724.

Stratmann, F. and A. Wiedensohler (1996). "A new data inversion algorithm for DMPS-measurements". In: *Journal of Aerosol Science* 27.Suppl. 1, pp. 339–340.

Sullivan, R. C., M. J. K. Moore, M. D. Petters, S. M. Kreidenweis, O. Qafoku, A. Laskin, G. C. Roberts, and K. A. Prather (2010). "Impact of particle generation method on the apparent hygroscopicity of insoluble mineral particles". In: *Aerosol Science and Technology* 44, pp. 830–846.

Takahashi, T. (1978). "Riming electrification as a charge generation mechanism in thunderstroms". In: *Journal of the Atmospheric Sciences* 35, pp. 1536–1548.

Tan, P. V., M. S. Fila, G. J. Evans, and R. E. Jervis (2002). "Aerosol laser ablation mass spectrometry of suspended powders from PM sources and

its implications to receptor modeling". In: *Journal of the Air & Waste Management Association* 52.1, pp. 27–40.

Umo, N. S., B. J. Murray, M. T. Baeza-Romero, J. M. Jones, A. R. Lea-Langton, T. L. Malkin, D. O'Sullivan, L. Neve, J. M. C. Plane, and A. Williams (2015). "Ice nucleation by combustion ash particles at conditions relevant to mixed-phase clouds". In: *Atmospheric Chemistry and Physics* 15, pp. 5195–5210.

Umo, N. S., R. Wagner, R. Ullrich, A. Kiselev, H. Saathoff, P. G. Weidler, D. J. Cziczo, T. Leisner, and O. Möhler (2019). "Enhanced ice nucleation activity of coal fly ash aerosol particles initiated by ice-filled pores". In: *Atmospheric Chemistry and Physics Discussions* 19, pp. 1–26. DOI: 10.5194/acp-2019-7.

Vali, G. (1971). "Quantitative evaluation of experimental results on the heterogeneous freezing nucleation of supercooled liquids". In: *Journal of the Atmospheric Sciences* 28, pp. 402–409.

– (2008). "Repeatability and randomness in heterogeneous freezing nucleation". In: *Atmospheric Chemistry and Physics* 8, pp. 5017–5031.

Vali, G. and E. J. Stansbury (1966). "Time-dependent characteristics of the heterogeneous nucleation of ice". In: *Canadian Journal of Physics* 44.3, pp. 477–502.

Vali, G., P. J. DeMott, O. Möhler, and T. F. Whale (2015). "Technical Note: A proposal for ice nucleation terminology". In: *Atmospheric Chemistry and Physics* 15, pp. 10263–10270.

Vassilev, S. V. and C. G. Vassileva (2005). "Methods for characterization of composition of fly ashes from coal-fired power stations: a critical overview". In: *Energy & Fuels* 19.3, pp. 1084–1098.

Vergara-Temprado, J., A. K. Miltenberger, K. Furtado, D. P. Grosvenor, B. J. Shipway, A. A. Hill, J. M. Wilkinson, P. R. Field, B. J. Murray, and K. S. Carslaw (2018). "Strong control of Southern Ocean cloud reflectivity by ice-nucleating particles". In: *Proceedings of the National Academy of Sciences* 115.11, pp. 2687–2692.

Vonnegut, B. (1947). "The nucleation of ice formation by silver iodide". In: *Journal of Applied Physics* 18.7, pp. 593–595.

Wagner, R., A. Kiselev, O. Möhler, H. Saathoff, and I. Steinke (2016). "Pre-activation of ice-nucleating particles by the pore condensation and freezing mechanism". In: *Atmospheric Chemistry and Physics* 16.

Wagner, R., K. Höhler, W. Huang, A. Kiselev, O. Möhler, C. Mohr, A. Pajunoja, H. Saathoff, T. Schiebel, X. Shen, and A. Virtanen (2017). "Heterogeneous ice nucleation of α-pinene SOA particles before and after ice cloud processing". In: *Journal of Geophysical Research: Atmospheres* 122, pp. 4924–4943.

Ward, C. R. and D. French (2006). “Determination of glass content and estimation of glass composition in fly ash using quantitative X-ray diffractometry”. In: *Fuel* 85.16, pp. 2268–2277.

Weinbruch, S., M. Ebert, H. Gorzawski, T. Dirsch, T. Berg, and E. Steinnes (2010). “Characterisation of individual aerosol particles on moss surfaces: implications for source apportionment”. In: *Journal of Environmental Monitoring* 12.5, pp. 1064–1071.

Weinbruch, S., D. Wiesemann, M. Ebert, K. Schütze, R. Kallenborn, and J. Ström (2012). “Chemical composition and sources of aerosol particles at Zeppelin Mountain (Ny Ålesund, Svalbard): An electron microscopy study”. In: *Atmospheric Environment* 49, pp. 142–150.

Weiss, F., F. Kubel, Ó. Gálvez, M. Hoelzel, S. F. Parker, P. Baloh, R. Iannarelli, M. J. Rossi, and H. Grothe (2016). “Metastable nitric acid trihydrate in ice clouds”. In: *Angewandte Chemie International Edition* 55.10, pp. 3276–3280.

Welti, A., K. Müller, Z. L. Fleming, and F. Stratmann (2018). “Concentration and variability of ice nuclei in the subtropical maritime boundary layer”. In: *Atmospheric Chemistry and Physics* 18, pp. 5307–5320.

Westbrook, C. D. and A. J. Illingworth (2011). “Evidence that ice forms primarily in supercooled liquid clouds at temperatures $> -27\,^{\circ}\mathrm{C}$”. In: *Geophysical Research Letters* 38.14. DOI: 10.1029/2011GL048021.

Wex, H., P. J. DeMott, Y. Tobo, S. Hartmann, M. Rösch, T. Clauß, L. Tomsche, D. Niedermeier, and F. Stratmann (2014). “Kaolinite particles as ice nuclei: Learning from the use of different kaolinite samples and different coatings”. In: *Atmospheric Chemistry and Physics* 14, pp. 5529–5546.

Wex, H., S. Augustin-Bauditz, Y. Boose, C. Budke, J. Curtius, K. Diehl, A. Dreyer, F. Frank, S. Hartmann, N. Hiranuma, E. Jantsch, Z. A. Kanji, A. Kiselev, T. Koop, O. Möhler, D. Niedermeier, B. Nillius, M. Rösch, D. Rose, C. Schmidt, I. Steinke, and F. Stratmann (2015). “Intercomparing different devices for the investigation of ice nucleating particles using Snomax® as a test substance”. In: *Atmospheric Chemistry and Physics* 15, pp. 1463–1485.

Whale, T. F. (2018). “Ice Nucleation in Mixed-Phase Clouds”. In: *Mixed-Phase Clouds: Observations and Modelling*. Elsevier, Cambridge, MA, USA, pp. 13–41.

Whale, T. F., B. J. Murray, D. O’Sullivan, T. W. Wilson, N. S. Umo, K. J. Baustian, J. D. Atkinson, D. A. Workneh, and G. J. Morris (2015). “A technique for quantifying heterogeneous ice nucleation in microlitre supercooled water droplets”. In: *Atmospheric Measurement Techniques* 8, pp. 2437–2447.

Wilson, T. W., L. A. Ladino, P. A. Alpert, M. N. Breckels, I. M. Brooks, J. Browse, S. M. Burrows, K. S. Carslaw, J. A. Huffman, C. Judd, W. P. Kilthau, R. H. Mason, G. McFiggans, L. A. Miller, J. J. Nájera, E. Polishchuk, C. L. Schiller S. Rae, M. Si, J. Vergara Temprado, T. F. Whale, J. P. S. Wong, O. Wurl, J. D. Yakobi-Hancock, J. P. D. Abbatt, J. Y. Aller, A. K. Bertram, D. A. Knopf, and B. J. Murray (2015). "A marine biogenic source of atmospheric ice-nucleating particles". In: *Nature* 525.7568, pp. 234–238.

Wright, T. P., M. D. Petters, J. D. Hader, T. Morton, and A. L. Holder (2013). "Minimal cooling rate dependence of ice nuclei activity in the immersion mode". In: *Journal of Geophysical Research: Atmospheres* 118, pp. 10535–10543. DOI: 10.1002/jgrd.50810.

Yi, H., X. Guo, J. Hao, L. Duan, and X. Li (2006). "Characteristics of inhalable particulate matter concentration and size distribution from power plants in China". In: *Journal of the Air and Waste Management Association* 56, pp. 1243–1251.

Young, T. (1805). "An essay on the cohesion of fluids". In: *Philosophical Transactions of the Royal Society of London*, pp. 65–87.

Zhang, L., Y. Ninomiya, and T. Yamashita (2006). "Formation of submicron particulate matter (PM_1) during coal combustion and influence of reaction temperature". In: *Fuel* 85.10-11, pp. 1446–1457.

Zhang, X., G. Wu, T. Yao, C. Zhang, and Y. Yue (2011). "Characterization of individual fly ash particles in surface snow at Urumqi Glacier No. 1, Eastern Tianshan". In: *Chinese Science Bulletin* 56.32, pp. 3464–3473.

Zheng, J. and M. Yamada (2006). "Inductively coupled plasma-sector field mass spectrometry with a high-efficiency sample introduction system for the determination of Pu isotopes in settling particles at femtogram levels". In: *Talanta* 69, pp. 1246–1253.

Zobrist, B. (2006). "Heterogeneous ice nucleation in upper tropospheric aerosols". PhD thesis. Eidgenössische Technische Hochschule Zürich, Zurich, Switzerland.

Zobrist, B., T. Koop, B. P. Luo, C. Marcolli, and T. Peter (2007). "Heterogeneous ice nucleation rate coefficient of water droplets coated by a nonadecanol monolayer". In: *The Journal of Physical Chemistry C* 111.5, pp. 2149–2155.

Zolles, T., J. Burkart, T. Häusler, B. Pummer, R. Hitzenberger, and H. Grothe (2015). "Identification of ice nucleation active sites on feldspar dust particles". In: *Journal of Physical Chemistry A* 119, pp. 2692–2700.

Zondlo, M. A., P. K. Hudson, A. J. Prenni, and M. A. Tolbert (2000). “Chemistry and microphysics of polar stratospheric clouds and cirrus clouds”. In: *Physical Chemistry* 51, pp. 473–499.

Zusammenfassung der Dissertation

Coal fly ash: How sample properties and methodology influence immersion freezing results

der Fakultät für Physik und Geowissenschaften eingereicht von

M. Sc. Sarah Grawe
angefertigt am
Leibniz-Institut für Troposphärenforschung
Februar 2019

It is a well-established fact that the formation of ice particles in clouds affects radiative properties, precipitation, electrification, and chemistry (e.g., Takahashi, 1978; Abbatt, 2003; Storelvmo et al., 2011; Vergara-Temprado et al., 2018). Aerosol particles with certain properties, so-called ice nucleating particles (INPs), play an important role in primary ice formation by lowering the energy barrier that needs to be overcome for nucleation to occur. A variety of different particle types has been found in ice crystal residues, among them mineral dust, biological particles, and combustion particles, such as soot and fly ash (DeMott et al., 2003; Pratt et al., 2009; Eriksen Hammer et al., 2018). While the ice nucleation ability of the majority of these particle types has been extensively investigated in laboratory settings (Murray et al., 2012, and references therein), there are very few ice nucleation studies dealing with coal fly ash (CFA) particles (Havlíček et al., 1993; Umo et al., 2015; Garimella, 2016).

CFA is emitted from power plants and disposal sites all over the world (∼30 Mt/a; Smil, 2008) and existing studies, as well as the presence of the particles in ice crystal residues, indicate that CFA can trigger ice formation in the atmosphere. However, previous results show a large spread with respect to the ice nucleation efficiency of samples from different origins and it was suspected, but not yet proven, that this variability is caused by both differences in physicochemical properties and the application of different methods (Grawe et al., 2016). The overall aim of the present thesis is to

clarify how physicochemical properties and methodology (more precisely, the amount of time that the particles spend in contact with water) influence the ice nucleation behavior of CFA samples.

Investigations were performed on CFA particles immersed in supercooled cloud droplets using samples from German coal-fired power plants and several established ice nucleation measurement techniques. In parallel, the samples were analyzed with respect to their chemical composition, crystallography, and morphology. By connecting results from the ice nucleation experiments and the physicochemical analysis, it was found that several components in the complex mixture influence the ice nucleation behavior. Specifically, it was possible to identify one substance which very likely contributes to the observed, methodology-dependent results. The key findings can be summarized as follows:

- All CFA samples show a tendency of reduced ice nucleation efficiency with an increase in suspension time. In other words, the longer the particles stay in contact with water prior to the initiation of freezing, the lower the number of particles that act as INPs. This deactivation is observed on very short time scales (seconds to minutes). When investigated with the fastest technique (1.6 s between droplet activation and freezing) below $-27\,^{\circ}\mathrm{C}$, the ice nucleation efficiency of the samples is comparable to that of mineral dust, i.e., more efficient than clay minerals but less efficient than K-feldspar (Augustin-Bauditz et al., 2014).

- Both the efficient triggering of ice nucleation of shortly suspended particles as well as the deactivation with elongated suspension time correlate with the concentration of anhydrite (anhydrous $CaSO_4$) in the samples. Anhydrite is hydrated to gypsum ($CaSO_4{\cdot}2H_2O$) in contact with water. A layer of hydrated ions on the particle surface potentially prevents direct interaction with the water molecules, thus impairing ice nucleation. Assuming that the experiments with elongated suspension time are representative for atmospheric processing, anhydrite-rich CFA samples, which will be hydrated in suspension, will contribute less to atmospheric ice nucleation than anhydrite-deficient CFA samples which will not be hydrated.

- A literature review of all available ice nucleation measurements with immersed CFA particles reveals a spread of 7 orders of magnitude. This spread is related to the varying chemical composition of samples from different sources, especially the concentration of hydratable substances such as anhydrite but probably also other, non-hydratable substances. The application of ice nucleation instrumentation with varying suspension times accounts for ∼50 % of the observed variability.

In the framework of this thesis, short-term changes of the ice nucleation efficiency of CFA due to hydration effects in suspension have been detected for the first time. Furthermore, it was shown that the ice nucleation efficiency of CFA samples from different sources is highly variable, even when accounting for differences in methodology. Consequently, the present thesis contributes to improving fundamental process understanding and, eventually, to a more accurate estimation of the contribution of CFA particles to the atmospheric INP population.

References

Abbatt, J. P. D. (2003). "Interactions of atmospheric trace gases with ice surfaces: Adsorption and reaction". In: *Chemical Reviews* 103.12, pp. 4783–4800.

Augustin-Bauditz, S., H. Wex, S. Kanter, M. Ebert, D. Niedermeier, F. Stolz, A. Prager, and F. Stratmann (2014). "The immersion mode ice nucleation behavior of mineral dusts: A comparison of different pure and surface modified dusts". In: *Geophysical Research Letters* 41.20, pp. 7375–7382.

DeMott, P. J., D. J. Cziczo, A. J. Prenni, D. M. Murphy, S. M. Kreidenweis, D. S. Thomson, R. Borys, and D. C. Rogers (2003). "Measurements of the concentration and composition of nuclei for cirrus formation". In: *Proceedings of the National Academy of Sciences* 100.25, pp. 14655–14660.

Eriksen Hammer, S., S. Mertes, J. Schneider, M. Ebert, K. Kandler, and S. Weinbruch (2018). "Composition of ice particle residuals in mixed-phase clouds at Jungfraujoch (Switzerland): enrichment and depletion of particle groups relative to total aerosol". In: *Atmospheric Chemistry and Physics* 18, pp. 13987–14003.

Garimella, S. (2016). "A vertically-integrated approach to climate science: From measurements and machine learning to models and policy". PhD thesis. Massachusetts Institute of Technology, Cambridge, MA, USA.

Grawe, S., S. Augustin-Bauditz, S. Hartmann, L. Hellner, J. B. C. Pettersson, A. Prager, F. Stratmann, and H. Wex (2016). "The immersion freezing behavior of ash particles from wood and brown coal burning". In: *Atmospheric Chemistry and Physics* 16, pp. 13911–13928.

Havlíček, D., R. Přibil, and O. Školoud (1993). "The chemical and mineralogical composition of the water-soluble fraction of power-plant ash and its effect on the process of crystallization of water". In: *Atmospheric Environment* 27A.5, pp. 655–660.

Murray, B. J., D. O'Sullivan, J. D. Atkinson, and M. E. Webb (2012). "Ice nucleation by particles immersed in supercooled cloud droplets". In: *Chemical Society Reviews* 41, pp. 6519–6554.

Pratt, K. A., P. J. DeMott, J. R. French, Z. Wang, D. L. Westphal, A. J. Heymsfield, C. T. Twohy, A. J. Prenni, and K. A. Prather (2009). "*In situ* detection of biological particles in cloud ice-crystals". In: *Nature Geoscience* 2, pp. 398–401.

Smil, V. (2008). *Energy in Nature and Society: General Energetics of Complex Systems*. MIT Press, Cambridge, MA, USA.

Storelvmo, T., C. Hoose, and P. Eriksson (2011). "Global modeling of mixed-phase clouds: The albedo and lifetime effects of aerosols". In: *Journal of Geophysical Research* 116.D05207. DOI: 10.1029/2010JD014724.

Takahashi, T. (1978). "Riming electrification as a charge generation mechanism in thunderstroms". In: *Journal of the Atmospheric Sciences* 35, pp. 1536–1548.

Umo, N. S., B. J. Murray, M. T. Baeza-Romero, J. M. Jones, A. R. Lea-Langton, T. L. Malkin, D. O'Sullivan, L. Neve, J. M. C. Plane, and A. Williams (2015). "Ice nucleation by combustion ash particles at conditions relevant to mixed-phase clouds". In: *Atmospheric Chemistry and Physics* 15, pp. 5195–5210.

Vergara-Temprado, J., A. K. Miltenberger, K. Furtado, D. P. Grosvenor, B. J. Shipway, A. A. Hill, J. M. Wilkinson, P. R. Field, B. J. Murray, and K. S. Carslaw (2018). "Strong control of Southern Ocean cloud reflectivity by ice-nucleating particles". In: *Proceedings of the National Academy of Sciences* 115.11, pp. 2687–2692.

List of Publications

Part of this thesis:

Grawe, S., S. Augustin-Bauditz, H.-C. Clemen, M. Ebert, S. Eriksen Hammer, J. Lubitz, N. Reicher, Y. Rudich, J. Schneider, R. Staacke, F. Stratmann, A. Welti, and H. Wex (2018). "Coal fly ash: linking immersion freezing behavior and physicochemical particle properties". In: *Atmospheric Chemistry and Physics* 18, pp. 13903–13923.

In this study, I was in charge of particle generation and LACIS measurements. Ideally, two people are available for LACIS experiments and hence Stefanie Augustin-Bauditz and Jasmin Lubitz supported me in equal parts. Jasmin Lubitz performed part of the LINA measurements, the remaining measurements were performed by myself. I evaluated the data obtained in the LACIS and LINA experiments. Hans-Christian Clemen performed ALABAMA measurements and data evaluation with the support of Johannes Schneider. Stine Eriksen Hammer performed particle sampling with the Multi-MINI and ESEM/EDX analysis with the support of Martin Ebert. Naama Reicher performed WISDOM and BET measurements. André Welti perfomed SPIN measurements and data evaluation. Robert Staacke performed XRD measurements and supported me with the data evaluation. Hans-Christian Clemen, Johannes Schneider, Stine Eriksen Hammer, Robert Staacke, and myself discussed the particle characterization results. Heike Wex, Frank Stratmann, and myself were involved in the discussion of the immersion freezing results. I deduced the presented interpretations based on both immersion freezing and particle characterization results. Heike Wex procured the CFA samples and coordinated the INUIT campaign. The manuscript was written by myself with short contributions from Hans-Christian Clemen, Stine Eriksen Hammer, and Naama Reicher. Proofreading of the first version was performed by Heike Wex, and of the final version by all co-authors.

Not part of this thesis:

Grawe, S., S. Augustin-Bauditz, S. Hartmann, L. Hellner, J. B. C. Pettersson, A. Prager, F. Stratmann, and H. Wex (2016). "The immersion freezing behavior of ash particles from wood and brown coal burning". In: *Atmospheric Chemistry and Physics* 16, pp. 13911–13928.

In this study, I performed particle generation and LACIS measurements with support from Lisa Hellner and Stefanie Augustin-Bauditz and evaluated the data. I was strongly involved in the discussion of the particle characterization and immersion freezing results. I wrote the manuscript.

Burkert-Kohn, M., H. Wex, A. Welti, S. Hartmann, **S. Grawe**, L. Hellner, P. Herenz, J. D. Atkinson, F. Stratmann, and Z. A. Kanji (2017). "Leipzig Ice Nucleation chamber Comparison (LINC): Inter-comparison of four online ice nucleation counters". In: *Atmospheric Chemistry and Physics* 17, pp. 11683–11705.

Here, I contributed by performing the LACIS experiments and data evaluation as well as simulations with the Soccer Ball Model. I was involved in the discussion of the results and proofreading of the manuscript.

Ling, M. L., H. Wex, **S. Grawe**, J. Jakobsson, J. Löndahl, S. Hartmann, K. Finster, T. Boesen, and T. Šantl-Temkiv (2018). "Effects of ice nucleation protein repeat number and oligomerization level on ice nucleation activity". In: *Journal of Geophysical Research: Atmospheres* 123.3, pp. 1802–1810.

In this study, I performed LINA and LACIS measurements and the respective data evaluation. I contributed to the discussion of the immersion freezing results and proofread the manuscript.

Chen, J., Z. Wu, S. Augustin-Bauditz, **S. Grawe**, M. Hartmann, X. Pei, Z. Liu, D. Ji, and H. Wex (2018). "Ice-nucleating particle concentrations unaffected by urban air pollution in Beijing, China". In: *Atmospheric Chemistry and Physics* 18, pp. 3523–3539.

For this publication, I gave support during the LINA measurements and development of the calibration routine. I was involved in the discussion of the results and proofreading of the manuscript.

Knackstedt, K., B. F. Moffett, S. Hartmann, H. Wex, T. C. J. Hill, E. Glasgo, L. Reitz, S. Augustin-Bauditz, B. Beall, G. S. Bullerjahn, J. Fröhlich-Nowoisky, **S. Grawe**, J. Lubitz, F. Stratmann, and R. M. McKay (2018). "A terrestrial origin for abundant riverine nanoscale ice-nucleating particles". In: *Environmental Science & Technology* 52 (21), pp. 12358–12367.

For this study, I established contact between the research groups at Bowling Green State University and TROPOS. I performed part of the measurements with the Ice Nucleation Droplet Array (INDA).

Hiranuma, N., K. Adachi, D. Bell, F. Belosi, H. Beydoun, B. Bhaduri, H. Bingemer, C. Budke, H.-C. Clemen, F. Conen, K. Cory, J. Curtius, P. DeMott, O. Eppers, **S. Grawe**, S. Hartmann, N. Hoffmann, K. Höhler, E. Jantsch, A. Kiselev, T. Koop, G. Kulkarni, A. Mayer, M. Murakami, B. Murray, A. Nicosia, M. Petters, M. Piazza, M. Polen, N. Reicher, Y. Rudich, A. Saito, G. Santachiara, T. Schiebel, G. Schill, J. Schneider, L. Segev, E. Stopelli, R. Sullivan, K. Suski, M. Szakáll, T. Tajiri, H. Taylor, Y. Tobo, D. Weber, H. Wex, T. Whale, C. Whiteside, K. Yamashita, A. Zelenyuk, and O. Möhler. (2019). "A comprehensive characterization of ice nucleation by three different types of cellulose particles immersed in water: lessons learned and future research directions". In: *Atmospheric Chemistry and Physics Discussions* 19, pp. 1–82.

This study is still in review. Here, I performed LACIS measurements with dry- and wet-generated particles and contributed to the respective paragraph in the manuscript.

Acknowledgments

To Heike and Frank: Thank you for giving me the opportunity to further investigate this topic which still had a large question mark after my master's thesis. Thanks for contributing ideas and supporting mine. Thanks for making important contacts. Thanks for reading and commenting my manuscripts. Thanks for your time. And thanks for sending me to inspiring conferences and workshops.

To Profs. Wendisch, Macke, and Tegen: Thank you for your technical and strategic guidance as my doctoral committee. A special thanks goes to Prof. Macke for supervising and reviewing this thesis.

To Steffi, Susi, and Dennis: Thank you for introducing me to the world of heterogeneous ice nucleation. Thanks for helping me with practical and theoretical issues. And thanks for being great company on business trips.

To my co-authors: Thank you for mastering this mammoth publication together. Special thanks to Stine, Hans, Naama, and Robert S. who put so much effort into helping me, despite their own PhD projects. Without your input I would not have been able to solve the mystery of the coal fly ash particles.

To the members of the TROPOS cloud group: Thanks for welcoming me as an inexperienced Master student and for helping me become a slightly more experienced PhD. Thanks for the reviving coffee breaks. I hope I will have similarly great ones with my new colleagues.

To my office colleagues: Thanks to Steffi, Henner, and Karoliina for some great first months and interesting, sometimes even work-related discussions. Thanks to Xianda, Silvio, and Christian for providing a quiet and relaxed working environment which helped me tremendously during my final year.

To the TROPOTONES: Thanks for taking my mind off work every once in a while. Playing with you often brought great end to an ordinary workday.

To my fellow PhD students: Thanks for many memorable PhD events and retreats which were always a good mixture of fun and education. Special thanks to Robert W. for introducing me to non-alcoholic beer.

To my friends: Thanks for distracting me with amazing holidays, delicious food, trash TV evenings, great music, and your nice company.

To my family: Thanks for your interest in my work, your relentless support, your encouragement, and your patience.

To Robert S. again: Thank you for making the difference.

Declaration of Independence

I hereby declare that I prepared this PhD thesis without inadmissible aid and only by the usage of the specified sources. I also declare that I marked the directly or indirectly adopted ideas from external references. Furthermore, I confirm that this PhD thesis is entirely the result or my own investigations except where otherwise indicated. In particular, I assure that I did not use the assistance of a doctoral consultant. I guarantee that no one has gained pecuniary advantages related to the content of this PhD thesis from me or from other persons on behalf of me.

I assure that this PhD thesis was not submitted in an identical or similar design to another examination office for the purpose of a graduation or another examination procedure. I also state that I have not been involved in another PhD procedure.

Leipzig, February 21, 2019